Title	Studies on Quinoidal and Anti-aromatic Compounds Having Tuned Electronic Structure for Application to Organic Semiconducting Materials
Author(s)	山本, 恵太郎
Citation	大阪大学, 2020, 博士論文
Version Type	VoR
URL	https://doi.org/10.18910/76515
rights	
Note	

Doctoral Dissertation

Studies on Quinoidal and Anti-aromatic Compounds Having Tuned Electronic Structure for Application to Organic Semiconducting Materials

Keitaro Yamamoto
January 2020

Graduate School of Engineering
Osaka University

Preface

The study presented in this thesis has been carried out under the guidance of Professor Yutaka Ie and Professor Yoshio Aso at The Institute of Scientific and Industrial Research (ISIR), Osaka University from April 2015 to March 2020.

This thesis concerns the synthesis, structure, properties, and semiconducting characteristics of new quinoidal and anti-aromatic compounds having tuned electronic structure by molecular modification. The objective of this work is to reveal the structure–property relationship of π-conjugated compounds having pro-aromatic nature for application to organic semiconducting materials.

Department of Applied Chemistry
Graduate School of Engineering
Osaka University

Suita, Osaka, Japan
January 2020

Keitaro Yamamoto

Table of Contents

Chapter 3 Effects of Fluorine Substitution in Quinoidal Oligothiophenes for Organic Semiconductors

Chapter 4 Development of Anti-aromatic Framework Containing Heptafulvene Segment

General Introduction

The importance of organic electronics such as organic light-emitting diode (OLED), organic photovoltaics (OPV), and organic field-effect transistor (OFET) has increased significantly by the potential to allow device fabrication over large areas and/or on flexible and lightweight substrates.[1] π-Conjugated compounds for use as the active materials in organic electronics have been the subject of intense study not only for elucidating of their structure−property relationship but also for evaluation of their semiconducting chracteristics.[2] The properties of organic semiconductors primarily depend on the energy levels of the highest occupied molecular orbital (HOMO) and lowest unoccupied molecular orbital (LUMO) of the molecules, and structural modification of π-conjugated frameworks enabled us to create hole-transporting (p-type) and electron-transporting (n-type) materials. So far, polycyclic aromatic hydrocarbons or polymers based on aromatic rings have been mainly developed for such organic semiconducting materials (Figure 1(a)). Compared with p-type organic semiconductor, the repertories of n-type materials are still limited due to the difficulty of lowering the LUMO energy level to match with the work function of metal electrodes, and thus further investigation for new n-type materials is necessary.

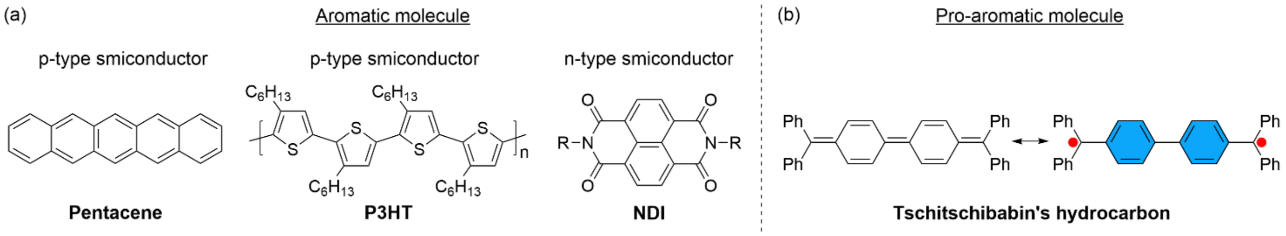

Figure 1. Structures of (a) aromatic molecules for semiconducting materials and (b) pro-aromatic molecule.

In 1907, Tschitschibabin synthesized a novel hydrocarbon bearing quinoidal structure, which is different from the conventional aromatic molecules (Figure 1 (b)).[3] One of the distinct features of quinoidal molecules is the existence of open-shell electronic configuration in the ground state because of their pro-aromatic nature, which originates the driving force of aromatic stabilization of each rings having [4n+2] π scaffolds.[4] Bis(dicyanomethylene)-substituted quinoidal oligothiophenes are representative quinoidal molecules. Pro-aromatic nature of quinoidal oligothiophenes can stabilize the reduced species, which enable these compounds to be promising candidates for application to n-type OFET materials (Figure 2(a)).[5] It was also demonstrated that the quinoidal oligothiophenes have a resonance between a closed-shell quinoidal state and an open-shell biradical state due to the driving force of aromatization of thiophene rings (Figure 2(b)).[6] The biradical character of pro-aromatic compounds have attracted attention in terms of nonlinear optics and spintronics.[7] However, such Kekulé diradicaloids with high biradical character sometimes suffer from the instability of the molecules. In this context, understanding and controlling of the biradical character of quinoidal molecules become important for application to organic electronics.

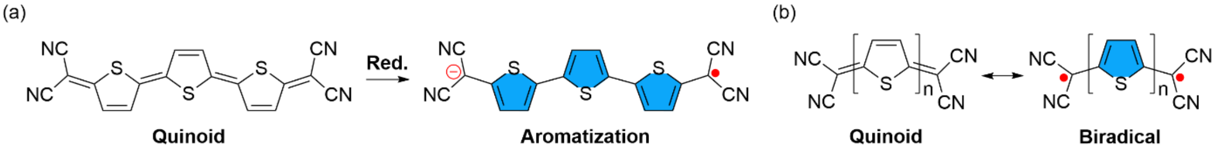

Figure 2. Depiction of (a) high electron-accepting nature and (b) resonance form of quinoidal oligothiophenes.

While, [4*n*] π conjugated systems with planar cyclic arrangement are thought to be anti-aromatic compounds, which show the unique properties such as unique redox behavior (Figure 3(a)).[8] Among them, indenofluorene derivatives are most well-investigated [4*n*] π system based on non-benzenoid frameworks.[9] Indenofluorene derivatives also have biradical character due to the pro-aromatic nature in the ground state, and the molecular design is based on the introduction of substituents that could sterically stabilize the reactive site having high spin density (Figure 3(b)). However, the synthetic report of anti-aromatic compounds is limited because of the intrinsic instability. Thus, development of novel [4*n*] π backbones becomes a critical issue to enable application of anti-aromatic compounds for use as organic electronics.

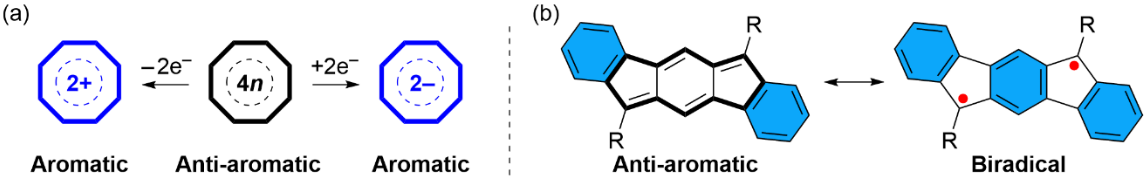

Figure 3. Depiction of (a) redox behavior of anti-aromatic compound and (b) resonance form of indeno[1,2-*b*]fluorene.

Considering this situation, I developed novel quinoidal oligothiophenes and anti-aromatic scaffold having tuned electronic structure to allow these compounds to be used as advanced electronic materials. The chemical structures and properties of these materials in the solid states were investigated in order to reveal the influence of the open-shell electronic nature on semiconducting properties in electronic devices. Although several researches have focused on the electronic interaction of open-shell molecules in the solid state,[10] systematic investigation concerning the influence of moderate biradical character on the semiconducting characteristics has not been conducted so far, because of the difficulty of estimation of the electronic state. The thesis is divided into four chapters.

In chapter 1, in order to increase the contribution of quinoidal electronic structure, quinoidal oligothiophenes containing benzo[*c*]thiophene unit were developed. Theoretical and experimental studies elucidated the structure−property relationships of the compounds, and OFET measurements revealed the influence of open-shell electronic configuration of quinoidal oligothiophenes on the semiconducting characteristics.

In chapter 2, I developed quinoidal terthiophenes having full benzo-annulation structure for further stabilization of the quinoidal closed-shell structure. The electronic state originated from the molecular structure was investigated by photophysical, electrochemical measurements, and X-ray crystallography. In order to investigate the potential application for OPV acceptor, photovoltaics characteristics based on the synthesized material was measured.

In chapter 3, quinoidal oligothiophenes having fluorine atoms at *β*-position of the thiophene core were developed to investigate the effects of fluorine substitution on structures, properties, and semiconducting characteristics. Also, donor/acceptor complex system based on the fluorinated compound was prepared and their properties were investigated.

In chapter 4, I designed and synthesized novel [4*n*] π conjugated system bearing heptafulvene segment to develop a new anti-aromatic framework. The origin of anti-aromaticity and semiconducting character of the compound was discussed by the results of experimental measurements and theoretical calculations.

References

1 (a) Abthony, J. E. *Chem. Rev.* **2006**, *106*, 5028. (b) Lu, L.; Zheng, T.; Wu, Q.; Schneider, A. M.; Zhao, D.; Yu, L. *Chem. Rev.* **2015**, *115*, 12666.

2 (a) Pron, A.; Gawrys, P.; Zagorska, M.; Djurado, D.; Demadrille, R. *Chem. Soc. Rev*. **2010**, *39*, 2577. (b) Miozzo, L.; Yassar, A.; Horowitz, G. *J. Mater. Chem.* **2010**, *20*, 2513. (c) Dou, L.; Liu, Y.; Hong, Z.; Li, G.; Yang, Y. *Chem. Rev.* **2015**, *115*, 12633. (d) Stępień, M.; Gońka, E.; Żyła, M.; Sprutta, N. *Chem. Rev.* **2017**, *117*, 3479. (e) Zhang, J.; Xu, W.; Sheng, P.; Zhao, G.; Zhu, D. *Acc. Chem. Res.* **2017**, *50*, 1654.

3 Tchitschibabin, A. E. Chem. Ber., **1907**, *40*, 1810.

4 Zeng, Z.; Shi, X.; Chi, C.; Navarrete, J. T. L.; Casado, J.; Wu. J. *Chem. Soc. Rev.* **2015**, *44*, 6578.

5 (a) Casado, J.; Ortiz, R. P.; Navarrete, J. T. L. *Chem. Soc. Rev.* **2012**, *41*, 5672.

6 Ortiz, R. P.; Casado, J.; González, S. R.; Hernández, V.; Navarrete, J. T. L.; Viruela, P. M.; Ortí, E.; Takimiya, K.; Otsubo, T. *Chem. − Eur. J.* **2010**, *16*, 470.

7 Nakano M. Excitation Energies and Properties of Open-Shell Singlet Molecules; Springer, Heidelberg, **2014**.

8 (a) Tobe, Y. *Chem. Rec.* **2015**, *15*, 86. (b) Shin, J.-Y.; Yamada, T.; Yoshikawa, H.; Awaga, K.; Shinokubo, H. *Angew. Chem., Int. Ed.* **2014**, *53*, 3096.

9 (a) Frederickson, C. K.; Rose, B. D.; Haley, M. M. *Acc. Chem. Res.* **2017**, 50, 977.

10 (a) Itkis, M. E.; Chi, X.; Cordes, A. M.; Haddon, R. C. *Science*, **2002**, *296*, 1443. (b) D. Small, V. Zaitsev, Y. Jung, S. V. Rosokha, M. Head-Gordon and J. K. Kochi, *J. Am. Chem. Soc.*, **2004**, *126*, 13850. (c) S. K. Mandal, S. Samanta, M. E. Itkis, D. W. Jensen, R. W. Reed, R. T. Oakley, F. S. Tham, B. Donnadieu and R. C. Haddon, *Science*, **2005**, *309,* 281. (d) Kubo, T.; Shimizu, A.; Sakamoto, M.; Uruichi, M.; Yakushi, K.; Nakano, M.; Shiomi, D.; Sato, K.; Takui, T.; Morita, Y.; Nakasuji, K. *Angew. Chem., Int. Ed*. **2005**, *44*, 6564.

Chapter 1

Development of Quinoidal Oligothiophenes Having Benzo[*c*]thiophene Unit

1.1 Introduction

Significant research interest continues to be focused on structurally well-defined π-conjugated oligomers, not only for the elucidation of fundamental structure–property relationship, but also for their applications in organic thin-film electronics such as OFETs and OPVs. [1,2] π-Conjugated compounds bearing quinoidal structures have been extensively investigated not only as a model structure of doped conducting arylene polymers, but also as a Wurster-type multi-redox system in Hünig's classification.[3] Among them, bis(dicyanomethylene)-substituted quinoidal compounds, which generate anionic aromatic state by accepting one or two electrons, exhibit a high electron-accepting ability as for instance the well-known tetracyano-*p*-quinodimethane.[4] Therefore, the extension of the π-conjugation of such quinoidal systems, typically tetracyano quinoidal oligothiophenes, have attracted great attention as promising electron-transporting (n-type) semiconductors.[5-13] Another unique feature of the quinoidal systems is an resonance between quinoidal and biradicaloid electronic structures,[14] which causes a configurational instability of quinoidal oligothiophenes (Figure 1.1(a)). The representative approach to increase the contribution of the quinoid character in oligothiophenes is the utilization of aromatic stabilization in a quinoidal form, which was accomplished by the introduction of a fused aromatic ring on the thiophene [*c*]bond, as observed in the first synthesis of poly(isothianaphthene) with a small band gap by Wudl et al.[15] In this context, quinoidal oligothiophenes containing thieno[3,4-*b*]thiophene have been extensively developed by Zhu et al (Figure 1.1(b)).[16] We envisioned that if the benzo[*c*]thiophene (isothianaphthene) quinoid unit can be incorporated into π-extended quinoidal structures, the high aromatic stabilization energy of this unit compared to that of benzo[*c*]thiophene would allow us to create quinoidal oligothiophenes that have potential as air-stable semiconducting materials. To pursue this possibility, new bis(dicyanomethylene)-substituted quinoidal oligothiophenes (**BTQ** and **BTQ-6**) containing 5,6-dialkylbenzo[*c*]thiophene units were designed (Figure 1.2). Furthermore, in order to increase the electron-accepting ability of **BTQ**, fluorine substituents were introduced to the β-positions of the quinoidal terthiophene (**BTQ-F**). In this work, the synthesis, properties, structures, and OFET characteristics of these compounds were reported. Although parent bis(dicyanomethylene)benzo[*c*]thiophene was synthesized and characterized by Cava et al. in 1993,[17] its π-extended derivative has not been reported so far.

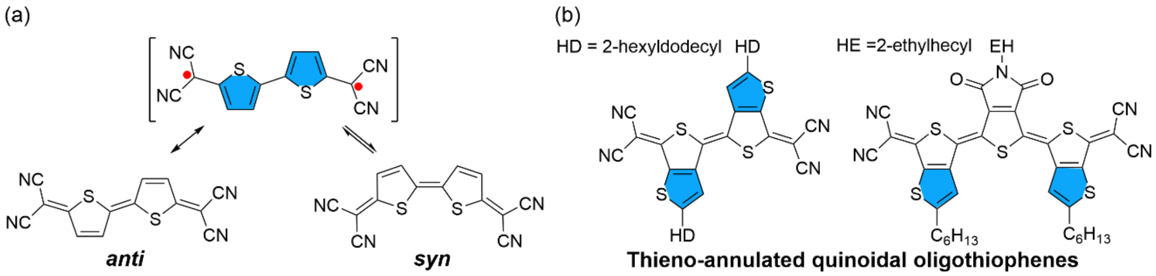

Figure 1.1. (a) Depiction of isomerization process of quinoidal thiophene. (b) Chemical structures of thieno-annulated quinoidal oligothiophenes.

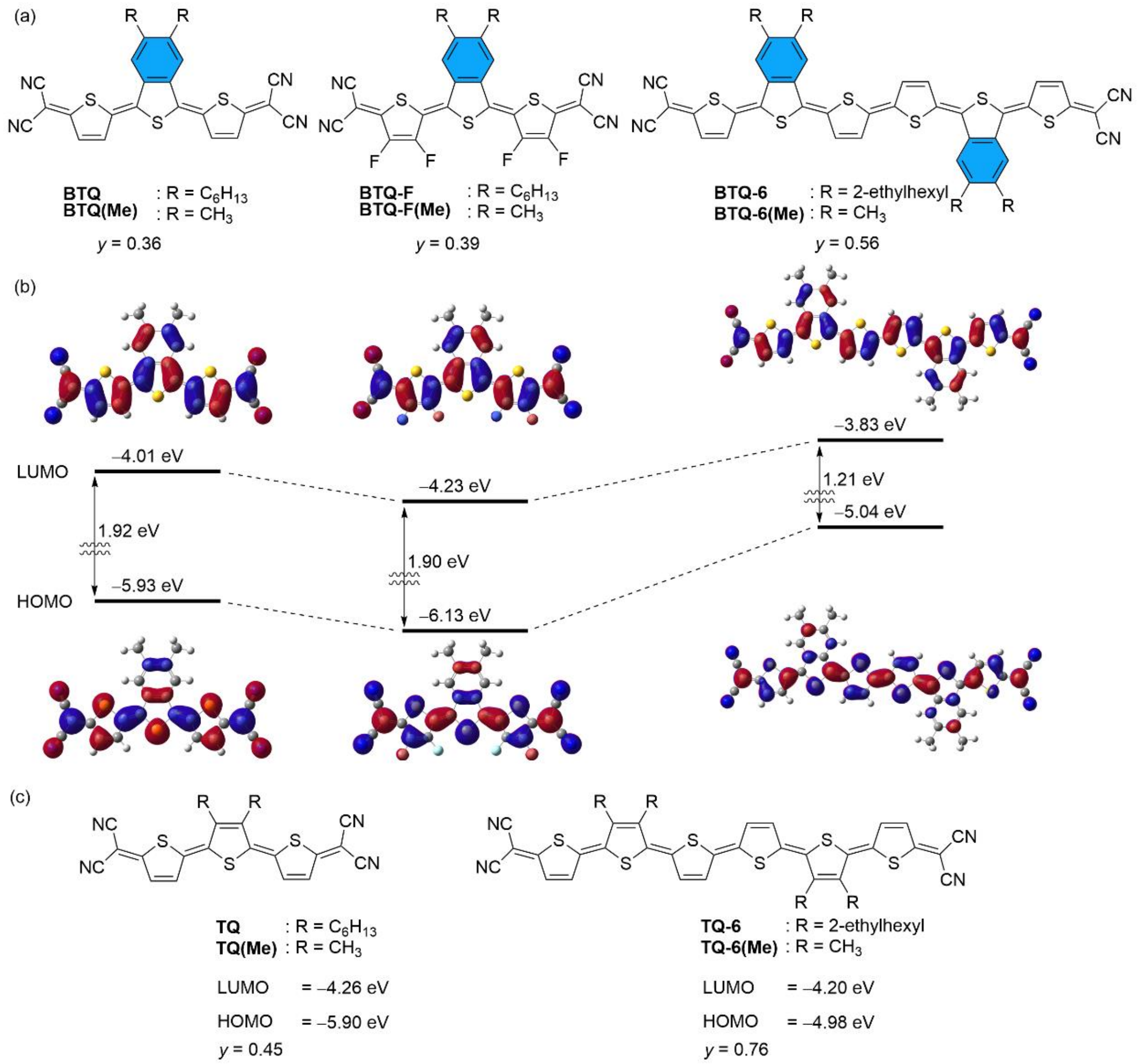

Figure 1.2. (a) Chemical structures of compounds investigated in this study. (b) Calculated energy levels and orbitals for model compounds **BTQ(Me)** (left), **BTQ-F(Me)** (center), and **BTQ-6(Me)** (right). (c) Chemical structures of reference compounds.

1.2 Theoretical study

To estimate the molecular structure and frontier orbital energies, density functional theory (DFT) calculation at the B3LYP/6-31G(d,p) level of theory was performed. All alkyl groups were replaced with methyl groups to ease the calculation. Optimized geometries of **BTQ(Me)**, **BTQ-F(Me)**, and **BTQ-6(Me)** showed a planar conformation which indicates that the introduction of the benzo-annulation in the central thiophene ring of terthiophene does not increase the distortion with respect to the dihedral angle (Figure 1.2(b)). LUMO energy level of **BTQ(Me)** is higher compared to that of **TQ(Me)** (Figure 1.2(b)(c)) but is still located at a low level of –4.01 eV. The substitution of hydrogen atoms in the thiophene rings with fluorine atoms for **BTQ-F(Me)** led to a further decrease of the LUMO energy level to –4.23 eV, while maintaining a similar HOMO–LUMO energy gap. It should be mentioned that the LUMO of both compounds is delocalized over the entire π-conjugated backbone including the annulated benzene ring, which is favorable for the intermolecular overlap of LUMOs between neighboring molecules in the solid state.[16b] On the other hand, the extension of π -conjugation from **BTQ(Me)** to **BTQ-6(Me)** mainly contributes to increasing the HOMO energy level from –5.93 eV to –5.04 eV. The singlet biradical character (y) of these quinoidal compounds was calculated by the natural orbital occupation number of the lowest unoccupied natural orbital (LUNO) with spin-unrestricted calculation at the UHF/6-31G(d) level.[18] Compounds **BTQ(Me)** and **BTQ-F(Me)** gave y values of 0.36 and 0.39, respectively. As expected, these values were smaller when compared to that of reference **TQ(Me)** ($y = 0.45$). Similarly, **BTQ-6(Me)** showed a lower y value of 0.56 compared to that of **TQ-6(Me)** (0.75). These results indicate that the introduction of the benzo[*c*]thiophene unit is effective in increasing the contribution of a quinoidal electronic structure in the ground state.

1.3 Synthesis and Characterization

Since 5,6-dialkyl derivatives of benzo[*c*]thiophene are not easily accessed from commercially available compounds, a rational synthetic procedure, which relies on the construction of the benzo[*c*]thiophene core from 2-pyridinyl ester was utilized (Scheme 1.1).[19] Methyl diester compound **1** was converted to 2-pyridinyl ester **2**, which was then reacted with Grignard reagents, generated from 2-bromothiophene or 2-bromo-3,4-difluoro-5-trimethylsilylthiophene, to give key intermediates **3a** and **3b**. Treatment of **3a** and **3b** with Davy’s reagent led to the formation of the benzo[*c*]thiophene core, and the obtained terthiophene derivatives were then treated with *N*-bromosuccinimide (NBS) to afford **4a** and **4b**. Finally, palladium-catalyzed coupling reactions of **4a** and **4b** with sodium dicyanomethanide, followed by oxidation with 2,3-dichloro-5,6-dicyano-*p*-benzoquinone (DDQ) to give **BTQ** and **BTQ-F** in 40% and 30% yield, respectively. The hexyl groups in the benzo[*c*]thiophene moiety ensured the good solubility of the molecules. The synthetic route of **BTQ-6** from **5** prepared similarly to **4** is also shown in Scheme 1.1. Note that 2-ethylhexyl groups on the benzo[*c*]thiophene core are essential to ensure proper solubility of the quinoidal thiophene 6-mer. On the other hand, pure **TQ-6** was due to the low chemical stability. The chemical structures of **BTQ**, **BTQ-F**, and **BTQ-6** were fully characterized by NMR and MS. Detailed synthesis and characterization were summarized in the experimental section.

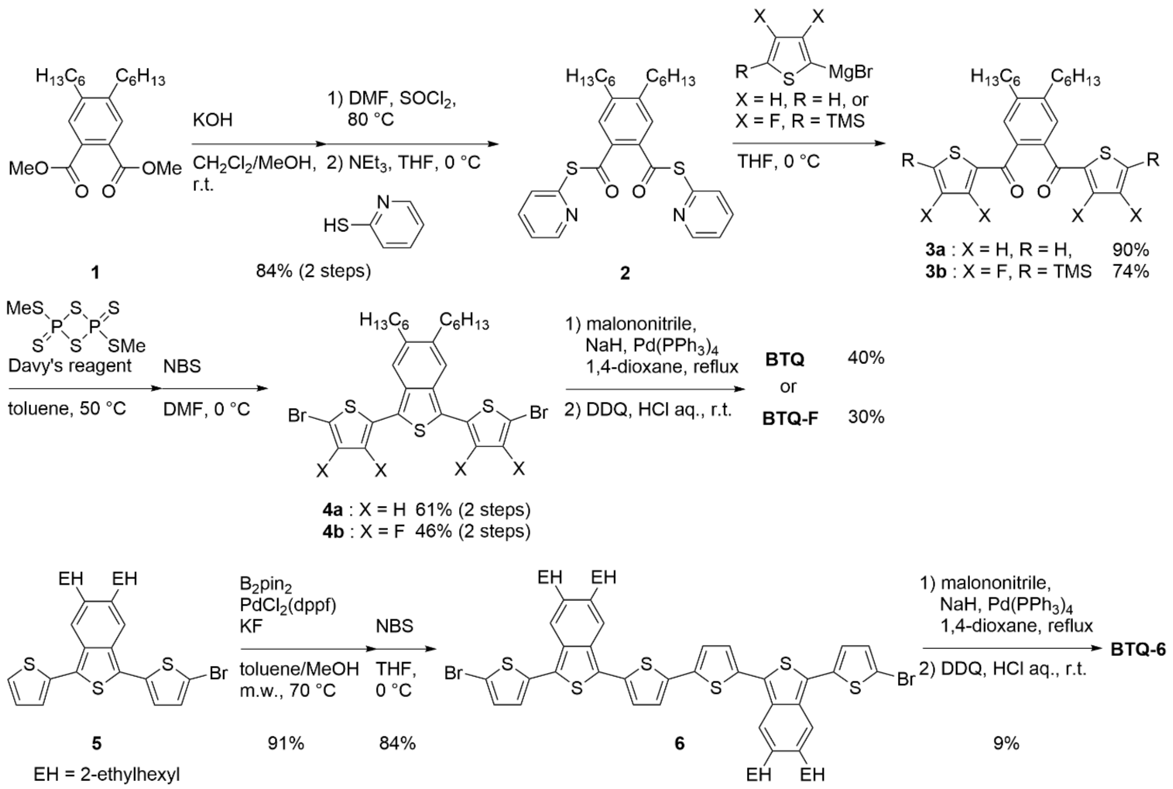

Scheme 1.1. Synthetic route of **BTQ**, **BTQ-F**, and **BTQ-6**.

In the ^{1}H NMR spectrum of **BTQ** at 25 °C, two sets of signals with an integration ratio of 10:1 were observed in the aromatic region (Figure 1.3),[5a] and all the peaks were assigned to *anti*-*anti* and *anti*-*syn* isomers of the quinoidal terthiophene backbone, respectively, by nuclear Overhauser effect measurements (Figure S1.1). On the other hand, almost one singlet signal was observed for **BTQ-F**. In order to investigate the isomerization behavior of **BTQ**, **BTQ-F**, and **TQ**, variable temperature (VT)-NMR measurements were performed at 0, 25, and 50 °C. As shown in Figure 1.3, the spectra of **BTQ** and **BTQ-F** showed little temperature dependence. Furthermore, the isomer ratio of **BTQ** is constant, irrespective of the temperature. On the other hand, although the spectrum of **TQ** showed two sets of signals at 0 °C similarly to that of **BTQ**, the small peaks that originate from the *anti*-*syn* isomer broadened at 25 °C and merged with the main peaks at 50 °C, implying the equilibrium between the two isomers provably via an aromatic biradical form. Similar *anti*–*syn* equilibrium was also reported on tetracyano bithiophene quinoid at 25 °C.[20] These results indicate that the quinoidal electronic structures of **BTQ** and **BTQ-F** are stabilized owing to the reduced contribution of biradicaloid structure by the benzo-annulation. In addition, the presence of fluorine atoms on the thiophene rings in **BTQ-F** induces not only steric congestion in the *syn* form but also intramolecular S–F attractive interactions, forming fixed *anti* configurations between adjacent thiophene rings.[21] In contrast, **BTQ-6** showed broad signals even under the low temperature of –45 °C (Figure S1.2), indicating the presence of equilibrium between the isomers.

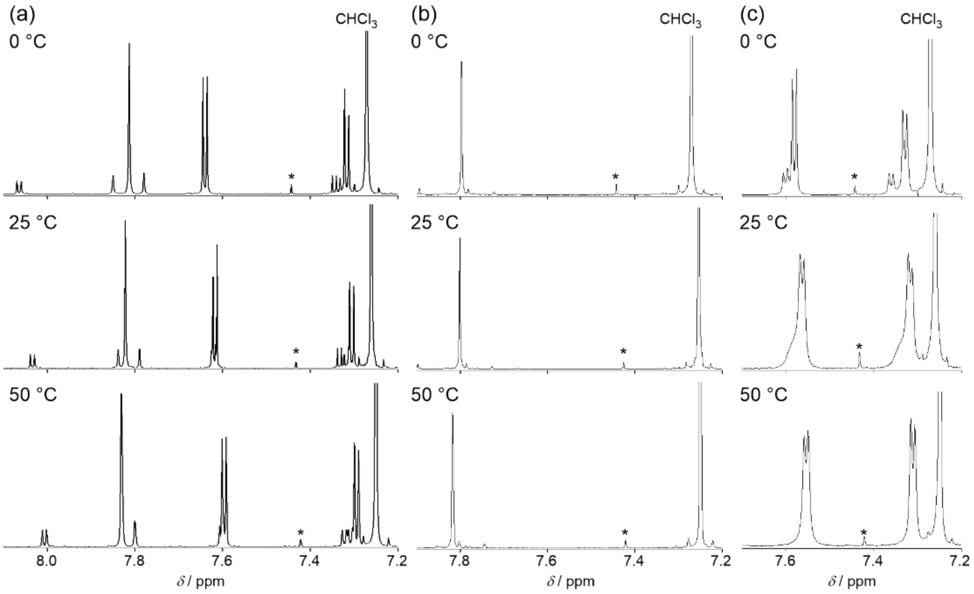

Figure 1.3. VT-NMR spectra of (a) **BTQ**, (b) **BTQ-F**, and (c) **TQ** in aromatic regions in $CDCl_3$. Signals pointed by asterisk are satellite peak of $CHCl_3$.

1.4 Photophysical and Electrochemical Properties

UV-vis-NIR absorption spectra of **BTQ**, **BTQ-F, BTQ-6**, and **TQ** in CH_2Cl_2 solutions are shown in Figure 1.4, and the photophysical data are summarized in Table 1.1. The absorption spectra of **BTQ** and **BTQ-F** showed similar shapes with an absorption maximum (λ_{max}) at around 640 nm, which are slightly blue-shifted compared to that of **TQ** (λ_{max} = 670 nm) (Figure 1.4(a)). These intense bands are mainly assigned to the HOMO–LUMO transition by time-dependent (TD)-DFT calculation at the B3LYP/6-31G (d,p) level of theory (see the experimental section). The qualitative trend of molar extinction coefficients (ε) for these compounds is in good accordance with estimated oscillator strength. As summarized in Table 1, the optical HOMO–LUMO energy gaps (ΔE_g^{opt}) of these compounds estimated from the onsets in the absorption spectra are found to be ca. 1.7 eV. The absorption spectrum of **BTQ-6** in a CH_2Cl_2 solution exhibited an absorption band at the near-infrared region (λ_{max} = 978 nm) with a large ε of 2.6×10^5 M cm^{-1}. This behavior is in contrast to a previous report where quinoidal sexithiophene showed a reduced molar extinction coefficient with concomitant appearance of marked absorptions in the visible region, compared to the corresponding quinoidal quinquethiophene. The reduced extinction coefficient was attributed to the high contribution of a biradical character,[14b] which indicates that the high ε of **BTQ-6** is rationalized by the higher contribution of quinoidal electronic structure owing to the presence of benzo[*c*]thiophene units in the framework. Compared to the solution spectra, well-structured shoulders with red-shifted λ_{max} were observed for **BTQ** and **BTQ-F** in thin films (Figure 1.4(b)). This phenomenon is attributed to the intermolecular electronic interactions of π–π stacked backbones, which are favorable for carrier transport in thin-film devices. The absorption spectrum of **BTQ-6** in thin film showed a broad absorption with the onset reaching 1800 nm. Such a large bathochromic shift was observed for quinoidal quarterthiophene.[9] In addition to the intermolecular electronic interactions, the existence of biradical character may have influence on this bathochromic shift.

Table 1.1. Photophysical and electrochemical properties.

Compounds	λ_{max} ($\varepsilon \times 10^5$) /nm (M^{-1} cm^{-1}) [a]	ΔE_g^{opt} /eV [a]	$\Delta E^{ox}_{1/2}$ /eV [b]	$\Delta E^{red}_{1/2}$ /eV [b]	E_{HOMO} /eV[c]	E_{LUMO} /eV[d]
BTQ	642 (0.9)	1.70	0.86	–0.74	–5.66	–4.06
BTQ-F	636 (1.0)	1.71	1.05	–0.50	–5.85	–4.30
BTQ-6	978 (2.6)	1.14	0.08	–0.54	–4.88	–4.26
			0.35	–0.61		
TQ	670 (1.1)	1.60	0.81	–0.58	–5.61	–4.23

[a] In CH_2Cl_2. [b] In CH_2Cl_2 containing 0.1 M $TBAPF_6$. V vs Fc/Fc^+. [c] $E_{HOMO} = -E^{ox}_{1/2} - 4.8$. [d] $E_{LUMO} = -E^{red}_{1/2} - 4.8$.

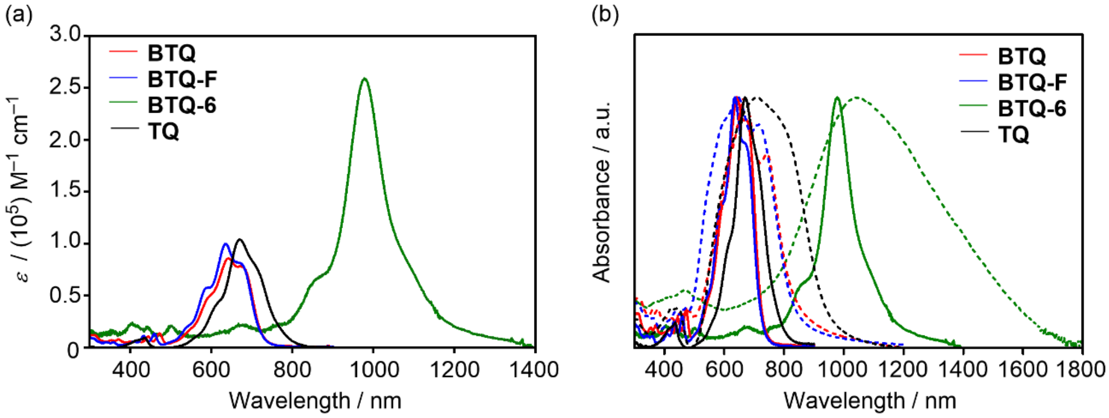

Figure 1.4. (a) UV-vis-NIR absorption spectra of **BTQ** (red) and **BTQ-F** (blue), **TQ** (black), and **BTQ-6** (green) in CH_2Cl_2 and (b) in CH_2Cl_2 (solid line) and thin films (dashed line).

The electrochemical properties of these compounds were investigated by cyclic voltammetry (CV) measurements in CH_2Cl_2 containing 0.1 M tetrabutylammonium hexafluorophosphate ($TBAPF_6$) as a supporting electrolyte. All potentials are calibrated against a ferrocene/ferrocenium (Fc/Fc^+) couple as a standard, and these values are listed in Table 1.1. As presented in Figure 1.5, the cyclic voltammograms of **BTQ**, **BTQ-F**, and **TQ** showed one reversible oxidation and reduction waves. The observed good reversibility indicates the stable formation of both cationic and anionic species. Integration of each peak area for these compounds implied the participation of one electron and two electrons in oxidation and reduction processes, respectively. As shown in Table 1.1, due to the electron-withdrawing nature of fluorine atoms, both half-wave oxidation potential ($E^{ox}_{1/2}$) and reduction potential ($E^{red}_{1/2}$) of **BTQ-F** are positively shifted compared to those of **BTQ**. Under the assumption that the energy level of Fc/Fc^+ is −4.8 eV below the vacuum level,[22–24] the LUMO energy levels (E_{LUMO}) of **BTQ** and **BTQ-F** were estimated to be –4.06 and –4.30 eV, respectively. These values are in good agreement with those estimated from the theoretical calculation. For **BTQ-6**, two reversible oxidation and reduction processes were observed. The E_{LUMO} and E_{HOMO} of **BTQ-6** estimated from the first $E^{red}_{1/2}$ and $E^{ox}_{1/2}$ were −4.26 and −4.88 eV, respectively, indicating that the extension of the quinoidal π-system leads to a significant rise of the HOMO energy level.

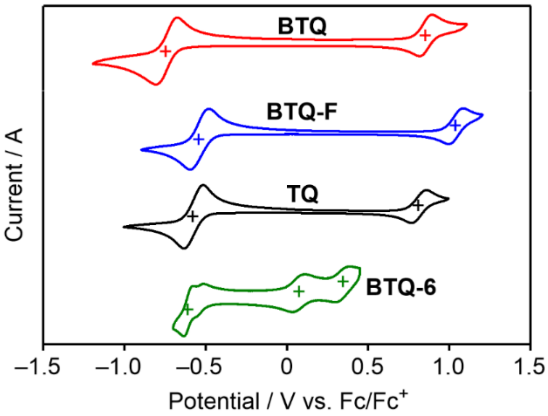

Figure 1.5. Cyclic voltammograms of **BTQ** (red) and **BTQ-F** (blue), **TQ** (black), and **BTQ-6** (green) in CH_2Cl_2 containing 0.1 M $TBAPF_6$.

1.5 X-Ray Single-Crystal Structures

The structure of **BTQ-F** was unambiguously determined by using X-ray crystallographic analysis of the crystals that were grown by the slow evaporation from a solution in ethyl acetate (EtOAc) and MeOH mixed solvent. As shown in Figure 1.6(a), the molecular structure of **BTQ-F** adopts all *anti* and planar conformation with dihedral angles of less than 2.7°. On the other hand, the distance of the intramolecular S–F contact (2.75 Å) is smaller than the sum of van der Walls radii of S and F atoms (3.27 Å), indicating the presence of nonbonding attractive interactions between these atoms. In the packing diagram, **BTQ-F** molecules are oriented in a face-to-face fashion with the minimum intermolecular π–π distances of 3.55 Å and 3.42 Å (a and b in Figure 1.6(b), respectively). On the basis of the calculation by the Amsterdam Density Functional (ADF) program at the PW91/TZP level, the transfer integrals between facial stacked structures of **BTQ-F** in the crystal were estimated. All the transfer integrals for electron transport (t_{LUMO}) and hole transport (t_{HOMO}) are summarized in Figure 1.6(c). **BTQ-F** showed a large t_{HOMO} and t_{LUMO} of 75.5 and 99.9 meV, respectively, which is expected to construct charge-carrier transporting pathway along the stacking direction.

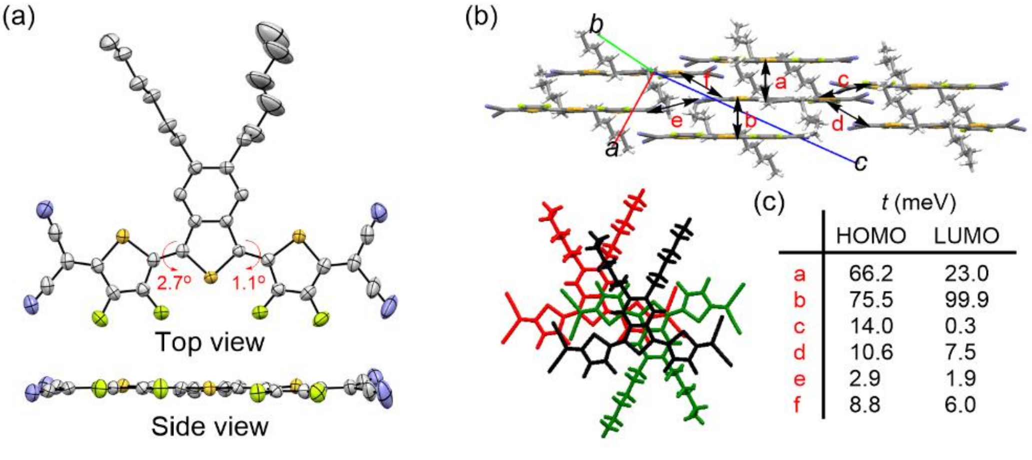

	HOMO	LUMO
a	66.2	23.0
b	75.5	99.9
c	14.0	0.3
d	10.6	7.5
e	2.9	1.9
f	8.8	6.0

Figure 1.6. (a) ORTEP drawing of molecular structure, (b) packing diagram from side view (top) and top view (bottom), and (c) estimated transfer integrals of HOMOs and LUMOs for **BTQ-F**.

1.6 Transistor Characteristics and Film Morphologies

To evaluate the semiconducting charge-transport characteristics of **BTQ**, **BTQ-F**, **BTQ-6**, and **TQ**, OFET devices based on thin films were fabricated. Although there have been several reports on high or finely tuned ambipolar OFETs of ter- and quater-thiophene quinoids,[5] the compounds in this work were characterized by using a conventional bottom-gate bottom-contact transistor configuration with similar fabrication conditions for all devices. The active layer was prepared by spin-coating from a 0.3 wt% $CHCl_3$ solution onto hexamethyldisilazane (HMDS)-modified Si/SiO_2 substrates. Thermal annealing was effective for improving the performance for **BTQ** and **BTQ-F**, and the current–voltage characteristics of best-performance devices are shown in Figure 1.7, S1.3, and S1.4. The hole (μ_h) and electron mobilities (μ_e) were extracted from the transfer characteristics at constant source–drain voltages. The corresponding device parameters as mobility, threshold voltage (V_{th}), and current on/off ratio (I_{on}/I_{off}) are summarized in Table 1.2. Both **BTQ** and **BTQ-F** revealed solely an electron transport with μ_e in the order of 10^{-3} cm^2 V^{-1} s^{-1} due to their low-lying LUMO energy levels. Furthermore, OFETs based on these compounds retained the same order of μ_e under air-exposed conditions. While the **TQ**-based device exhibited higher μ_e compared with **BTQ** and **BTQ-F**, the I_{on}/I_{off} ratio was quite low due to a high off source–drain current (Figure S1.4(d)). This might indicate that the ambipolar character of **TQ** framework effects the increase of carrier density even in the off state.[6b]

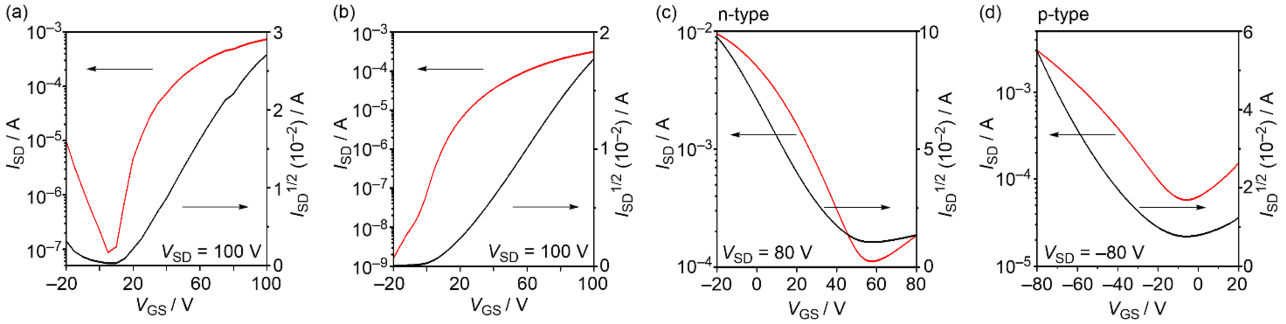

Figure 1.7. Transfer characteristics of OFETs using (a) **BTQ**, (b) **BTQ-F**, (c) **BTQ-6**, and (d) **BTQ-6**. V_{GS}, I_{SD}, and V_{SD} denotes gate voltage, source–drain current, and source–drain voltage, respectively.

Table 1.2. Field-effect transistor characteristics under vacuum and in air.

Compounds	Anneal temp. /°C	V_{th} /V	I_{on} / I_{off}	μ_e /cm^2 V^{-1} s^{-1} (μ_h /cm^2 V^{-1} s^{-1})
BTQ [a)]	170	15	10^4	3.4×10^{-3}
BTQ [b)]	170	18	10^5	2.5×10^{-3}
BTQ-F [a)]	170	13	10^5	1.2×10^{-3}
BTQ-F [b)]	170	–9.4	10^3	3.0×10^{-4}
TQ [a)]	As cast	35	10^1	3.3×10^{-2}
TQ [b)]	150	22	10^2	3.4×10^{-2}
BTQ-6	As cast	78	10^1	8.9×10^{-4}
	(As cast) [c)]	(–29) [c)]	(10^2) [c)]	(3.1×10^{-2}) [c)]

[a)] Under vacuum. [b)] In air. [c)] Hole-transporting characteristics are shown in parenthesis.

In order to investigate the film properties of these compounds, X-ray diffraction (XRD) and atomic force microscopy (AFM) measurements of these thin films on HMDS-modified Si/SiO_2 substrates were performed. As shown in Figure 1.8 and S1.5, these compounds exhibited clear diffraction peaks in XRD, indicating the formation of crystalline structures in thin films. The peak of **BTQ-F** at $2\theta = 6.2°$ can be indexed as a (011) diffraction peak with a *d* spacing of 14.2 Å according to the above-mentioned X-ray crystal structure analysis. Thus, the **BTQ-F** molecules are edge-on arranged with the stacking direction parallel to the SiO_2 surface. While AFM image of **BTQ** revealed crystal-shaped micrometer-sized grains, **BTQ-F** showed a rough film surface with large crystal grains (Figure 1.8). Both **BTQ** and **BTQ-F** maintained OFET responses under air-exposed conditions, irrespective of the difference of the film morphologies. This result indicates that the observed air-stability mainly originates from the thermodynamic stability, i.e, low LUMO energy level of less than −4.0 eV. As discussed above, the introduction of benzo-annulation led to the isomerization behavior different from that of **TQ** against temperature change. Therefore, to investigate the influence of the benzo-annulation on the device characteristics, temperature-dependent OFET measurements of **BTQ-** and **TQ**-based devices were performed. For these measurements, we performed the surface modification of the source and drain gold electrodes using hexadecanethiol to minimize the contact resistance between Au electrodes and active layer.[25] The decreased contact resistance was confirmed by the output characteristics (Figure S1.6).

As shown in Figure 1.9(a), OFETs using **BTQ** showed a decrease of electron mobility with decreasing the temperature. This phenomenon is in agreement with the temperature dependence of hopping dominated carrier transport.[26] The activation energy of **BTQ** was estimated to be 0.13 eV (Figure S1.7). On the other hand, the **TQ**-based device showed a reverse trend with a decrease in off current (Figure 1.9(b)). We speculate that the diminution of the biradical character for **BTQ** might facilitate the inherent electron transport, which means that biradicals act as both carriers. Although the presence of the sterically bulky 2-ethylhexyl groups may prevent dense π–π stacking, XRD results indicate the crystalline structures in thin films (Figure 1.8(c)). In fact, OFET devices based on **BTQ-6** showed not only an electron-transporting characteristics (8.9×10^{-4} $cm^2\ V^{-1}\ s^{-1}$) but also hole-transporting characteristics (3.1×10^{-2} $cm^2\ V^{-1}\ s^{-1}$). The appearance of p-type behavior can be explained by the increased HOMO energy levels. Note that the field-effect response for the quinoidal thiophene 6-mer is not reported so far. The OFET devices based on **BTQ**, **TQ**, and **BTQ-6** were stored and measured periodically under the air-exposed condition. As shown in Figure S1.8, compared to **TQ**, a decrease of carrier mobility is suppressed for benzo[c]thiophene-containing semicondutors. This result suggests that the introduction of the benzo-annulation to form a stabilized quinoidal electronic structure becomes an effective strategy in developing new semiconducting materials.

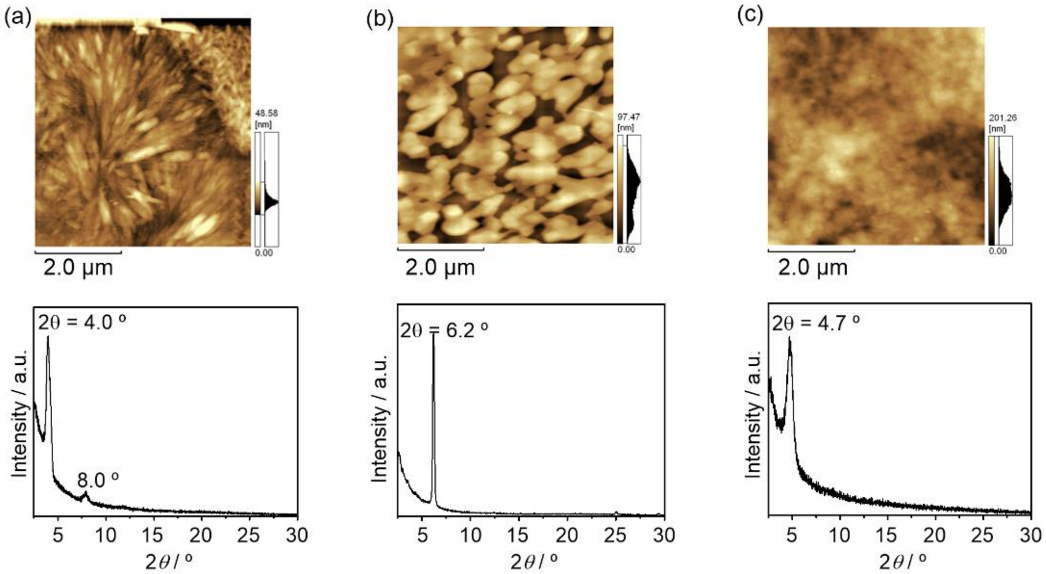

Figure 1.8. AFM height images and XRD data of (a) **BTQ** and (b) **BTQ-F**, and (c) **BTQ-6**.

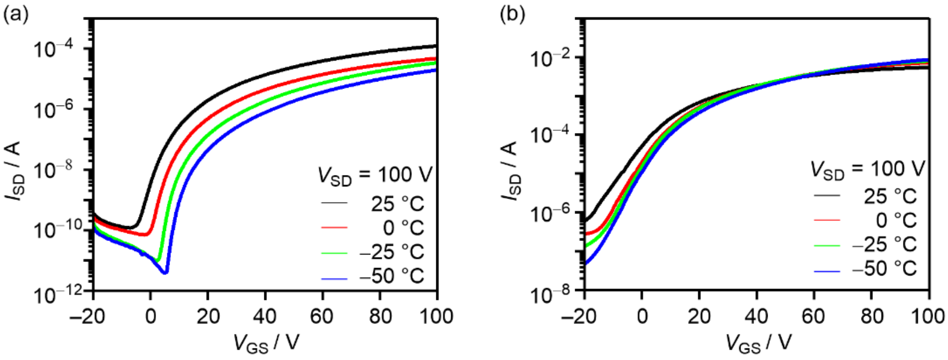

Figure 1.9. Temperature-dependent transfer characteristics of the 1-hexadecanethiol-treated OFETs using (a) **BTQ** and (b) **TQ**.

1.7 Conclusion

In summary, to investigate the influence of benzo-annulation on the stabilization of quinoidal electronic structure, the synthesis of new bis(dicyanomethylene)-substituted quinoidal oligothiophenes containing benzo[*c*]thiophene units was successfully achieved. Also, quinoidal oligothiophenes containing both benzo[*c*]thiophene unit and fluorinated thiophenes was developed. Theoretical calculations as well as experimental results indicate that the introduction of benzo[*c*]thiophene into oligothiophene π-conjugated quinoid system is effective in stabilizing quinoidal electronic structures. These molecules showed good electron-transporting characteristics, and the extension of π-conjugation from thiophene 3-mer to 6-mer led to the appearance of both hole- and electron-transporting characteristics. These results show that quinoidal π-conjugated systems containing benzo[*c*]thiophene units have potential as candidates for semiconducting materials using stabilized quinoidal structures.

1.8 Experimental Section

Supplementary Figures

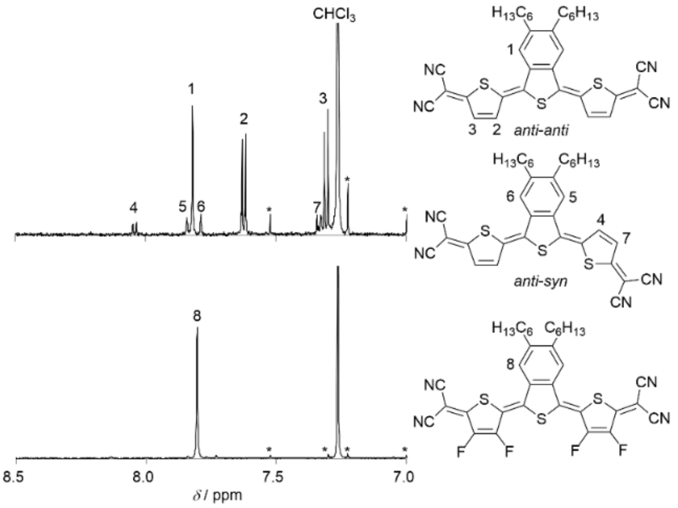

Figure S1.1. Magnified ^{1}H NMR spectra of **BTQ** and **BTQ-F** at room temperature in CDCl$_3$.

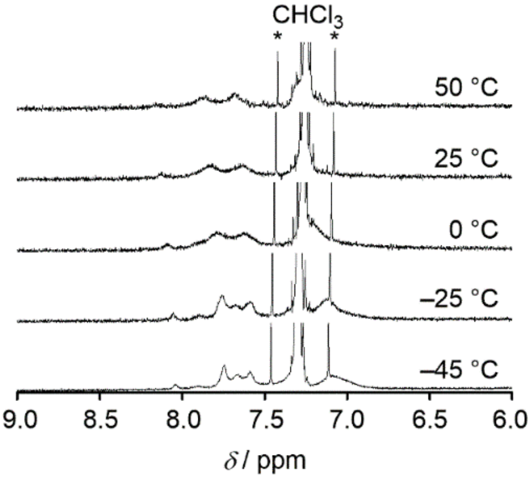

Figure S1.2. VT-NMR spectra of **BTQ-6** in aromatic regions in CDCl$_3$. Signals pointed by asterisk are satellite peak of CHCl$_3$.

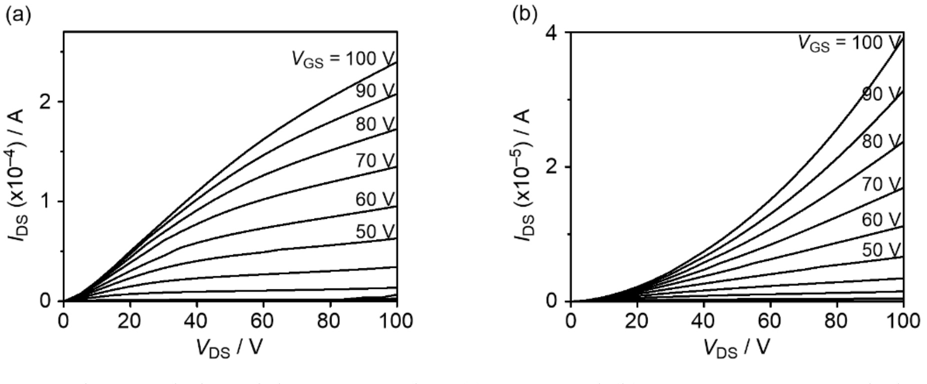

Figure S1.3. Output characteristics of the OFET using (a) **BTQ** and (b) **BTQ-F** at source–drain voltage of 100 V. I_{DS}, and V_{DS} denotes source–drain current and source–drain voltage, respectively.

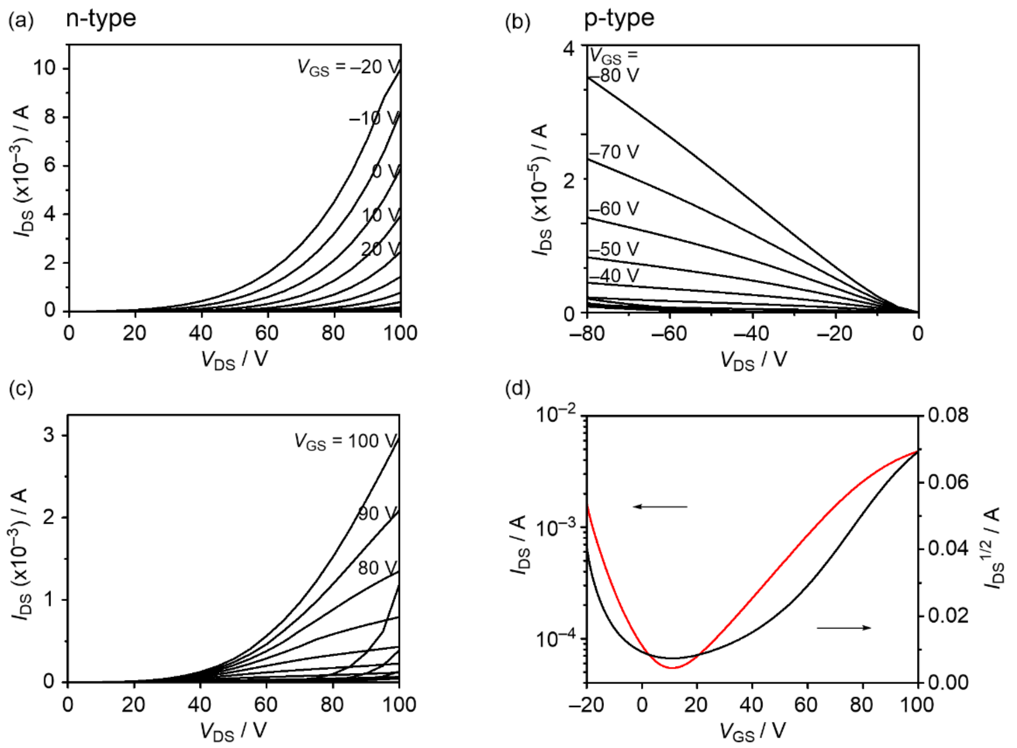

Figure S1.4. Output characteristics of (a) **BTQ-6**, (b) **BTQ-6**, and (c) **TQ**. (d) Transfer characteristics of OFETs using **TQ**.

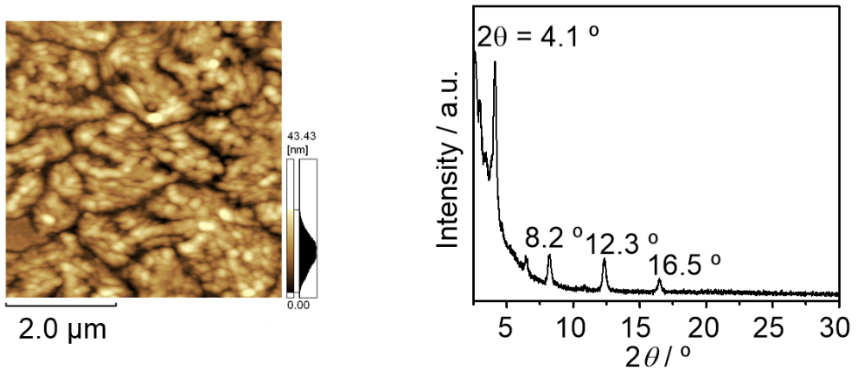

Figure S1.5. AFM images and XRD data of **TQ**.

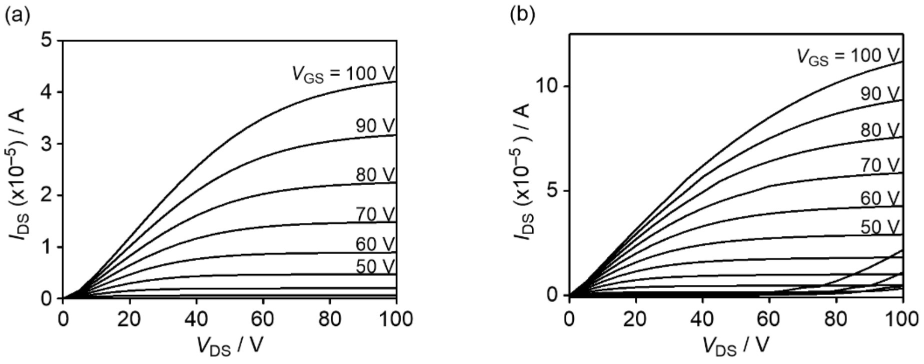

Figure S1.6. Output characteristics of the 1-hexadecanethiol-treated OFETs using (a) **BTQ** and (b) **TQ**.

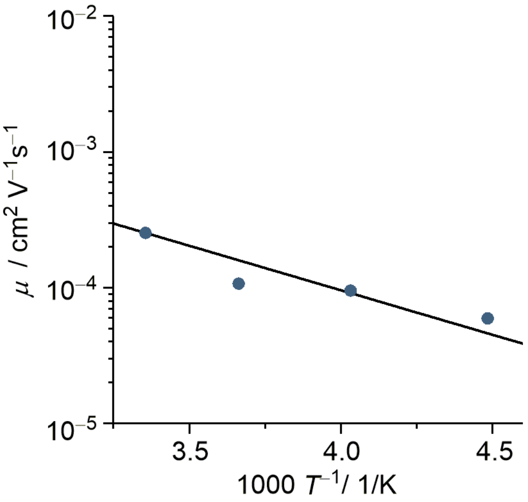

Figure S1.7. Temperature dependence of carrier mobility for **BTQ**. Black solid lines were fitted from the equation $\mu = \mu_0 \exp(-E_a k^{-1} T^{-1})$, where E_a is an activation energy, k is Boltzmann's constant, and μ_0 is the mobility at $1000/T = 0$.

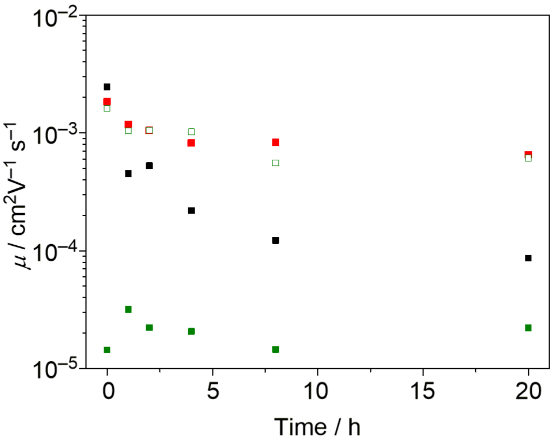

Figure S1.8. Plots of electron mobility against time for **BTQ** (red square), **TQ** (black square), and **BTQ-6** (green square). Hole mobility of **BTQ-6** is represented as empty green square.

General Information

Column chromatography was performed on silica gel. KANTO Chemical silica gel 60N (40–50 µm). Thin-layer Chromatography (TLC) plates were visualized with UV light. Preparative gel-permeation chromatography (GPC) was performed on a Japan Analytical LC-918 equipped with JAI-GEL 1H/2H. ^{1}H and ^{13}C NMR spectra were recorded on a JEOL JNM-ECS400 or JEOL JNM-ECA600 spectrometer in $CDCl_3$ with tetramethylsilane (TMS) as an internal standard. ^{19}F NMR spectra were recorded on a JEOL JNM-ECA600 spectrometer in $CDCl_3$. Data are reported as follows: chemical shift in ppm (δ), multiplicity (s = singlet, d = doublet, t = triple, m = multiplet, br = broad), coupling constant (Hz), and integration. Mass spectra were obtained on a Shimadzu AXIMA-TOF. UV-vis spectra were recorded on a Shimadzu UV-3600 spectrophotometer. All spectra were obtained in spectrograde solvents. Cyclic voltammetry was carried out on a BAS CV-620C voltammetric analyzer using a platinum disk as the working electrode, platinum wire as the counter electrode, and Ag/AgNO$_3$ as the reference electrode at a scan rate of 100 mV s^{-1}. Elemental analyses were performed on PerkinElmer LS-50B by the elemental analysis section of the Comprehensive Analysis Center (CAC) of ISIR, Osaka University. The surface structures of the deposited organic film were observed by atomic force microscopy (Shimadzu, SPM9600), and the film crystallinity was evaluated by an X-ray diffractometer (Rigaku, SmartLab). X-ray diffraction patterns were obtained using Bragg-Brentano geometry with CuKα radiation as an X-ray source with an acceleration voltage of 45 kV and a beam current of 200 mA. The scanning mode was set to 2θ–θ scans between 2º–30º with scanning steps of 0.01º.

OFET Device Fabrication and Evaluation

The field-effect electron mobility was measured using bottom-gate bottom-contact OFET devices. The p-doped silicon substrate functions as the gate electrode. A thermally grown silicon oxide (SiO$_2$) dielectric layer on the gate substrate has 300 nm thick and a capacitance of 10.0 nF cm^{-2}. Interdigital source and drain electrodes were constructed with gold (30 nm) that were formed on the SiO$_2$layer. The channel width (*W*) and channel length (*L*) are 38 mm and 5 μm, respectively. The silicon oxide surface was first washed with toluene, acetone, purified water and 2-propanol. It was then activated by ozone treatment and pretreated with ODTS or HMDS. The semiconducting layer was fabricated by spin coating from 0.3 wt% chloroform solution at 1000 rpm for 1 min onto the substrate in air for **BTQ**, **BTQ-F** and **TQ**, 0.1 wt% chloroform solution at 1000 rpm for 1 min onto the substrate in air for **BTQ-6**, followed by annealing for 90 min at various temperatures under a vacuum condition (10^{-3}Pa). The characteristics of the OFETs were measured at room temperature under a pressure of 10^{-3} Pa by using a KEITHLEY 4200 semiconductor parameter analyzer. The μ_e was calculated in the saturated region by the following equation.

$$I_{DS} = \frac{W}{2L} C_i \mu (V_{GS} - V_{th})^2$$

Current on/off ratio was determined from the I_D sat V_{GS}= 0 V (I_{off}) and V_{GS}= 100 V (I_{on}).

Computational Details

All calculations were conducted using Gaussian 09 program. The geometry was optimized with the restricted Becke Hybrid (B3LYP) at 6-31 G(d,p) level.

TD-DFT Calculation

BTQ(Me)

Excited State 1: Singlet-A 2.30 eV 538 nm *f* = 1.84 <S**2>=0.000

HOMO–1 > LUMO+1 0.11515

HOMO > LUMO 0.69738

BTQ-F(Me)

Excited State 1: Singlet-A 2.30 eV 538 nm *f* = 2.01 <S**2>=0.000

HOMO–1 > LUMO+1 0.10961

HOMO > LUMO 0.69954

TQ(Me)

Excited State 1: Singlet-A 2.11 eV 589 nm *f* = 1.98 <S**2>=0.000
  HOMO > LUMO 0.70613
  HOMO < LUMO 0.11819

Synthesis

Unless stated otherwise, all reagents were purchased from commercial sources and used without purification. Compounds **1** and 2-bromo-3,4-difluoro-5-trimethylsilyl-thiohene were prepared by the reported procedures.[27,28]

Synthesis of ***2***: Compound **1** (1.44 g, 4.41 mmol) was placed in a round-bottom flask and dissolved in methanol (4.8 mL). Potassium hydroxide (988 mg, 17.6 mmol) was added to the mixture at room temperature. After stirring for 5 min, water was poured into the reaction mixture. The aqueous layer was washed with ether to remove unreacted ester compounds and then acidified with 6 *N* hydrochloric acid (HCl). The precipitate was extracted with ether and dried over $MgSO_4$. The solvent was removed under reduced pressure to give dicarboxylic acid **A** as a white solid (1.3 g). ^{1}H NMR (400 MHz, DMSO-d_6): δ 0.86 (t, *J* = 7.2 Hz, 6H), 1.21-1.39 (m, 12H), 1.45-1.57 (m, 4H), 2.58-2.66 (m, 4H), 7.43 (s. 2H), 12.5-13.2 (br, 2H). This compound was used for next step without further purification. **A** (550 mg, 1.64 mmol) was placed in a round-bottom flask. Thionyl chloride (10 mL) and DMF as a catalyst was added to the flask, and the reaction mixture was reflux for overnight. After removal of thionyl chloride and DMF under reduced pressure, the residue was resolved in THF (5.8 mL). Then, this solution was added to a solution of triethylamine (0.55 mL) and 2-mercaptopyridine (362 mg, 3.28 mmol) in THF (7.5 mL) at 0 °C. After vigorously stirring for 10 min., the reaction was quenched by addition of 2% HCl aq.. The resultant mixture was extracted with $CHCl_3$. The combined organic layer was washed with 10% sodium hydroxide (NaOH) aq., and water. After drying over with $MgSO_4$, the solvent was removed under reduced pressure. The residue was purified by column chromatography on silica gel (hexane:EtOAc = 5:3) to give **2** (810 mg, 84%, 2 steps) as a pale yellow solid. ^{1}H NMR (400 MHz, $CDCl_3$, TMS): δ 0.91 (t, *J* = 7.0 Hz, 6H), 1.30-1.46 (m, 12H), 1.55-1.65 (m, 4H), 2.66-2.72 (m, 4H), 7.28-7.32 (m, 2H), 7.65 (s, 2H), 7.74-7.82 (m, 4H), 8.62-8.65 (m, 2H); ^{13}C NMR (100 MHz, $CDCl_3$, TMS): δ 13.4, 21.8, 28.6, 30.0, 30.9, 31.9, 122.9, 128.8, 129.7, 133.6, 136.5, 144.7, 149.6, 150.9, 189.4; HRMS (ESI) *m/z* 543.2107 ($[M+Na]^+$) ($[M+Na]^+$, Calcd 543.2110).

Synthesis of ***3a***: Compound **2** (810 mg, 1.56 mmol) was placed in a two-necked-bottomed flask and resolved in THF (11 mL). 2-Thienyl magnesium bromide (3.12 mmol, 0.5 M in THF) was added slowly to the solution at 0 °C. The reaction mixture was stirred for 30 min. and then quenched by addition of 10% HCl aq.. The resultant mixture was extracted with $CHCl_3$, and the combined organic layer was washed with 10% NaOH aq., $NaHCO_3$ aq., and water. After drying over with $MgSO_4$, the solvent was removed under reduced pressure. The residue was purified by column chromatography on silica gel (hexane:EtOAc = 8:1) to give **3a** (660 mg, 90%) as a pale yellow solid. ^{1}H NMR (400 MHz, $CDCl_3$, TMS): δ 0.90 (t, *J* = 7.0 Hz, 6H), 1.28-1.46 (m, 12H), 1.59-1.67 (m, 4H), 2.68-2.74 (m, 4H), 7.06 (dd, *J* = 5.0 and 3.6 Hz, 2H), 7.46 (dd, *J* = 3.6 and 1.2 Hz, 2H), 7.51 (s, 2H), 7.64 (dd, *J* = 5.0 and 1.2 Hz, 2H); ^{13}C NMR (100 MHz, CDCl$_3$, TMS): δ 14.1, 22.6, 29.4, 30.9, 31.7, 32.7, 127.9, 130.2, 134.5, 134.8, 136.9, 143.8, 144.5, 188.5; MS MALDI-TOF (1,8,9-trihydroxyanthracene matrix) *m/z* 466.03 (M$^+$, Calcd 465.93); Anal. Calcd for $C_{28}H_{34}O_2S_2$: C 72.06, H 7.34; found: C 71.86, H 7.34.

*Synthesis of **3b***: Compound **2** (433 mg, 0.831 mmol) was placed in a two-necked-bottomed flask and dissolved in THF (3.5 mL). The Grignard solution (1.83 mmol, 0.5 M in THF), which was generated in situ by refluxing of 2-bromo-3,4-difluoro-5-trimethylsilylthiophene and magnesium for 30 min., was added slowly to the solution at 0 °C. The reaction mixture was stirred for 2 h and then quenched by addition of 10% HCl aq.. Purification was conducted by following the same procedure as **3a** to give **3b** (420 mg 74%) as a pale yellow oil. ^{1}H NMR (400 MHz, CDCl$_3$, TMS): δ 0.35(s, 18H), 0.90 (t, J = 6.8 Hz, 6H), 1.30-1.42 (m, 12H), 1.58-1.64 (m, 4H); ^{19}F NMR (565 MHz, CDCl$_3$): δ –125.7, –122.9; ^{13}C NMR (150 MHz, CDCl$_3$, TMS): δ –0.9, 14.4, 22.9, 29.7, 31.1, 32.0, 33.0, 125.2, 125.6, 130.3, 136.4, 144.8, 146.4, 149.7, 185.5; MS MALDI-TOF (1,8,9-trihydroxyanthracene matrix) *m/*z 681.88 (M$^+$, Calcd 682.24); Anal. Calcd for $C_{34}H_{46}F_4O_2S_2Si_2$: C 59.79, H 6.79; found: C 59.56, H 6.64.

*Synthesis of **4a***: Davy's reagent (623 mg, 2.19 mmol) was added to a solution of **3a** (930 mg, 1.99 mmol) in toluene (61 mL) and stirred at 50 °C. After stirring for 1 h, the solvent was removed under vacuum and ethanol (61 mL) was added. This solution was stirred at 50 °C for 30 min. The solvent was removed under reduced pressure and purified by column chromatography on silica gel (hexane) to give the intermediate **B** (810 mg) as a red solid. NBS (619 mg, 1.74 mmol) was added in four portions to a solution of the **B** (810 mg) in DMF (28 mL) at 0 °C. After stirring for 2 h at 0 °C, the reaction was quenched by addition of water. The combined organic was extracted with EtOAc and washed with water. The solvent was removed under reduced pressure and purified by column chromatography on silica gel (hexane:CH_2Cl_2 = 1:1), followed by purification with preparative GPC (CHCl$_3$) to give **4a** (760 mg, 61%) as a red solid. ^{1}H NMR (400 MHz, CDCl$_3$, TMS): δ 0.91 (t, J = 6.8 Hz, 6H), 1.29-1.49 (m, 12H), 1.60-1.68 (m, 4H), 2.62-2.68 (m, 4H), 7.05 (d, J = 2.0 Hz, 2H), 7.09 (d, J = 2.0 Hz, 2H), 7.60 (s, 2H); ^{13}C NMR (100 MHz, CDCl$_3$, TMS): δ 14.1, 22.7, 29.4, 30.8, 31.8, 33.1, 111.8, 119.4, 124.1, 125.4, 130.6, 134.9, 137.4, 140.0; MS MALDI-TOF (1,8,9-trihydroxyanthracene matrix) *m/z* 623.55 (M$^+$, Calcd 624.00); Anal. Calcd for $C_{28}H_{32}Br_2S_3$: C 53.85, H 5.16; found: C 53.76, H 5.29.

*Synthesis of **4b***: Compound **4b** was synthesized from 3**b** with a yield of 46% by following the procedure used for the preparation of **4a**. Red solid; ^{1}H NMR (400 MHz, CDCl$_3$, TMS): δ 0.91 (t, J = 6.8 Hz, 6H), 1.31-1.50 (m, 12H), 1.59-1.68 (m, 4H), 2.67 (t, J = 7.6 Hz ,4H), 7.50 (s, 2H); ^{19}F NMR (565 MHz, CDCl$_3$): δ –132.3, –131.4; ^{13}C NMR (150 MHz, CDCl$_3$, TMS): δ 14.1, 22.7, 29.3, 30.7, 31.8, 33.1, 90.9, 114.2, 119.3, 120.2, 135.7, 140.6, 140.7, 144.9; MS MALDI-TOF (1,8,9-trihydroxyanthracene matrix) *m/z* 695.02 (M$^+$, Calcd 695.96); Calcd for $C_{28}H_{28}Br_2F_4S_3$: C 48.28, H 4.05; found: C 48.22, H 4.23.

*Synthesis of **BTQ***: Sodium hydride (60% in oil) (20 mg, 0.51 mmol) was added to a suspension of malononitrile (17 mg, 0.25 mmol) in anhydrous 1,4-dioxane (3.0 mL) under nitrogen atmosphere and stirred for 10 min at room temperature. To this mixture was added **4a** (66 mg, 0.11 mmol) and Pd(PPh$_3$)$_4$ (12 mg, 0.011 mmol). After stirring for 4 h at reflux, the reaction was quenched by adding 1.0 M HCl aq., and then DDQ (36 mg, 0.16 mmol) was added to the mixture. After stirring for 30 min. at room temperature, the resulting mixture was extracted with CH_2Cl_2. The combined organic was washed with water and dried over $MgSO_4$. The solvent was removed under reduced pressure, and the residue was purified by column chromatography on silica gel (hexane:CH_2Cl_2 = 5:1) to give **BTQ** (25 mg, 40%) as a blue solid. ^{1}H NMR (400 MHz, $CDCl_3$, TMS): δ 0.92 (t, J = 7.0 Hz, 6H), 1.32-1.52 (m, 12H), 1.62-1.71 (m, 4H), 2.80-2.86 (m, 4H), 7.31 (d, J = 2.8 Hz, 2H), 7.62 (d, J = 2.8 Hz, 2H), 7.82 (s, 2H); ^{13}C NMR (150 MHz, $CDCl_3$, TMS): δ 14.1, 22.6, 29.3, 31.1, 31.6, 33.5, 67.9, 113.1, 114.0, 126.6, 129.8, 129.9, 137.1, 140.4, 141.7, 147.0, 172.6; MS MALDI-TOF (1,8,9-trihydroxyanthracene matrix) *m/z* 591.98 (M^+, Calcd 592.18); Calcd for $C_{34}H_{32}N_4S_3$: C 68.88, H 5.44, N 9.45; found: C 68.56, H 5.45, N 9.38.

*Synthesis of **BTQ-F***: Compound **BTQ-F** was synthesized from **4b** with a yield of 30% by following the procedure used for the preparation of **BTQ**. Blue solid; ^{1}H NMR (400 MHz, $CDCl_3$, TMS): δ 0.92 (t, J = 6.8 Hz, 6H), 1.30-1.52 (m, 12H), 1.63-1.72 (m, 4H), 2.84 (t, J = 7.6 Hz, 4H), 7.80 (s, 2H); ^{19}F NMR (565 MHz, $CDCl_3$): δ –135.8, –111.8; ^{13}C NMR (150 MHz, $CDCl_3$, TMS): δ 14.1, 22.6, 29.2, 30.7, 31.6, 33.3, 67.7, 111.2, 111.3, 112.6, 112.9, 126.8, 136.6, 140.5, 142.4, 147.6, 152.0; MS MALDI-TOF (1,8,9-trihydroxyanthracene matrix) *m/z* 663.84 (M^+, Calcd 664.14); HRMS (APCI) *m/z* 665.1479 ($[M+H]^+$) ($[M+H]^+$, Calcd 665.1485).

*Synthesis of **6***: **5** (110 mg, 0.183 mmol), bis(pinacolato)diboron (24.7 mg, 0.0967 mmol), $PdCl_2(dppf)\cdot CH_2Cl_2$ (15.0 mg, 0.0183 mmol), potassium fluoride (52.2 mg, 0.894 mmol), and toluene/methanol (2.5/2.5 mL) were placed in a microwave proof walled glass vial equipped with a snap cap. The glass vial was purged nitrogen, securely sealed, and heated in a microwave reactor with keeping a temperature at 70 °C for 15 min. The solvent was removed under reduced pressure and purified by column chromatography on silica gel (hexane:$CHCl_3$ = 1:1) to give **C** (87 mg, 91%) as a violet solid. ^{1}H NMR (400 MHz, $CDCl_3$, TMS): δ 0.86-0.96 (m, 24H), 1.22-1.46 (m, 32H), 1.60-1.70 (m, 4H), 2.54-2.70 (m, 8H), 7.15 (dd, J = 5.0, 3.7 Hz, 2H), 7.24 (d, J = 4.0 Hz, 2H), 7.27 (d, J = 4.0 Hz, 2H), 7.34 (dd, J = 3.7, 0.9 Hz, 2H), 7.37 (dd, J = 5.0, 0.9 Hz, 2H), 7.68 (s, 2H), 7.71 (s, 2H). NBS (39 mg, 0.220 mmol) was added in two portions to a solution of **C** (115 mg, 0.110 mmol) in THF (14 mL) at 0 °C. After stirring for 2 h at room temperature, the reaction was quenched by addition of water. The resulting mixture was extracted with EtOAc. The organic layer was washed with water and dried over $MgSO_4$. The solvent was removed under reduced pressure and purified by column chromatography on silica gel ($CHCl_3$), followed by purification with preparative GPC ($CHCl_3$) to give **6** (111 mg, 84%) as a violet solid. ^{1}H NMR (400 MHz, $CDCl_3$, TMS): δ 0.85-0.96 (m, 24H), 1.24-1.46 (m, 32H), 1.59-1.69 (m, 4H), 2.54-2.68 (m, 8H), 7.06 (d, J = 4.1 Hz, 2H), 7.09 (d, J = 4.1 Hz, 2H), 7.24 (d, J = 3.7 Hz, 2H), 7.27 (d, J = 3.7 Hz, 2H), 7.56 (s, 2H), 7.02 (s, 2H); ^{13}C NMR (100 MHz, $CDCl_3$, TMS): δ 10.9, 14.2, 23.2, 25.5, 28.8, 32.5, 37.7, 39.8, 111.6, 120.8, 121.2, 123.6, 124.3, 125.1, 125.7, 130.6, 134.5, 134.9, 135.1, 136.5, 137.6, 138.9, 139.1; HRMS (APCI) *m/z* 1201.2991 ($[M+H]^+$) ($[M+H]^+$, Calcd 1201.3003).

*Synthesis of **BTQ-6***: Sodium hydride (60% in oil) (15 mg, 0.37 mmol) was added to a suspension of malononitrile (13 mg, 0.19 mmol) in anhydrous THF (2.2 mL) under nitrogen atmosphere and stirred for 10 min. at room temperature. To this mixture was added compound **6** (92 mg, 0.077 mmol) and $Pd(PPh_3)_4$ (8.8 mg, 0.0077 mmol).

After stirring at reflux temperature for 7 h, the reaction was quenched by adding 1.0 M HCl aq., and then DDQ (17 mg, 0.077 mmol) was added to the mixture. After stirring at room temperature for 30 min., the resulting mixture was extracted with $CHCl_3$. The combined organic was washed with water and dried over $MgSO_4$. The solvent was removed under reduced pressure, and the residue was purified by column chromatography on silica gel (hexane:CH_2Cl_2 = 5:1), followed by purification with preparative GPC ($CHCl_3$) to give **BTQ-6** (8 mg, 9%) as a black solid. ^1H NMR (400 MHz, $CDCl_3$, TMS): δ 0.78-1.04 (m, 24H), 1.14-1.48 (br, 32H), 1.60-1.74 (br, 4H), 2.62-2.84 (br, 8H). Proton signals of aromatic region were observed as broad signals; HRMS (APCI) *m/z* 1169.4767 ($[M+H]^+$) ($[M+H]^+$, Calcd 1169.4780).

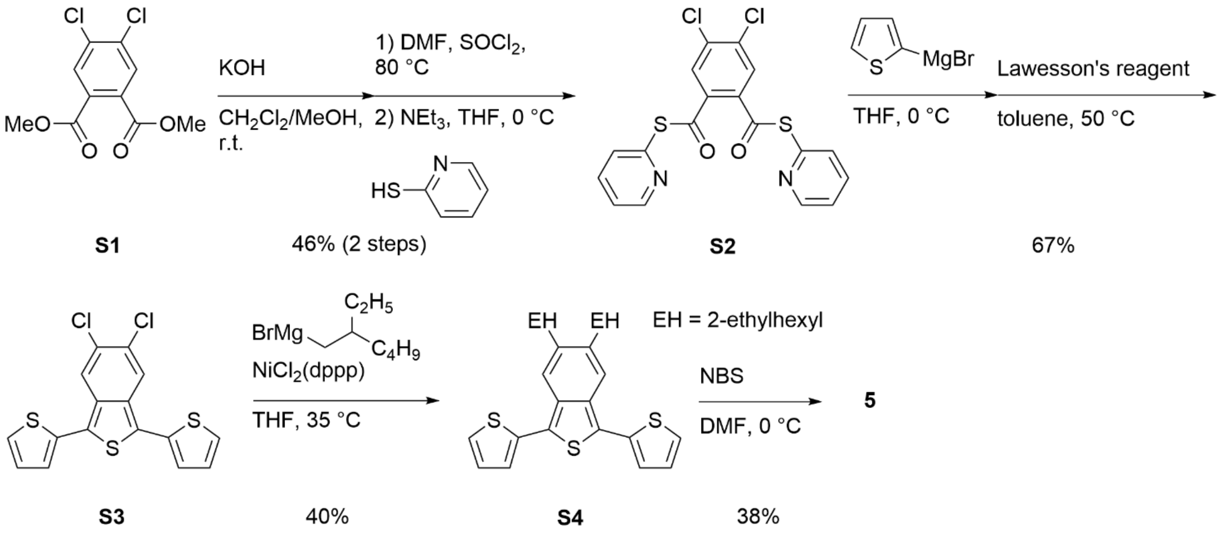

Scheme S1.1. Synthetic route of **5**.

Synthesis of S2: Compound **S2** was synthesized from **S1** with a yield of 46% by following the procedure used for the preparation of **2**. Pale yellow solid; ^1H NMR (400 MHz, $CDCl_3$, TMS): δ 7.31-7.35 (m, 2H), 7.73-7.80 (m, 4H), 7.96 (s, 2H), 8.64 (m, 2H). This compound was used for next step without further purification.

Synthesis of S3: Compound **S2** (6.9 g, 16.4 mmol) was placed in a two-necked-bottomed flask and dissolved in THF (112 mL). 2-Thienyl magnesium bromide (32.8 mmol, 0.5 M in THF) was added slowly to the solution at 0 °C. The reaction mixture was stirred for 30 min. and then quenched by addition of 10% HCl aq.. The resultant mixture was extracted with $CHCl_3$, and the combined organic layer was washed with 5% NaOH aq., $NaHCO_3$ aq., and water. After drying over with $MgSO_4$, the solvent was removed under reduced pressure to give **D** as a pale yellow solid. ^1H NMR (400 MHz, $CDCl_3$, TMS): δ 7.11 (dd, J = 5.0, 3.7 Hz, 2H), 7.47 (dd, J = 3.7, 0.9 Hz, 2H), 7.71 (dd, J = 5.0, 0.9 Hz, 2H), 7.82 (s, 2H); ^{13}C NMR (100 MHz, $CDCl_3$, TMS): δ 128.3, 131.0, 135.2, 135.3, 135.8, 138.7, 143.2, 185.7.

Lawesson's reagent (9.4 g, 23.4 mmol) was added to a solution of **D** in toluene (260 mL) and stirred at 50 °C. After stirring for 1 h, the solvent was removed under reduced pressure and purified by column chromatography on silica gel ($CHCl_3$). Then obtained solid was recrystallized from $CHCl_3$/hexane to give **S3** (4.0 g, 67%) as a red solid.

^{1}H NMR (400 MHz, $CDCl_3$, TMS): δ 7.16 (dd, J = 5.0, 3.7 Hz, 2H), 7.32 (dd, J = 3.7, 0.9 Hz, 2H), 7.42 (dd, J = 5.0, 0.9 Hz, 2H), 8.03 (s, 2H); ^{13}C NMR (100 MHz, $CDCl_3$, TMS): δ 122.2, 126.6, 126.7, 127.1, 128.5, 130.3, 133.6, 134.7; HRMS (APCI) *m/z* 366.9232 ($[M+H]^+$) ($[M+H]^+$, Calcd 366.9238).

*Synthesis of **S4***: Compound **S3** (1.13 g, 3.08 mmol) and $NiCl_2$(dppp) (85 mg, 0.157 mmol) were placed in a two-necked-bottomed flask and dissolved in THF (10.8 mL). (2-Ethylhexyl)magnesium bromide (9.38 mmol, 1.0 M in Et_2O) was added slowly to the solution at 0 °C. The reaction mixture was stirred for 1h at 0 °C, 11 h at 35 °C, and then quenched by addition of water. The resultant mixture was extracted with EtOAc, and the combined organic layer was washed with water. After drying over with $MgSO_4$, the solvent was removed under reduced pressure and purified by column chromatography on silica gel (hexane), followed by purification with preparative GPC ($CHCl_3$) to give **S4** (660 mg, 40%) as a red oil. ^{1}H NMR (400 MHz, $CDCl_3$, TMS): δ 0.85-0.93 (m, 12H), 1.22-1.42 (m, 16H), 1.63 (m, 2H), 2.59 (m, 4H), 7.14 (d, J = 5.0, 3.7 Hz, 2H), 7.32 (dd, J = 3.7, 1.4 Hz, 2H), 7.35 (dd, J = 5.0, 1.4 Hz, 2H), 7.66 (s, 2H); ^{13}C NMR (100 MHz, $CDCl_3$, TMS): δ 10.8, 14.2, 23.2, 25.5, 28.8, 32.5, 37.7, 39.7, 121.0, 124.6, 124.9, 127.8, 134.6, 136.2, 138.4; HRMS (APCI) *m/z* 523.2512 ($[M+H]^+$) ($[M+H]^+$, Calcd 523.2521).

*Synthesis of **5***: NBS (224 mg, 1.26 mmol) was added in two portions to a solution of **S4** (660 mg, 1.26 mmol) in DMF (35 mL) at 0 °C. After stirring for 4 h at 0 °C, the reaction was quenched by addition of water. The combined organic was extracted with EtOAc and washed with water. After drying over with $MgSO_4$, the solvent was removed under reduced pressure and purified by column chromatography on silica gel (hexane) to give **5** (290 mg, 38%) as a red oil. ^{1}H NMR (400 MHz, $CDCl_3$, TMS): δ 0.82-0.93 (m, 12H), 1.22-1.42 (m, 16H), 1.62 (m, 2H), 2.59 (m, 4H), 7.04 (d, J = 4,4 Hz, 1H), 7.08 (d, J = 4,4 Hz, 1H), 7.14 (dd, J = 5.0, 3.8 Hz, 1H), 7.32 (dd, J = 3.8, 1.0 Hz, 1H), 7.36 (dd, J = 5.0, 1.0 Hz, 1H), 7.56 (s, 1H), 7.66 (s, 1H); ^{13}C NMR (100 MHz, $CDCl_3$, TMS): δ 10.9, 14.2, 23.2, 25.6, 28.8, 32.5, 37.7, 40.0, 111.4, 120.7, 121.1, 123.3, 125.2, 125.3, 125.4, 127.8, 130.6, 134.5, 134.8, 136.0, 137.8, 138.6, 138.9; HRMS (APCI) *m/z* 601.1626 ($[M+H]^+$) ($[M+H]^+$, Calcd 601.1627).

1.9 References

1 (a) Mishra, A.; Ma, C.-Q.; Bäuerle, P. *Chem. Rev.* **2009**, *109*, 1141. (b) Takimiya, K., Shinamura, S.; Osaka I.; Miyazaki, E. *Adv. Mater*. **2011**, *23*, 4347. (c) Zhao, Y.; Guo Y.; Liu, Y. *Adv. Mater*. **2013**, *25*, 5372. (d) Roncali, J.; Leriche, P.; Blanchard, P. *Adv. Mater.* **2014**, *26*, 3821. (e) McAfee, S. M.; Topple, J. M.; Hill, I. G.; Welch, G. C. *J. Mater. Chem. A* **2015**, *3*, 16393.

2 (a) Yang, J.; Yan, D.; Jones, S. T. *Chem. Rev*. **2015**, *115*, 5570. (b) Ostroverkhova, O. **Chem. Rev**. **2016**, *116*, 13279.

3 Deuchert, K.; Hünig, S. *Angew., Chem., Int. Ed*. **1978**, *17*, 875.

4 (a) Torrance, J. B. *Acc. Chem. Res*. **1979**, *12*, 79. (b) Martín, N.; Segura, J. L.; Seoane, C. *J. Mater. Chem*. **1997**, *7*, 1661.

5 Casado, J.; Ortiz, R. P.; Navarrete, J. T. L. *Chem. Soc. Rev*. **2012**, *41*, 5672.

6 (a) Pappenfus, T. M.; Chesterfield, R. J.; Frisbie, C. D.; Mann, K. R.; Casado, J.; Raff, J. D.; Miller, L. L. *J. Am. Chem. Soc*. **2002**, *124*, 4184. (b) Chesterfield, R. J.; Newman, C. R.; Pappenfus, T. M.; Ewbank, P. C.; Haukaas,

M. H.; Mann, K. R.; Miller, L. L.; Frisbie, C. D. *Adv. Mater*. **2003**, *15*, 1278. (c) Janzen, D. E.; Burand, M. W.; Ewbank, P. C.; Pappenfus, T. M.; Higuchi, H.; da Silva Filho, D. A.; Young, V. G.; Brédas, J.-L.; Mann, K. R. *J. Am. Chem. Soc*. **2004**, *126*, 15295.

7 Handa, S.; Miyazaki, E.; Takimiya, K.; Kunugi, Y. *J. Am. Chem. Soc*. **2007**, *129*, 11684.

8 (a) Ribierre, J. C.; Fujihara, T.; Watanabe, S.; Matsumoto, M.; Muto, T.; Nakao, A.; Aoyama, T. *Adv. Mater*. **2010**, *22*, 1722. (b) Ribierre, J.-C.; Watanabe, S.; Matsumoto, M.; Muto, T.; Nakao, A.; Aoyama, T. *Adv. Mater*. **2010**, *22*, 4044. (c) Ribierre, J.-C.; Watanabe, S.; Matsumoto, M.; Muto, T.; Aoyama, T. *Appl. Phys. Lett*. **2010**, *96*, 083303.

9 Li, J.; Qiao, X.; Xiong, Y.; Hong, W.; Gao, X.; Li, H. *J. Mater. Chem. C*, **2013**, *1*, 5128.

10 (a) Qiao, Y.; Guo, Y.; Yu, C.; Zhang, F.; Xu, W.; Liu, Y.; Zhu, D. *J. Am. Chem. Soc*. **2012**, *134*, 4084. (b) Qiao, Y.; Zhang, J.; Xu, W.; Zhu, D. *J. Mater. Chem*. **2012**, *22*, 5706. (c) Wu, Q.; Ren, S.; Wang, M.; Qiao, X.; Li, H.; Gao, X.; Yang, X.; Zhu, D. *Adv. Mater*. **2013**, *23*, 2277.

11 Xiong, Y.; Tao, J.; Wang, R.; Qiao, X.; Yang, X.; Wang, D.; Wu, H.; Li, H. *Adv. Mater*. **2016**, *28*, 5949.

12 (a) Wu, Q.; Li, R.; Hong, W.; Li, H.; Gao, X.; Zhu, D. *Chem. Mater*. **2011**, *23*, 3138. (b) Wu, Q.; Ren, S.; Wang, M.; Qiao, X.; Li, H.; Gao, X.; Yang, X.; Zhu, D. *Adv. Funct. Mater*. **2013**, *23*, 2277. (c) Li, J.; Qiao, X.; Xiong, Y.; Li, H.; Zhu, D. *Chem. Mater*. **2014**, *26*, 5782–5788.

13 Mori, T.; Yanai, N.; Osaka, I.; Takimiya, K. *Org. Lett*. **2014**, *16*, 1334.

14 (a) Hernández, V.; Losada, S. C.; Casado, J.; Higuchi, H.; Navarrete, J. T. L. *J. Phys. Chem. A* **2000**, *104*, 661. (b) Takahashi, T.; Matsuoka, K.-i.; Takimiya, K.; Otsubo, T.; Aso, Y. *J. Am. Chem. Soc*. **2005**, *127*, 8928. (c) Ortiz, R. P.; Casado, J.; Hernández, V.; Navarrete, J. T. L.; Viruela, P. M.; Ortí, I.; Takimiya, K.; Otsubo, T. *Angew., Chem. Int. Ed*. **2007**, *46*, 9057. (d) Canesi, E. V.; Fazzi, D.; Colella, L.; Bertarelliand, C.; Castiglioni, C. *J. Am. Chem. Soc*. **2012**, *134*, 19070. (e) Kishi, R.; Dennis, M.; Fukuda, K.; Murata, Y.; Morita, K.; Uenaka, H.; Nakano, M. *J. Phys. Chem. C* **2013**, *117*, 21498. (f) Colella, L.; Brambilla, L.; Nardone, V.; Parisini, E.; Castiglioni, C.; Bertarelli, C. *Phys. Chem. Chem. Phys*. **2015**, *17*, 10426. (g) Ray, S.; Sharma, S.; Salzner, U.; Patil, S. *J. Phys. Chem. C* **2017**, *121*, 16088.

15 Wudl, F.; Kobayashi, M.; Heeger, A. J. *J. Org. Chem*. **1984**, *49*, 3382.

16 (a) Zhang, C.; Zang, Y.; Gann, E.; McNeill, C. R.; Zhu, X.; Di, C.-a.; Zhu, D. *J. Am. Chem. Soc*. **2014**, *136*, 16176. (b) Zhang, C.; Zang, Y.; Zhang, F.; Diao, Y.; McNeill, C. R.; Di, C.-a.; Zhu, X.; Zhu, D. *Adv. Mater*. **2016**, *28*, 8456. (c) Ren, L.; Fan, H.; Huang, D.; Yuan, D.; Di, C.-a.; Zhu, X. *Chem. − Eur. J*. **2016**, *22*, 17136. (d) Ren, L.; Yuan, D.; Gann, E.; Guo, Y.; Thomsen, L.; McNeill, C. R.; Di, C.-a.; Yi, Y.; Zhu, X.; Zhu, D. *Chem. Mater*. **2017**, *29*, 4999. (e) Zhang, C.; Yuan, D.; Wu, H.; Gann, E.; Thomsen, L.; McNeill, C. R.; Di, C.-a.; Zhu, X.; Zhu, D. *J. Mater. Chem. C* **2017**, *5*, 1935.

17 Lorcy, D.; Robinson, k. D.; Okuda, Y.; Atwood, J. L.; Cava, m. P. *J. Chem. Soc., Chem. Commun*. **1993**, 345.

18 Kishi, R.; Ochi, S.; Izumi, S.; Makino, A.; Nagami, T.; Fujiyoshi, J.-y.; Matsushita, N.; Saito, M.; Nakano, M. *Chem. − Eur. J*. **2016**, *22*, 1493.

19 Kiebooms, R. H. L.; Adriaensens, P. J. A.; Vanderzande, D. J. M.; Gelan, J. M. J. V. *J. Org. Chem*. **1997**, *62*, 1473.

20 Higuchi, H.; Yoshida, S.; Uraki, Y.; Ojima, J. *Bull. Chem. Soc. Jpn*. **1998**, *71*, 222.

21 Metrangolo, P.; Neukirch, H.; Pilati, T.; Resnati, G. *Acc. Chem. Res*. **2005**, *38*, 386.

22 Bard, A. J.; Faulkner, L. R. Electrochemical MethodsFundamentals and Applications, Wiley, New York, **1984**.

23 Pommerehne, J.; Vestweber, H.; Guss, W.; Mahrt, R. F.; Bassler, H.; Porsch, M.; Daub, J. *Adv. Mater*. **1995**, *7*, 551.

24 Cardona, C. M.; Li, W.; Kaifer, A. E.; Stockdale, D.; Bazan, G. C. *Adv. Mater.* **2011**, *23*, 2367.

25 Asadi, K.; Gholamrezaie, F.; Smits, E. C. P.; Blom, P. W. M.; de Boer, B. *J. Mater. Chem*. **2007**, *17*, 1947.

26 Pivrikas, A.; Ullah, M.; Sitterand, H.; Sariciftci, N. S. *Appl. Phys. Lett*. **2011**, *98*, 092114.

27 Li, D.; Qu, H.; Zhou, L.; Kanno, K.-i.: Guo, Q.; Shen, B.; Takahashi, T. *Org. Lett*. **2009**, *11*, 3318.

28 Sakamoto, Y.; Komatsu, S.; Suzuki, T. *J. Am. Chem. Soc*. **2001**, *123*, 4643.

Chapter 2

Development of Quinoidal Oligothiophenes Having Full Benzo-Annulation

2.1 Introduction

As discussed in chapter 1, quinoidal oligothiophenes have a resonance between a closed-shell quinoidal state and an open-shell biradical state as well as a low-lying triplet energy level.[1] Such quinoidal oligothiophenes with Kekulé diradical characteristics would be expected to be ideal candidates for nonlinear optics and singlet-fission photovoltaics applications.[2] On the other hand, it has also been reported that low-lying triplet states result in a high charge-recombination efficiency in organic solar cells (OSCs).[3] In fact, the use of quinoidal π-conjugated scaffolds as OSC materials is still rare.[4] Given this situation, the management and control of biradical characteristics to fine-tune the electronic properties of quinoidal oligothiophenes becomes an important issue. In this context, stabilizing quinoidal resonance by using aromatic stabilization represents an effective approach.[5] In chapter 1, a quinoidal terthiophene bearing a benzo[*c*]thiophene unit to introduce benzo-annulation (**BTQ**) was developed.[6] The quinoidal structure in this molecule resulted in an increased contribution of the quinoidal state compared to **TQ**, leading to improved OFET characteristics. This result motivated us to develop additional fully benzo-annulated quinoidal oligothiophene derivatives in order to realize a complete closed-shell. However, functionalization of benzo[*c*]thiophene-repeating terthiophene has not been achieved because of their instability. In this work, we report on successfully overcoming this problem by utilizing a thermal retro Diels–Alder reaction and the development of new quinoidal terthiophenes that contain full benzo-annulation (**B3TQ**) (Figure 2.1).

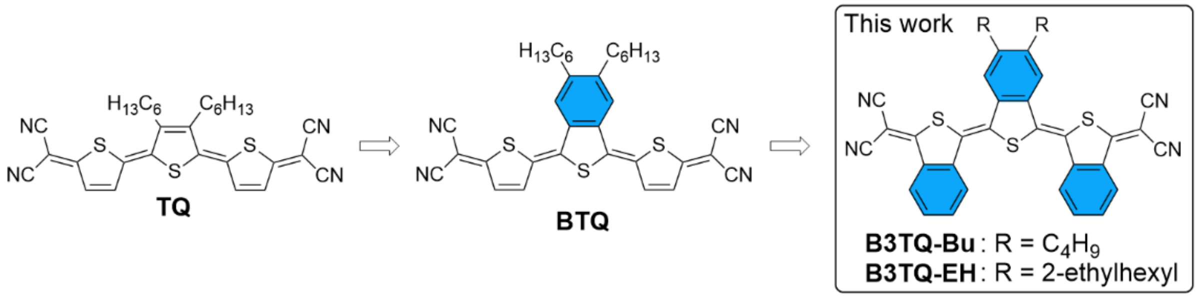

Figure 2.1. Chemical structures used in this study.

2.2 Theoretical study

To estimate the biradical character (y), the occupation number of the LUNO of the model compounds **TQ-H**, **BTQ-H**, and **B3TQ-H** were calculated by using the spin-unrestricted Hartree–Fock method at the UHF/6-31G(d) level.[7] As shown in Figure 2.2, the y value of these compounds decreased with increasing amount of benzo-annulation, and the fully-annulated **B3TQ-H** showed a y value of 0.00. This result indicates that the open-shell electronic configuration makes no contribution in the ground state. The symmetries for the HOMO and LUMO for the terthiophene backbone of **B3TQ-H** were similar to those of **TQ-H** and **BTQ-H**. However, the HOMO–LUMO energy gap of **B3TQ-H** was increased compared to the values for **TQ-H** and **BTQ-H**, which is a unique behavior of closed-shell molecules and diradicaloids having electron-correlated systems.[8] This theoretical result indicates that the introduction of benzo-annulation into quinoidal backbones can substantially change both the LUMO energy levels and the HOMO-LUMO energy gaps. This is in contrast to the case of methyl-substituted quinoidal terthiophene, where the HOMO-LUMO energy gap has little influence on the number of methyl groups due to the similar biradical character of this derivative (Figure S2.1 in the experimental section). The energies of the singlet (E_S) and triplet (E_T) excited states for these compounds were also calculated. As summarized in Table S2.1, compared to the E_S, the E_T values were significantly increased with decreasing y values. The resulting low value of E_S–2E_T for **B3TQ-H** indicates the potential for singlet fission applications.

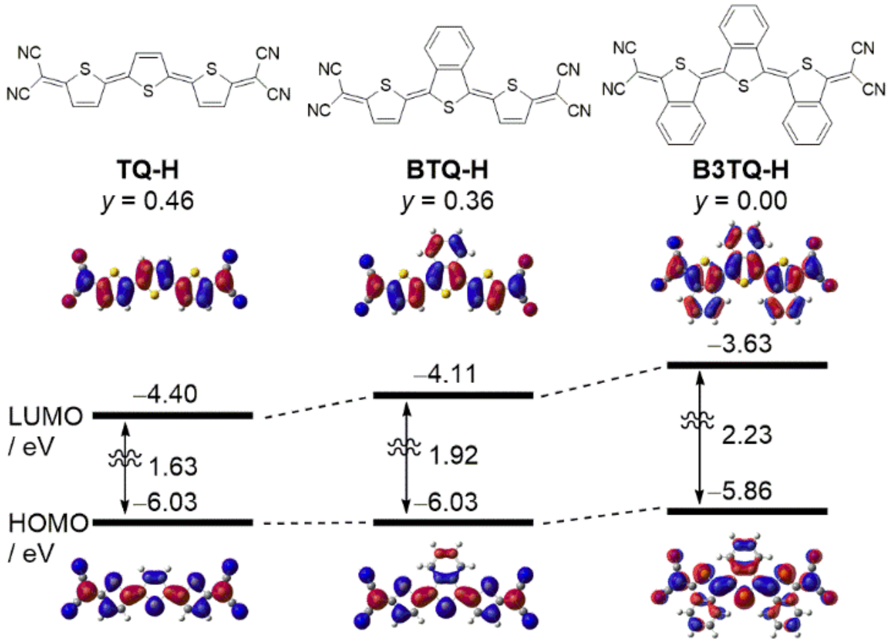

Figure 2.2. Calculated energy levels, HOMOs, LUMOs, and *y* values of **TQ-H**, **BTQ-H**, and **B3TQ-H**.

2.3 Synthesis, Thermal Properties, and X-Ray Single-Crystal Structure

The synthesis of **B3TQ-Bu** and **B3TQ-EH** is shown in Scheme 2.1. To circumvent the formation of unstable benzo[*c*]thiophene-repeated terthiophene framework, a thermal retro Diels–Alder reaction was used in the final step of the synthesis.[9] the 2-pyridinyl ester **1a** was reacted with the Grignard reagent **2**, which was prepared by the reaction of 1-iodo-4,7-dihydro-4,7-ethanobenzo[*c*]thiophene and isopropylmagnesium chloride, to afford **3a**. Treatment of **3a** with Davy's reagent gave the terthiophene with a benzo[*c*]thiophene in the central unit, which was subjected to iodination using *N*-iodosuccinimide (NIS) to provide **4a**. The Pd-catalyzed coupling reaction of **4a** with sodium dicyanomethanide, followed by oxidation using DDQ then gave **5a**. Finally, the retro Diels–Alder reaction of **5a** was conducted at 220 °C under reduced pressure to produce **B3TQ-Bu** in 87% yield. The same protocol was used in the synthesis of **B3TQ-EH**. Detailed information concerning the synthesis and characterization of the compounds are summarized in the experimental section.

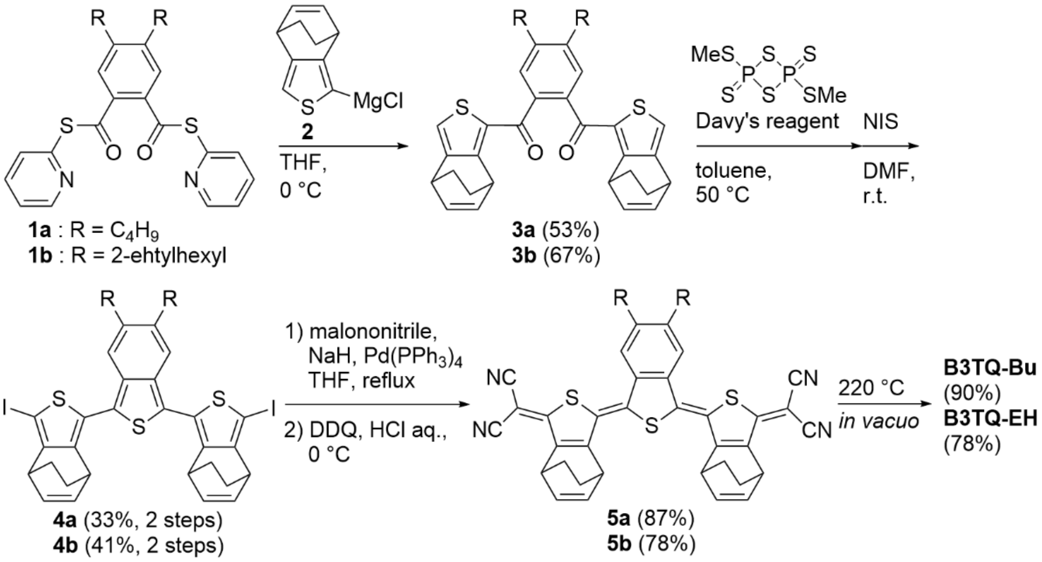

Scheme 2.1. Synthesis of **B3TQ-Bu** and **B3TQ-EH**.

In order to investigate the thermal properties of these derivatives, thermogravimetric analyses (TGA) and differential scanning calorimetry (DSC) measurements under a nitrogen atmosphere were performed (Figure 2.3, S2.2). The TGA curves of **B3TQ-Bu** and **B3TQ-EH** showed a 3% weight-loss temperature (T_d) of 364 and 344 °C, respectively. These T_d values are higher than those of **BTQ** (300 °C) and **TQ** (328 °C), suggesting that the fully benzo-annulation contributed to increasing the thermal stabilities of the derivatives. TGA curve for **5a** showed a weight loss of 8.1% between 147 and 206 °C, which is attributed to the elimination of two ethylene molecules. A similar weight loss was observed for **5b** (Figure 2.3(b)). As shown in Figure S2.2, the DSC curves for **BTQ** and **TQ** showed melting peaks at 277 and 235 °C, followed by exothermic peaks at around 290 and 240 °C on the first scans, respectively. These exothermic peaks are assigned to decomposition products since insoluble charcoal solids were obtained after the first scan. On the other hand, the DSC curves for **B3TQ-EH** exhibited melting and crystallization peaks in the second scan, and **B3TQ-Bu** showed polymorphism, which was confirmed by temperature-dependent X-ray diffraction measurements (Figure S2.3).

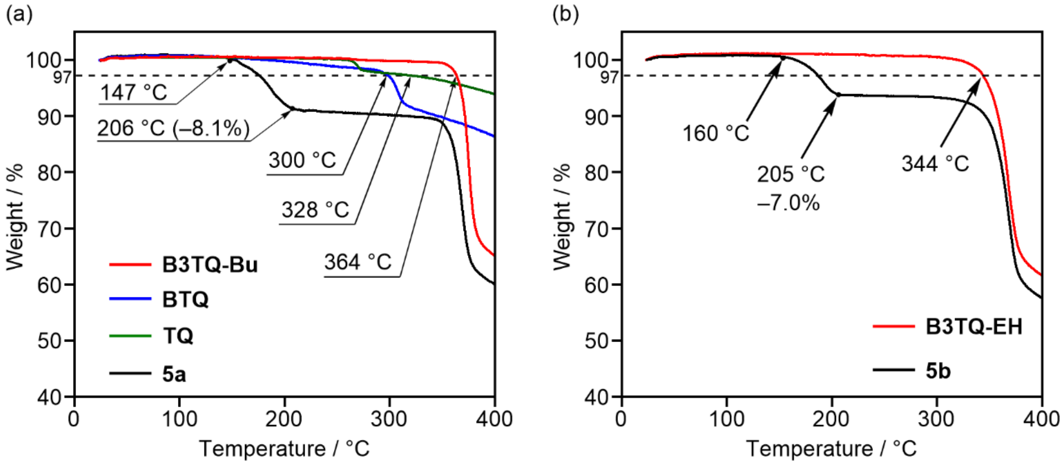

Figure 2.3. TGA curves for (a) **B3TQ-Bu**, **BTQ**, **TQ**, and **5a**, and (b) **B3TQ-EH** and **5b** with a heating rate of 10 °C min^{-1} in a N_2 atmosphere.

The molecular structure of **B3TQ-Bu** was unambiguously elucidated by X-ray diffraction analysis of crystals that were grown by slow evaporation from a $CHCl_3$/EtOAc solution. As shown in Figure 2.4(a), the π-conjugated framework of **B3TQ-Bu** has a perfectly planar geometry with dihedral angles of 0.0°. In the packing diagram, **B3TQ-Bu** molecules are arranged in a co-facial stacking arrangement with an intermolecular π–π distance of 3.48 Å (Figure 2.4(b)). Based on this diagram, the calculated transfer integrals of the HOMO and LUMO between the stacked molecules were determined to be 56.1 and 85.7 meV, respectively, by using the ADF program at the PW91/TZP level. To investigate the carrier transporting behaviors of the materials, we attempted to fabricate OFETs based on **B3TQ-Bu** and **B3TQ-EH**. Although the low solubility of **B3TQ-Bu** hampered the device fabrication by solution process, thin film of **B3TQ-EH** was prepared onto HMDS-modified Si/SiO_2 substrate by spin-coating from the $CHCl_3$ solution. This device showed n-type characteristics with the electron mobility of 4.0×10^{-4} $cm^2 V^{-1} s^{-1}$ after thermal annealing at 200 °C (Figure S2.4). In order to compare the bond length alternation (BLA) of the quinoidal backbones for **B3TQ-Bu** and the **TQ-Bu**[10], the harmonic oscillator model of aromaticity (HOMA) analysis was performed.[11] As shown in Figure 2.4(c), **B3TQ-Bu** showed a small HOMA value of 0.36 compared to that of **TQ-Bu** (0.73), indicating that **B3TQ-Bu** has a large degree of BLA. This significant difference clearly highlighted the large contribution of the closed-shell electronic configuration for **B3TQ-Bu**.

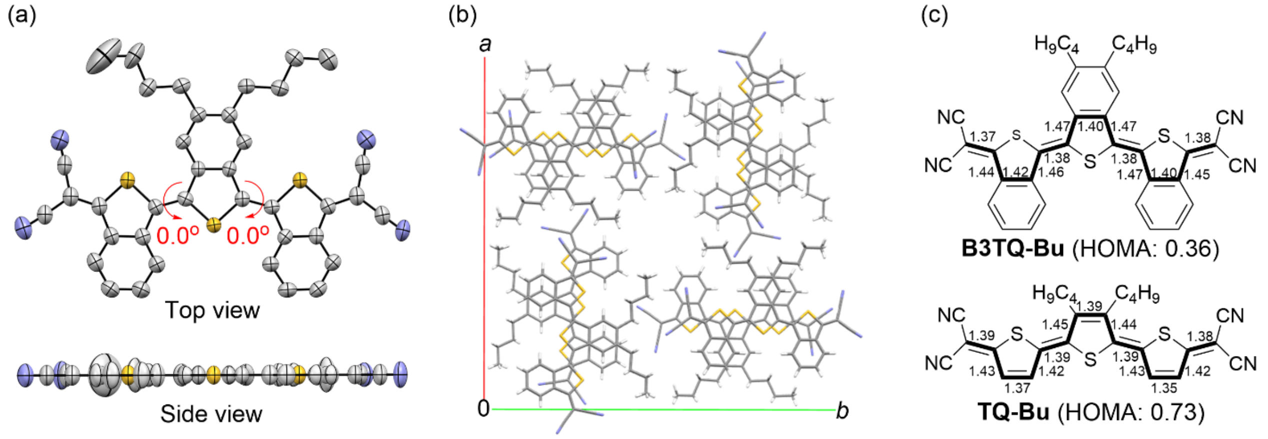

Figure 2.4. (a) ORTEP drawing of **B3TQ-Bu** at the 50% probability level, (b) packing diagram from top view, and (c) bond lengths and the HOMA values for **B3TQ-Bu** and **TQ-Bu**.

2.4 Photophysical and Electrochemical Properties

The UV-vis absorption spectra of **B3TQ-EH** as well as reference compounds **BTQ** and **TQ** in CH_2Cl_2 solutions and thin films are shown in Figure 2.5, and their absorption maxima (λ_{max}) and molar extinction coefficient (ε) values are summarized in Table 2.1. The UV-vis absorption spectrum of **B3TQ-Bu** is shown in Figure S2.5, since the low solubility of **B3TQ-Bu** did not permit the accurate determination of ε. Both **B3TQ-Bu** and **B3TQ-EH** exhibited intense absorption bands in the range of 500–700 nm, which mainly are attributed to a HOMO–LUMO transition, as confirmed by TD-DFT calculations at the CAM-B3LYP/6-31G(d,p) level of theory (see the experimental section). The λ_{max} of these molecules are blue-shifted with increasing level of benzo-annulation. Based on the onset of solution spectra, the optical HOMO–LUMO energy gaps (ΔE_g^{opt}) of **B3TQ-EH**, **BTQ**, and **TQ** were estimated to be 1.83, 1.70, and 1.60 eV, respectively. These phenomena are rationalized by the difference in the open-shell electronic configuration. Compared to the solution spectra, thin films of these molecules showed a red-shifted absorption. However, the broadening of the spectra was suppressed with increasing level of benzo-annulation: the full width at half maximum of **B3TQ-EH**, **BTQ**, and **TQ** was determined to be 158, 203, 320 nm, respectively. This difference may originate from a contribution of intermolecular spin-spin interaction in the case of open-shell molecules.[12] As a result, the estimated optical band gap of **B3TQ-EH** is considerably wider than those of **BTQ** and **TQ** in the solid states (Table 2.1).

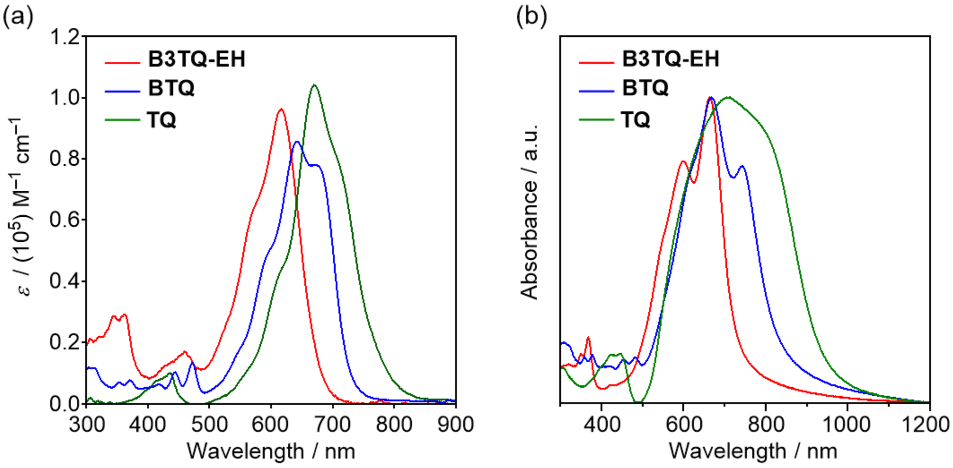

Figure 2.5. UV-vis absorption spectra of **B3TQ-EH**, **BTQ**, **TQ** in (a) CH_2Cl_2 and (b) thin films.

To investigate the electrochemical behavior of these molecules, CV measurements of **B3TQ-EH**, **BTQ**, and **TQ** were carried out in a CH_2Cl_2 solution containing 0.1 M $TBAPF_6$ as a supporting electrolyte. The half-wave reduction and oxidation potentials ($E^{red}_{1/2}$ and $E^{ox}_{1/2}$) were calibrated against a ferrocene/ferrocenium (Fc/Fc^+) couple as the standard, and these values are listed in Table 2.1. As shown in Figure 2.6, the CVs for these molecules showed one reversible oxidation wave corresponding to a one-electron process and one reversible reduction wave corresponding to two-electron processes, which is typically observed for quinoidal oligothiophene derivatives.[6,13] These molecules showed comparable oxidation potentials ($E^{ox}_{1/2}$) of 0.8 eV. However, the $E^{red}_{1/2}$ for these molecules was negatively shifted with increasing level of benzo-annulation. The LUMO energy levels of **B3TQ-EH**, **BTQ**, and **TQ**, as estimated from the equation $E_{LUMO} = -(E^{red}_{1/2} + 4.8)$ were found to be –3.78, –4.06, and –4.23 eV, respectively. This result indicates that the introduction of benzo-annulation to quinoidal terthiophenes leads to an increase in the LUMO energy level. The electrochemically estimated HOMO-LUMO gap (ΔE_g^{CV}) for **B3TQ-EH**, **BTQ**, and **TQ** are summarized in the Table 2.1. These experimentally estimated energy levels of **B3TQ-EH**, **BTQ**, and **TQ** are in good agreement with the theoretical results.

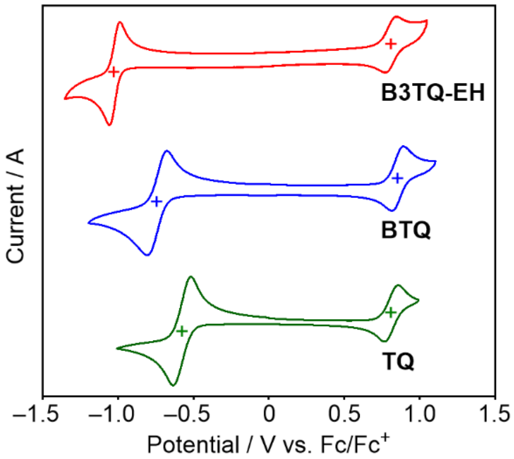

Figure 2.6. CVs of **B3TQ-EH**, **BTQ**, **TQ** in CH_2Cl_2 containing 0.1 M $TBAPF_6$.

Table 2.1. Photophysical and electrochemical properties.

Compounds	λ_{max} (ε × 10^5) /nm (M^{-1} cm^{-1}) [a]	$\Delta E_g^{opt(sol.)}$ /eV [b]	$\Delta E_g^{opt(film)}$ /eV [b]	$E^{ox}_{1/2}$ /V [c]	$E^{red}_{1/2}$ /V [c]	E_{HOMO} /eV [d]	E_{LUMO} /eV [e]	ΔE_g^{CV} /eV
B3TQ-EH	617 (1.0)	1.83	1.69	0.81	−1.02	−5.61	−3.78	1.83
B3TQ-Bu	616 (nd)	1.83	nd	nd	nd	nd	nd	nd
BTQ	642 (0.9)	1.70	1.47	0.86	−0.74	−5.66	−4.06	1.60
TQ	670 (1.1)	1.60	1.31	0.81	−0.58	−5.61	−4.23	1.38

[a] In CH_2Cl_2. [b] Determined by the onset of the UV−vis spectra. [c] In CH_2Cl_2 containing $TBAPF_6$. [d] $E_{HOMO} = -E^{ox}_{1/2} - 4.8$. [e] $E_{LUMO} = -E^{red}_{1/2} - 4.8$.

2.5 Photovoltaic Characteristics

Finally, to reveal the potential of **B3TQ-EH** as a non-fullerene acceptor, we fabricated OSC devices with an inverted structure of indium tin oxide (ITO)/ZnO/**PBDB-T**:**B3TQ-EH**/MoO_3/Ag, where **PBDB-T** (structure shown in Figure S2.6) was used as the donor material.[14] This device showed photovoltaic characteristics with a power conversion efficiency (PCE) of 1.39%, a short-circuit current density of 5.10 mA cm^{-1}, an open-circuit voltage of 0.76 V, and a fill factor of 37% (Figure 2.7(a)). The reproducibility of the data are summarized in Figure S2.7 and Table S2.2. An external quantum efficiency (EQE) spectrum showed photoresponses between 300 and 750 nm (Figure 2.7(b)), which matched with the absorption spectrum of the blend film (Figure S2.6). AFM images of the **PBDB-T**:**B3TQ-EH** films showed smooth morphologies with an average roughness of 0.6 nm (Figure S2.8). Note that **BTQ** and **TQ** showed low PCEs of less than 0.1%. These results indicate that quinoidal oligothiophenes with appropriate electronic properties can function as non-fullerene acceptors.

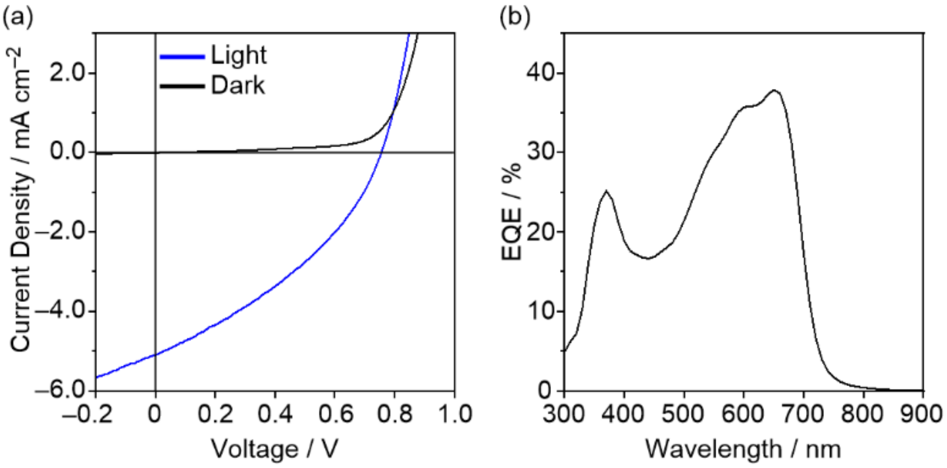

Figure 2.7. (a) Current density-voltage curves and (b) EQE spectrum of **PBDB-T/B3TQ-EH**-based OSCs.

2.6 Conclusion

In conclusion, in order to completely suppress biradical character, quinoidal terthiophenes composed of benzo[*c*]thiophene units were successfully synthesized and their chemical structure determined by X-ray analyses. The introduction of full benzo-annulation had a significant influence on the thermal, photophysical, and electrochemical properties of the compounds. OSC devices based on **PBDB-T** and **B3TQ-EH** showed a PCE of 1.39%. To our knowledge, this is the first reported quinoidal oligothiophene that has the potential for functioning as a non-fullerene acceptor in OSCs. The findings reported herein demonstrate that the electronic structures of quinoidal oligothiophenes can be modulated by appropriate chemical modification, which can broaden electronic applications in the future.

2.7 Experimental Section

Supplementary Figures and Tables

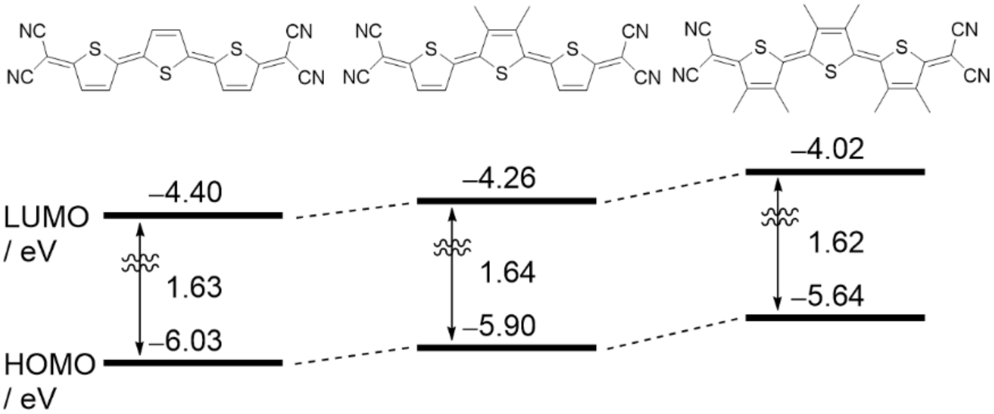

Figure S2.1. Calculated energy levels of the methyl-substituted quinoidal terthiophenes.

Table S2.1. Calculated biradical characteristics and energies.

Compounds	y	E_S /eV	E_T /eV	E_S–2E_T /eV
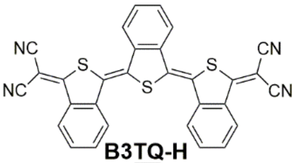 **B3TQ-H**	0.00	2.13	0.90	+0.33
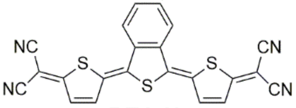 **BTQ-H**	0.36	2.04	0.67	+0.70
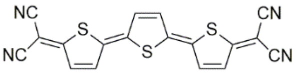 **TQ-H**	0.46	1.94	0.32	+1.30

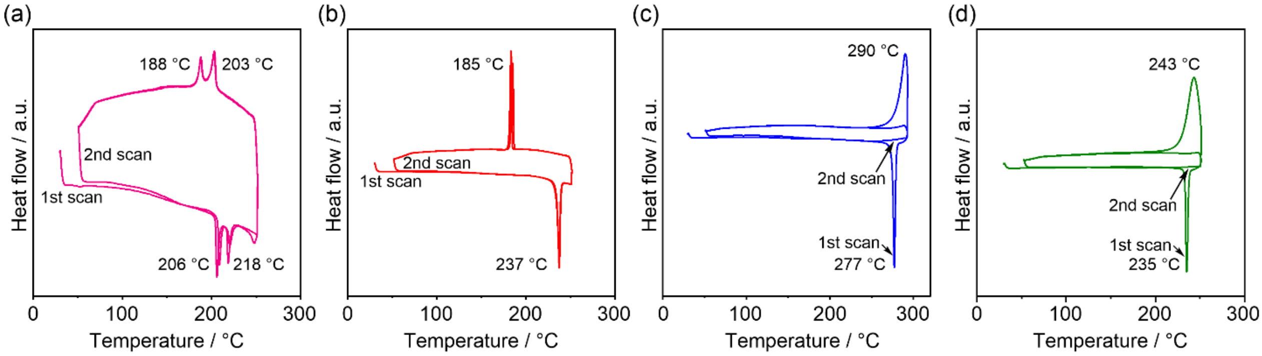

Figure S2.2. DSC curves of (a) **B3TQ-Bu**, (b) **B3TQ-EH**, (c) **BTQ**, and (d) **TQ** at a heating rate of 10 °C min^{-1} in a N_2 atmosphere.

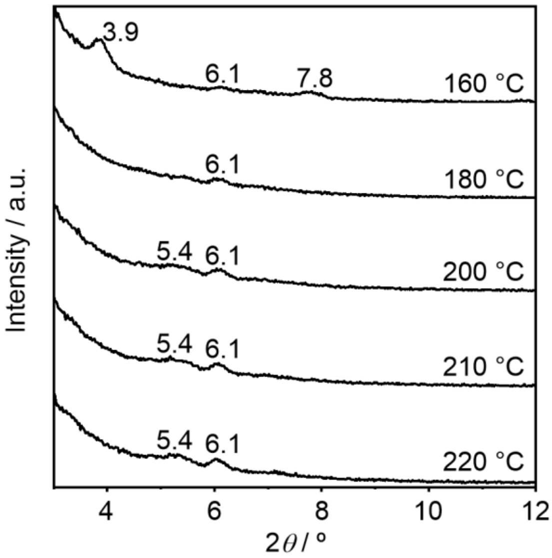

Figure S2.3. Temperature-dependent X-ray diffraction data of **B3TQ-Bu**. Thin films were fabricated by vacuum deposition onto Si/SiO_2 substrates.

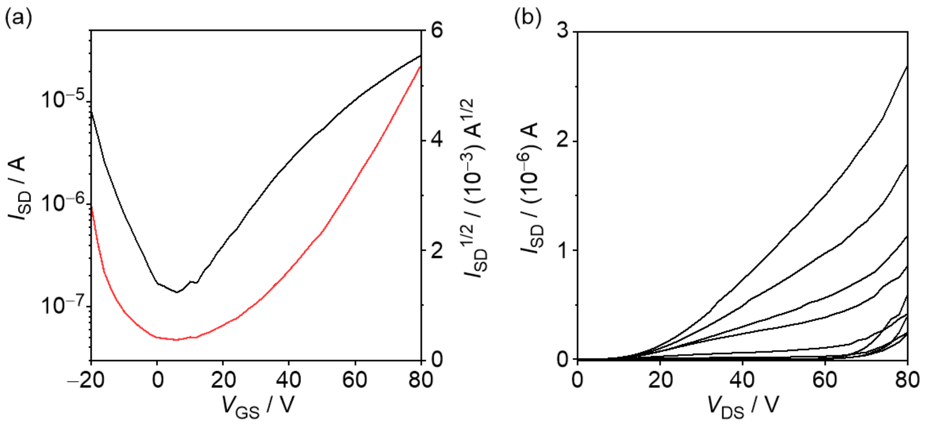

Figure S2.4. (a) Transfer and (b) output characteristics of OFETs using **B3TQ-EH**. V_{GS}, I_{SD}, and V_{DS} denotes gate voltage, source–drain current, and source–drain voltage, respectively.

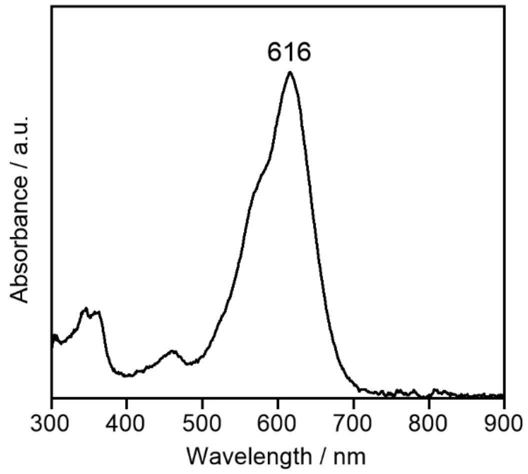

Figure S2.5. UV-vis absorption spectrum of **B3TQ-Bu** in CH_2Cl_2.

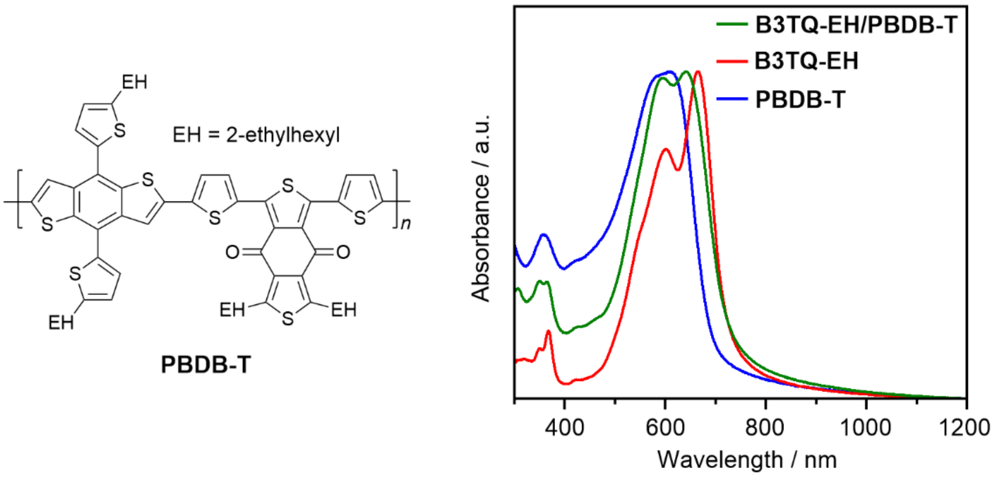

Figure S2.6. Chemical structure of **PBDB-T** and UV-vis absorption spectra of **PBDB-T**:**B3TQ-EH** (green), **B3TQ-EH** (red), and **PBDB-T** (blue) films.

Table S2.2. Photovoltaic characteristics of **PBDB-T**:**B3TQ-EH** based OSCs.

Run	J_{SC} / mA cm^{-2}	V_{OC} / mA cm^{-2}	FF / %	PCE /%
1	5.10	0.76	36	1.39
2	5.00	0.75	36	1.36
3	4.52	0.75	37	1.26
4	4.56	0.75	37	1.25
5	4.35	0.73	37	1.17
6	4.37	0.73	37	1.19
7	4.38	0.74	37	1.19
8	4.44	0.74	37	1.20
Average	4.59 ± 0.28	0.74 ± 0.01	37 ± 0.4	1.25 ± 0.08

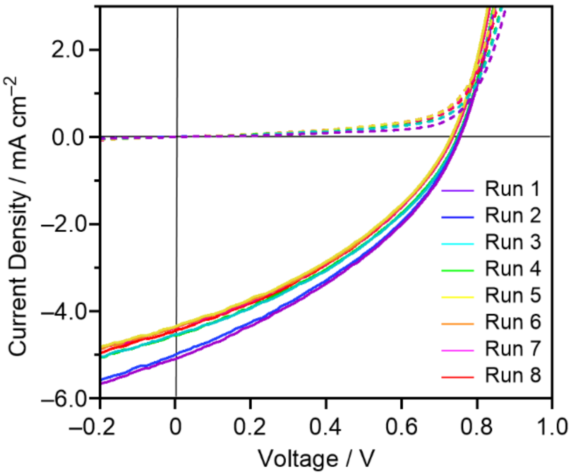

Figure S2.7. Current density-voltage curves **PBDB-T**:**B3TQ-EH** based OSCs.

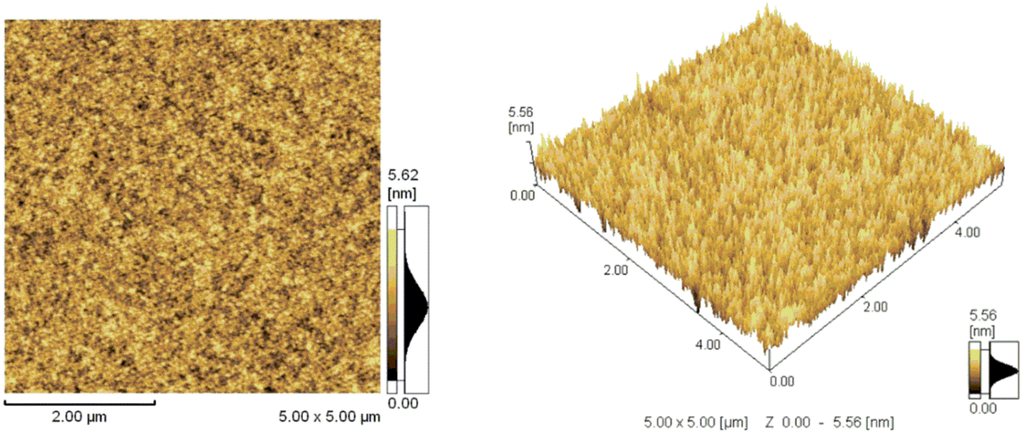

Figure S2.8. AFM height images of **PBDB-T**:**B3TQ-EH** blend films.

General Information

Column chromatography was performed on silica gel. KANTO Chemical silica gel 60N (40–50 μm). Thin-layer Chromatography (TLC) plates were visualized with UV light. Preparative GPC was performed on a Japan Analytical LC-918 equipped with JAI-GEL 1H/2H. ^{1}H and ^{13}C NMR spectra were recorded on a JEOL JNM-ECS400 or JEOL JNM-ECA600 spectrometer in $CDCl_3$ with TMS as an internal standard. Data are reported as follows: chemical shift in ppm (δ), multiplicity (s = singlet, d = doublet, t = triplet, m = multiplet, br = broad), coupling constant (Hz), and integration. UV-vis spectra were recorded on a Shimadzu UV-3600 spectrophotometer. All spectra were obtained in spectrograde solvents. Cyclic voltammetry was carried out on a BAS CV-620C voltammetric analyzer using a platinum disk as the working electrode, platinum wire as the counter electrode, and Ag/AgNO3 as the reference electrode at a scan rate of 100 mV s^{-1}. High-resolution mass spectrum (HRMS) was obtained atmospheric pressure chemical ionization (APCI) or electrospray ionization (ESI) methods using a Thermo scientific LTQ Orbitrap XL. Elemental analyses were performed on PerkinElmer LS-50B by the elemental analysis section of the Comprehensive Analysis Center (CAC) of ISIR, Osaka University. The surface structures of the deposited organic film were observed by atomic force microscopy (Shimadzu, SPM9600), and the film crystallinity was evaluated by an X-ray diffractometer (Rigaku, SmartLab). X-ray diffraction patterns were obtained using Bragg-Brentano geometry with CuKα radiation as an X-ray source with an acceleration voltage of 45 kV and a beam current of 200 mA. The scanning mode was set to 2θ–ω scans between 2º–12º with scanning steps of 0.02º.

X-ray Information

Single crystals suitable of **B3TQ-Bu** were obtained by the recrystallization using $CHCl_3$/EtOAc. The diffraction data were collected on Rigaku Oxford Diffraction XtaLAB PRO diffractometer with CuKα radiation (λ = 1.54187 Å). The structure was solved using a dual-space algorithm (SHELXT version 2018/2[17]) and refined using full-matrix least-squares method (SHELXL version 2018/3[18]). All non-hydrogen atoms were refined anisotropically, whereas all hydrogen atoms were grown using the proper HFIX commands and refined isotropically by using the riding model. CCDC-1967373 contains the supplementary crystallographic data for **B3TQ-Bu**. These data can be obtained free of charge from The Cambridge Crystallographic Data Centre via www.ccdc.cam.ac.uk/data_request/cif/.

OPV Device Fabrication and Evaluation

Organic solar cells were prepared with a structure of ITO/ZnO/**PBDB-T**:**B3TQ-EH**/MoO_3/Ag. ITO-coated glass substrates were first cleaned by ultrasonication in acetone, water, and 2-propanol for 10 min, respectively. The substrates were then activated by ozone treatment for 1 h. ZnO layer was spin-coated using the solution of zinc acetate dihydrate (99.9%, 200 mg), ethanolamine (99%, 55 μL), and 2-methoxyethanol (99.8, 2 mL) at 3000 rpm. and baked at 200 °C for 30 min in air. Subsequently, **PBDB-T**:**B3TQ-EH** (1:1, wt:wt) in a 4 mg mL^{-1} chloroform solution was spin-coated at 600 rpm. for 60 s to obtain a thickness of ca. 60 nm films. MoO_3 and Ag electrodes were evaporated on the top of active layer through a shadow mask to define the active area of the device (0.09 cm^2) under a vacuum of 10^{-5} Pa to thicknesses of 10, 100 nm, respectively. After sealing the device from the air, the photovoltaic characteristics were measured under simulated AM 1.5G solar irradiation (100 mW cm^{-1}) (SAN-EI ELECTRIC Co., LTD., XES-301S). The current density–voltage characteristics of devices were measured by using a KEITHLEY

2400 source meter. The EQE spectrum was measured by using a SOMA OPTICS, LTD. S-9240. The thickness of the active layer was determined by using a KLA Tencor Alpha-step IQ.

Computational Details

All calculations were conducted using Gaussian 09 program. The geometry was optimized with the unrestricted Becke Hybrid (UB3LYP) at 6-31G(d,p) level. The time-dependent density functional theory (TD-DFT) calculation was conducted at the CAM-B3LYP/6-31G(d,p) level of theory.

TD-DFT Calculation

B3TQ-H

Excited State 1: Singlet-A 2.51 eV 495 nm f = 1.50 <S**2>=0.000
HOMO–1 > LUMO+1 0.12572
HOMO > LUMO 0.69053

BTQ-H

Excited State 1: Singlet-A 2.31 eV 537 nm f = 1.83 <S**2>=0.000
HOMO–1 > LUMO+1 0.11448
HOMO < LUMO 0.69744

TQ-H

Excited State 1: Singlet-A 2.10 eV 592 nm f = 1.98 <S**2>=0.000
HOMO > LUMO 0.70672
HOMO < LUMO 0.12099

Synthesis

Unless stated otherwise, all reagents were purchased from commercial sources and used without purification. Compounds **1a** and 1-iodo-4,7-dihydro-4,7-ethanobenzo[*c*]thiophene, and **S1** were prepared by the reference procedures.[8,19.20]

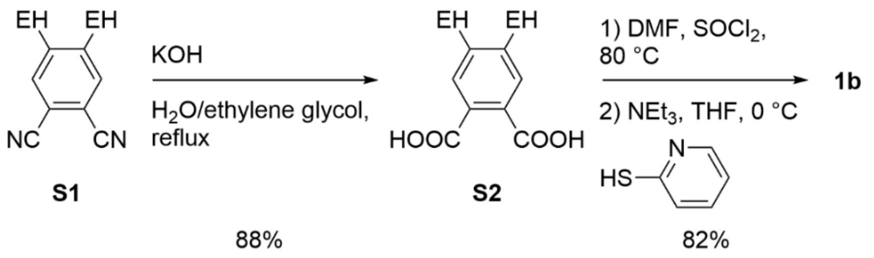

Scheme S2.1. Synthetic route of **1b**.

*Synthesis of **3a***: **1a** (430 mg, 0.927 mmol) was placed in a two-necked-bottomed flask and dissolved in THF (6.5 mL). Grignard reagent **2** (2.04 mmol, 0.33 M in THF), which was prepared by a reaction of 1-iodo-4,7-dihydro-4,7-ethanobenzo[*c*]thiophene and isopropylmagnesium chloride in THF at –10 °C for 1 h, was added slowly to a solution of **1a** at 0 °C. The reaction mixture was stirred for 30 min. and then quenched by addition of 10% HCl aq.. The resultant mixture was extracted with $CHCl_3$, and the combined organic layer was washed with 5% NaOH aq., $NaHCO_3$ aq., and water. After drying over with $MgSO_4$, the solvent was removed under reduced pressure. The residue was purified by column chromatography on silica gel (hexane:EtOAc = 7:1) to give **3a** (278 mg, 53%) as a pale yellow solid. ^{1}H NMR (400 MHz, $CDCl_3$, TMS): δ 0.96 (t, J = 7.3 Hz, 6H), 1.38-1.65 (m, 16H), 2.69 (t, J = 7.8 Hz, 4H), 3.85-3.90 (m, 2H), 4.08-4.14 (m, 2H), 6.34-6.40 (m, 2H), 6.48-6.54 (m, 2H), 6.97-6.99 (m, 2H), 7.44-7.46 (m, 2H). This compound was used for next step without further purification.

*Synthesis of **3b***: **1b** (1.39 g, 2.41 mmol) was placed in a two-necked-bottomed flask and dissolved in THF (16.9 mL). Grignard reagent **2** (5.30 mmol, 0.33 M in THF), which was prepared by a reaction of 1-iodo-4,7-dihydro-4,7-ethanobenzo[*c*]thiophene and isopropylmagnesium chloride in THF at –10 °C for 1 h, was added slowly to a solution of **1b** at 0 °C. The reaction mixture was stirred for 30 min. and then quenched by addition of 10% HCl aq.. The resultant mixture was extracted with $CHCl_3$, and the combined organic layer was washed with 5% NaOH aq., $NaHCO_3$ aq., and water. After drying over with $MgSO_4$, the solvent was removed under reduced pressure. The residue was isolated by column chromatography on silica gel (hexane:EtOAc = 7:1) to give **3b** (1.09 g, 67%) as a pale yellow solid. ^{1}H NMR (400 MHz, $CDCl_3$, TMS): δ 0.82-0.92 (m, 12H), 1.18-1.66 (m, 26H), 2.55-2.68 (m, 4H), 3.85-3.90 (m, 2H), 4.08-4.14 (m, 2H), 6.32-6.40 (m, 2H), 6.45-6.54 (m, 2H), 6.97-6.99 (m, 2H), 7.42-7.44 (m, 2H). This compound was used for next step without further purification.

*Synthesis of **4a***: Davy's reagent (153 mg, 0.539 mmol) was added to a solution of **3a** (278 mg, 0.490 mmol) in toluene (7.0 mL) and stirred at 50 °C. After stirring for 5 min., water was added to the reaction mixture. The precipitate was extracted with EtOAc and washed with brine. After drying over with $MgSO_4$, the solvent was removed under reduced pressure and purified by column chromatography on silica gel (hexane:CH_2Cl_2 = 5:1) to give the intermediate A (158 mg) as an orange solid. NIS (144 mg, 0.586 mmol) was added to a solution of intermediate A (158 mg) in DMF (20 mL) and $CHCl_3$ (5.0 mL) at 0 °C. Then, this reaction was allowed to warm to room temperature. After stirring for 14 h, the reaction was quenched by addition of Na_2SO_3 aq.. The combined organic was extracted with hexane and washed with water. After drying over with $MgSO_4$, the solvent was removed under reduced pressure and purified by column chromatography on silica gel (hexane:CH_2Cl_2 = 10:1), followed by purification with preparative GPC ($CHCl_3$) to give **4a** (133 mg, 33%, 2 steps) as a yellow solid. ^{1}H NMR (400 MHz, $CDCl_3$, TMS): δ 0.97 (t, J = 7.3 Hz, 6H), 1.40-1.65 (m, 16H), 2.64 (t, J = 7.3 Hz, 4H), 3.77-3.82 (m, 2H), 4.10-4.14 (m, 2H), 6.48-6.54 (m, 2H), 6.56-6.62 (m, 2H), 7.45 (s, 2H); ^{13}C NMR (100 MHz, $CDCl_3$, TMS): δ 14.1, 22.9, 25.5, 25.7, 32.8, 33.2, 36.4, 38.1, 63.9, 119.6, 123.5, 127.8, 135.2, 135.4, 135.5, 139.1, 144.7, 152.9; HRMS (APCI) *m/z*: $[M+H]^+$ calcd. for $C_{36}H_{36}I_2S_3$, 819.0141; found, 819.0125.

*Synthesis of **4b***: Davy's reagent (316 mg, 1.11 mmol) was added to a solution of **3b** (684 mg, 1.01 mmol) in toluene

(14.4 mL) and stirred at 50 °C. After stirring for 5 min., water was added to the reaction mixture. The precipitate was extracted with EtOAc and washed with brine. After drying over with $MgSO_4$, the solvent was removed under reduced pressure and purified by column chromatography on silica gel (hexane:CH_2Cl_2 = 5:1) to give the intermediate B (471 mg) as an orange solid. NIS (53 mg, 0.237 mmol) was added to a solution of intermediate B (77 mg) in DMF (8.1 mL) and $CHCl_3$ (2.0 mL) at 0 °C. Then, this reaction was allowed to warm to room temperature. After stirring for 14 h, the reaction was quenched by addition of Na_2SO_3 aq.. The combined organic was extracted with hexane and washed with water. After drying over with $MgSO_4$, the solvent was removed under reduced pressure and purified by column chromatography on silica gel (hexane:CH_2Cl_2 = 10:1), followed by purification with preparative GPC ($CHCl_3$) to give **4b** (63 mg, 41%, 2 steps) as a yellow solid. ^1H NMR (400 MHz, $CDCl_3$, TMS): δ 0.84-0.94 (m, 12H), 1.20-1.68 (m, 26H), 2.52-2.58 (m, 4H), 3.77-3.83 (m, 2H), 4.13-4.18 (m, 2H), 6.48-6.54 (m, 2H), 6.55-6.61 (m, 2H), 7.41 (s, 2H); ^{13}C NMR (100 MHz, $CDCl_3$, TMS): δ 10.9, 11.0, 14.2, 23.2, 25.5, 25.7, 28.8, 32.4, 36.4, 37.9, 38.1, 40.0, 63.8, 120.9, 123.4, 127.9, 135.2, 135.3, 135.5, 138.3, 144.5, 152.9; HRMS (APCI) *m/z*: $[M+H]^+$ calcd. for $C_{44}H_{52}I_2S_3$, 931.1393; found, 931.1371.

Synthesis of ***5a***: Sodium hydride (60% in oil) (35.1 mg, 0.878 mmol) was added to a suspension of malononitrile (29.0 mg, 0.439 mmol) in anhydrous THF (5.2 mL) under nitrogen atmosphere and stirred for 10 min at room temperature. To this mixture was added **4a** (77.0 mg, 0.0941 mmol) and $Pd(PPh_3)_4$ (10.9 mg, 0.00941 mmol), which was then heated to reflux. After 20 h, the reaction was cooled to 0 °C, and diluted hydrochloric acid (1M, 5.3 mL), $CHCl_3$ (5.3 mL) and DDQ (32.0 mg, 0.141 mmol) were added and stirred at 0 °C for 5 min. The resulting mixture was extracted with $CHCl_3$, washed with water, and dried over $MgSO_4$. The solvent was removed under reduced pressure and purified by column chromatography on silica gel (hexane:CH_2Cl_2 = 1:10) to give **5a** (57.0 mg, 87%) as a blue solid. ^1H NMR (400 MHz, $CDCl_3$, TMS): δ 1.01 (t, *J* = 7.3 Hz, 6H), 1.42-1.75 (m, 16H), 2.81 (t, *J* = 7.3 Hz, 4H), 4.88-4.94 (m, 2H), 4.95-5.00 (m, 2H), 6.56-6.67 (m, 4H), 8.01 (s, 2H); ^{13}C NMR (150 MHz, $CDCl_3$, TMS): δ 14.0, 22.5, 24.7, 24.9, 32.5, 32.7, 35.7, 40.2, 62.7, 114.5, 115.1, 125.0, 126.8, 133.0, 135.6, 137.6, 138.7, 145.9, 149.0, 162.3, 163.1; HRMS (APCI) *m/z*: $[M+H]^+$ calcd. for $C_{42}H_{36}N_4S_3$, 693.2175; found, 693.2169.

Synthesis of ***5b***: Compound **5b** was synthesized from **4b** with a yield of 78% by following the procedure used for the preparation of **5a**. blue solid; ^1H NMR (400 MHz, $CDCl_3$, TMS): δ 0.85-0.98 (m, 12H), 1.20-1.80 (m, 26H), 2.65-2.75 (m, 4H), 4.88-4.94 (m, 2H), 4.95-4.50 (m, 2H), 6.56-6.68 (m, 4H), 7.99 (s, 2H); ^{13}C NMR (150 MHz, $CDCl_3$, TMS): δ 10.6, 10.7, 14.1, 23.0, 24.7, 24.9, 25.3, 28.9, 32.6, 35.7, 37.6, 40.3, 63.8, 114.5, 115.0, 125.0, 128.0, 133.1, 135.7, 137.3, 138.7, 145.6, 148.9, 162.3, 163.1; HRMS (APCI) *m/z*: $[M+H]^+$ calcd. for $C_{50}H_{52}N_4S_3$, 805.3427; found, 805.3422.

Synthesis of ***B3TQ-Bu***: **5a** was placed in a Kugelrohr setup, and allowed to heated at 220 °C for 30 min under vacuum condition. After cooling to room temperature, the residue was recrystallized from $CHCl_3$/acetone to give **B3TQ-Bu** (20.0 mg, 90%) as a blue solid; ^1H NMR (400 MHz, $CDCl_3$, TMS): δ 1.04 (t, *J* = 7.3 Hz, 6H), 1.50-1.78 (m, 8H), 2.86 (t, *J* = 6.9 Hz, 4H), 7.65-7.70 (m, 2H), 7.92-7.97 (m, 2H), 8.16 (s, 2H), 8.45 (d, *J* = 8.2 Hz, 2H), 8.83 (d, *J* = 8.2 Hz, 2H). ^{13}C NMR spectrum of this compound was not observed due to the limited solubility. HRMS

(APCI) *m/z*: $[M+H]^+$ calcd. for $C_{38}H_{28}N_4S_3$, 637.1549; found, 637.1548.

*Synthesis of **B3TQ-EH***: **5b** was placed in a Kugelrohr setup, and allowed to heated at 220 °C for 30 min under vacuum condition. After cooling to room temperature, the residue was recrystallized from $CHCl_3$/MeOH to give **B3TQ-EH** (31.0 mg, 78%) as a blue solid; ^1H NMR (400 MHz, $CDCl_3$, TMS): δ 0.87-1.02 (m, 12H), 1.25-1.50 (m, 16H), 1.66-1.76 (m, 2H), 2.69-2.83 (m, 4H), 7.63-7.69 (m, 2H), 7.92-7.97 (m, 2H), 8.12 (s, 2H), 8.44 (d, *J* = 8.2 Hz, 2H), 8.82 (d, *J* = 8.2 Hz, 2H); ^{13}C NMR (150 MHz, $CDCl_3$, TMS): δ 10.7, 14.1, 23.1, 25.4, 28.9, 32.6, 37.6, 40.6, 66.0, 113.9, 114.1, 122.7, 125.8, 126.1, 128.0, 129.2, 134.0, 134.1, 135.6, 136.7, 142.5, 144.7, 170.1; HRMS (APCI) *m/z*: $[M+H]^+$ calcd. for $C_{46}H_{44}N_4S_3$, 749.2801; found, 749.2792; Anal. calcd for $C_{46}H_{44}N_4S_3$: C 73.76; H 5.92; N 7.48, found C 73.62; H 5.95; N 7.35.

*Synthesis of **S2***: Potassium hydroxide (4.90 g, 87.3 mmol) was added to a solution of **S1** (1.23 g, 3.49 mmol) in H_2O (16 mL) and ethylene glycol (32 mL) and refluxed for 2 days. The precipitate was extracted with EtOAc and dried over $MgSO_4$. The solvent was removed under reduced pressure to give **S2** as a white solid (1.20 g, 88%). ^1H NMR (400 MHz, DMSO-d_6, TMS): δ 0.80-0.90 (m, 12H), 1.14-1.34 (m, 12H), 1.47-1.57 (m, 2H), 2.52-2.60 (m, 4H), 7.40 (s, 2H), 12.95 (s, 2H). This compound was used for next step without further purification.

*Synthesis of **1b***: **S2** (1.20 g, 3.07 mmol) was placed in a round-bottom flask. Thionyl chloride (10 mL) and DMF as a catalyst was added to the flask, and the reaction mixture was reflux for overnight. After removal of thionyl chloride and DMF under reduced pressure, the residue was resolved in THF (19 mL). Then, this solution was added to a solution of triethylamine (1.03 mL) and 2-mercaptopyridine (683 mg, 6.14 mmol) in THF (14 mL) at 0 °C. After vigorously stirring for 15 min., the reaction was quenched by addition of 2% HCl aq. (30 mL). The resultant mixture was extracted with $CHCl_3$ and the combined organic layer was washed with 5% sodium hydroxide (NaOH) aq., and water. After drying over with $MgSO_4$, the solvent was removed under reduced pressure. The residue was purified by column chromatography on silica gel (hexane:EtOAc = 7:3) to give **1b** (1.45 g, 82%) as a pale yellow oil. ^1H NMR (400 MHz, $CDCl_3$, TMS): δ 0.84-0.94 (m, 12H), 1.20-1.40 (m, 16H), 1.58-1.64 (m, 2H), 2.56-2.66 (m, 4H), 7.28-7.34 (m, 2H), 7.62 (s, 2H), 7.73-7.83 (m, 4H), 8.62-8.66 (m, 2H); ^{13}C NMR (100 MHz, CDCl3, TMS): δ 10.9, 14.1, 23.0, 25.6, 28.8, 32.4, 37.1, 40.5, 123.6, 130.4, 130.5, 133.9, 137.2, 145.2, 150.3, 151.7, 190.2; HRMS (ESI) *m/z*: $[M+H]^+$ calcd. for $C_{34}H_{44}N_2O_2S_2$, 577.2917; found, 577.2910.

2.8 References

1 Burrezo, P. M.; Zafra, J. L.; Navarrete, J. T. L.; Casado, J. *Angew. Chem., Int. Ed.* **2017**, *56*, 2250–2259.

2 Nakano M. Excitation Energies and Properties of Open-Shell Singlet Molecules; Springer, Heidelberg, **2014**.

3 Ie, Y.; Karakawa, M.; Jinnai, S.; Yoshida, H.; Saeki, A.; Seki, S.; Yamamoto, S.; Ohkita, H.; Aso, Y. *Chem. Commun.* **2014**, *50*, 4123–4125.

4 (a) Kawata, S.; Pu, Y.-J.; Saito, A.; Kurashige, Y.; Beppu, T.; Katagiri, H.; Hada, M.; Kido. J. *Adv. Mater.* **2016**, *28*, 1585−1590. (b) Ren, L.; Fan, H.; Huang, D.; Yuan, D.; Di, C.-a.; Zhu, X. *Chem. − Eur. J.* **2016**, *22*, 17136−17140.

5 Zhang, C.; Zhu, X. *Acc. Chem. Res.* **2017**, *50*, 1342−1350.

6 Yamamoto, K.; Ie, Y.; Nitani, M.; Tohnai, N.; Kakiuchi, F.; Zhang, K.; Pisula, W.; Asadi, K.; Blom, P. W. M.; Aso, Y. *J. Mater. Chem. C* **2018**, *6*, 7493−7500.

7 Kishi, R.; Ochi, S.; Izumi, S.; Makino, A.; Nagami, T.; Fujiyoshi, J.-y.; Matsushita, N.; Saito, M.; Nakano, M. *Chem. − Eur. J.* **2016**, *22*, 1493−1500.

8 Abe, M. *Chem. Rev.* **2013**, *113*, 7011−7088.

9 (a) Shimizu, Y.; Shen, Z.; Ito, S.; Uno, H.; Daub, J.; Ono, N. *Tetrahedron Lett.* **2002**, *43*, 8485−8488. (b) Yamada, H.; Okujima, T.; Ono, N. *Chem. Commun.* **2008**, 2957–2974.

10 Pappenfus, T. M.; Chesterfield, R. J.; Frisbie, C. D.; Mann, K. R.; Casado, J.; Raff, J. D.; Miller. L. L. *J. Am. Chem. Soc.* **2002**, *124*, 4184–4185.

11 Kruszews, J.; Krygowski, T. M. *Tetrahedro*n *Lett.* **1972**, *36*, 3839–3842.

12 Shimizu, A.; Uruichi, M.; Yakushi, K.; Matsuzaki, H.; Okamoto, H.; Nakano, M.; Hirao, Y.; Matsumoto, K.; Kurata, H.; Kubo, T. *Angew., Chem. Int. Ed.* **2009**, *48*, 5482–5486.

13 Pappenfus, T. M.; Raff, J. D.; Hukkanen, E. J.; Burney, J. R.; Casado, J.; Drew, S. M.; Miller, L. L.; Mann, K. R. *J. Org. Chem.* **2002**, *67*, 6015–6024.

14 Qian, D.; Ye, L.; Zhang, M.; Liang, Y.; Li, L.; Huang, Y.; Guo, X.; Zhang, S.; Tan, Z.; Hou, J. *Macromolecules* **2012**, *45*, 9611–9617.

15 Sheldrick, G. M. *Acta Cryst.* **2015**, *A71*, 3-8.

16 Sheldrick, G. M. *Acta Cryst.* **2015**, *C71*, 3-8.

17 Liu, Q.; Feng, Q.-Y.; Yamada, H.; Wang, Z.-S.; Ono, N.; You, X.-Z.; Shen, Z. *Chem. − Asian J.* **2012**, *7*, 1312–1319.

18 Chambrier, I.; White, G.-F.; Cook, M. J. *Chem. − Eur. J.* **2007**, *13*, 7608–7618.

Chapter 3
Effects of Fluorine Substitution in Quinoidal Oligothiophenes for Organic Semiconductors

3.1 Introduction

One of the advantages of organic semiconducting materials is that the structures of such molecules can be easily modified. For example, introduction of electron-withdrawing substituents into π-conjugated backbones in known to a rational approach to create promising n-type organic semiconducting materials. On the other hand, only limited efforts have been made to tune the electronic properties of quinoidal oligothiophene derivatives, based on substituent groups that are attached to the molecule.[1–3] In chapter 1, a benzo-annulated quinoidal terthiophene bearing fluorine atoms at the *β*-positions in the thiophene rings (**BTQ-F**) was developed. This molecule showed increased electron-accepting characteristics, presumably caused by the introduction of electron-withdrawing fluorine atoms (Figure 3.1).[4] The presence of fluorine atoms led to fixed *anti* conformations between adjacent thiophene rings, which were attributed to intramolecular S–F non-covalent interactions.[5] However, since the known fluorinated quinoidal oligothiophenes are limited to **F$_2$CPDT-TCNQ**[2] and **BTQ-F**[4], the effects of fluorine substitution on both electronic and structural properties have not been fully explored. In chapter 3, some new bis(dicyanomethylene)-substituted quinoidal oligothiophene derivatives that contain fluorine atoms at the *β*-positions in the thiophene rings (**FQT**, **FTQ**, and **FTQ-TT**) were synthesized (Figure 3.1), and their molecular properties and OFET characteristics by comparison with the non-fluorinated quinoidal molecules (**QT**, **TQ**, and **TQ-TT**) were investigated. Further studies for blend films of a n-type **FTQ** and p-type pentacene derivative (**TIPSP**) and **TQ/TIPSP** to clarify the effects of the presence of fluorine atoms on the properties and structures of such blends were conducted. Blended films based on combinations of fluorinated π-conjugated molecules with non-fluorinated molecules have been reported to show unique thin-film properties and device performance.[6]

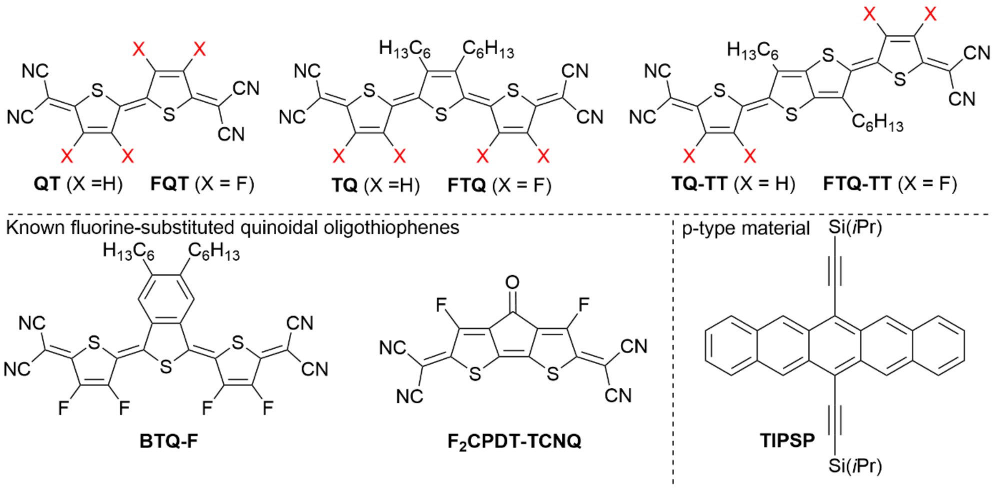

Figure 3.1. Chemical structures of the molecules.

3.2 Theoretical Study

To investigate the effects of electron-withdrawing fluorine atoms on the molecular structure, the HOMO and LUMO energy levels, and the charge distribution, DFT calculations for the target molecules at the B3LYP/6-31G(d, p) level were performed. The hexyl groups in **FTQ**, **FTQ-TT**, **TQ**, and **TQ-TT** were replaced with methyl groups to simplify the calculation (denoted as **FTQ(Me)**, **FTQ-TT(Me)**, **TQ(Me)**, and **TQ-TT(Me)**). As shown in Figure 3.2(a), both fluorinated quinoidal oligothiophenes (**FQT**, **FTQ(Me)**, and **FTQ-TT(Me)**) and non-fluorinated quinoidal oligothiophenes (**QT**, **TQ(Me)**, and **TQ-TT(Me)**) were found to exhibit completely planar conformations. On the other hand, the HOMO and LUMO energy levels of fluorinated quinoidal oligothiophenes were lower than those of non-fluorinated quinoidal oligothiophenes. These results indicate that the introduction of fluorine atoms have a major influence on the electronic properties of quinoidal oligothiophenes. Electro static potential (ESP) plots reflecting the charge distribution in these molecules are shown in Figure 3.2(b). The ESP plots of non-fluorinated quinoidal oligothiophenes revealed the localized distribution of positive charges on the hydrogen atoms at the β-positions of the thiophenes and methyl groups, while negative charges were concentrated on the dicyanomethylene moieties. In contrast, the distribution of negative charge was extended to fluorine atoms in the case of the fluorinated quinoidal oligothiophenes, leading to the positive charges being concentrated on the oligothiophene core. This result indicates that fluorine substitution alters the charge distribution symmetry on the oligothiophene framework of these molecules.

In order to analyze intramolecular S–F interactions, natural bond orbital (NBO) analyses of the fluorinated quinoidal molecules as well as the corresponding fluorinated oligothiophenes were performed using MP2/jun-cc-pVDZ. As shown in Figure S3.1 (see the experimental section), the lone pair of the fluorine atom is located close to the C–S $\sigma*$ antibonding orbital, and the through-space charge transfer stabilization (E_{CT}) was calculated to be between 0.81 and 1.66 kcal mol^{-1}. Interestingly, quinoidal structures have large E_{CT} values compared to the corresponding fluorinated oligothiophenes. This phenomenon can be rationalized by the decreased distance between the sulfur and fluorine atoms in the molecule, due to the double bond character between the thiophene rings in the quinoidal structure.

The singlet biradical character (y) of these quinoidal molecules was also estimated, by calculating the occupation number of the lowest unoccupied natural orbital with spin-unrestricted calculation at the UHF/6-31G(d) level.[7] **FQT**, **FTQ(Me)**, and **FTQ-TT(Me)** gave y values of 0.37, 0.48, and 0.54, which are similar to those of **QT** (0.34), **TQ(Me)** (0.45), and **TQ-TT(Me)** (0.52). This result indicates that the introduction of fluorine atoms into quinoidal oligothiophene derivatives has little effect on the biradical character of such molecules.

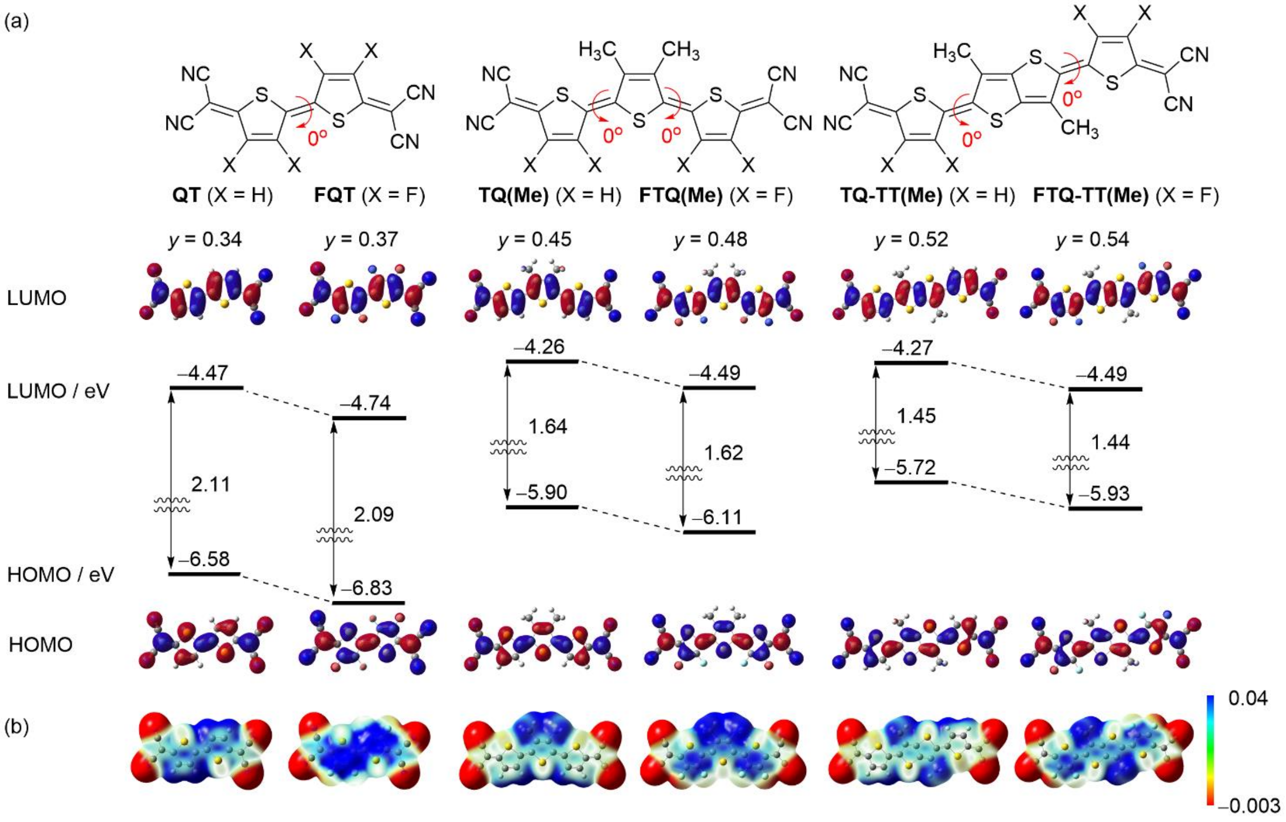

Figure 3.2. (a) Calculated HOMO and LUMO orbitals, energy levels, *y* values and (b) ESP plots for the compounds investigated in this study. Red and blue colors in ESP plots indicate negative and positive charge distribution, respectively.

3.3 Synthesis and Characterization

The synthesis of **FQT**, **FTQ**, and **FTQ-TT** are shown in Scheme 3.1. The key to accessing these compounds is the synthesis of fluorinated oligothiophene frameworks with bromo substituents at both terminal positions. Bromination of 3,3',4,4'-tetrafluoro-5,5'-bis(trimethylsilyl)-2,2'-bithiophene (**1**) with NBS yielded the dibromo bithiophene **2** in 79% yield. A Stille-coupling reaction was employed to prepare **4a** and **4b**, which were then brominated using NBS to afford **5a** and **5b**. Finally, palladium-catalyzed coupling reactions of **2**, **5a**, and **5b** with sodium dicyanomethanide, followed by oxidation with 2,3-dichloro-5,6-dicyano-*p*-benzoquinone (DDQ) to give **FQT**, **FTQ**, and **FTQ-TT** in 56%, 49% and 63% yield, respectively. Synthesis of **TQ-TT** followed previously reported methods (Scheme S3.1).[8] Interestingly, the fluorinated quinoidal oligothiophenes (**FQT**: 5.5 mg mL^{-1}, **FTQ**: 48.8 mg mL^{-1}, **FTQ-TT**: 14.7 mg mL^{-1}) were more soluble in CHCl$_3$ than the non-fluorinated quinoidal oligothiophenes (**QT**: 0.7 mg mL^{-1}, **TQ**: 37.1 mg mL^{-1}, **TQ-TT**: 1.0 mg mL^{-1}). This phenomenon can be rationalized by assuming that the fluorine substitution restricts intermolecular C-H/π interactions.[9] The chemical structures of **FQT**, **FTQ**, and **FTQ-TT** were fully characterized by NMR and high resolution (HR)-MS. Detailed syntheses and characterization data are summarized in the experimental section. A TGA revealed that a 5% weight-loss temperature for **FQT**, **FTQ**, and **FTQ-TT** was 297, 298, and 241 °C, respectively, indicating that these compounds are sufficiently thermally stable under annealing conditions (Figure S3.2). Differential scanning calorimetry (DSC) measurements showed that **FQT** and **FTQ-TT** have no detectable phase transitions, whereas **FTQ** exhibited melting and crystallization peaks (Figure S3.3).

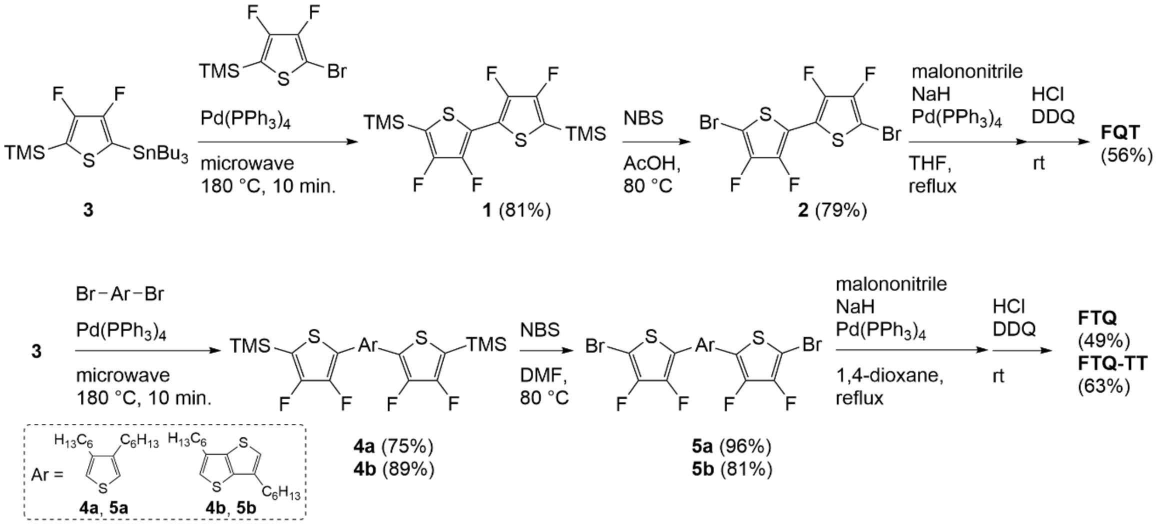

Scheme 3.1. Syntheses of **FQT**, **FTQ**, and **FTQ-TT**.

As discussed in chapter 1, at 0 °C, the ^{1}H NMR spectrum of **TQ** showed two sets of signals in the aromatic region (Figure 3.3(a)).[4] Based on nuclear Overhauser effect measurements, the large and small peaks were fully assigned to *anti-anti* and *anti-syn* isomers of the quinoidal oligothiophene backbone, respectively. These signals were broadened at 25 °C, implying that the two aromatic biradical forms were in equilibrium. In contrast, the ^{19}F NMR spectrum of **FTQ** showed one set of signals at both –45 and 25 °C (Figure 3.3(b)). This result indicates that the presence of intramolecular S–F attractive interactions contributed to fixing the *anti* conformations between adjacent thiophene rings. It should also be noted that the sharpness of peak (1) did not change irrespective of the temperature, whereas the peak (2) showed a substantial broadening at 25 °C. This phenomenon is rationalized by rotation of the dicyanomethylene moieties in **FTQ**. As shown in Figure S3.4, similar phenomena were observed for **TQ-TT** and **FTQ-TT**.

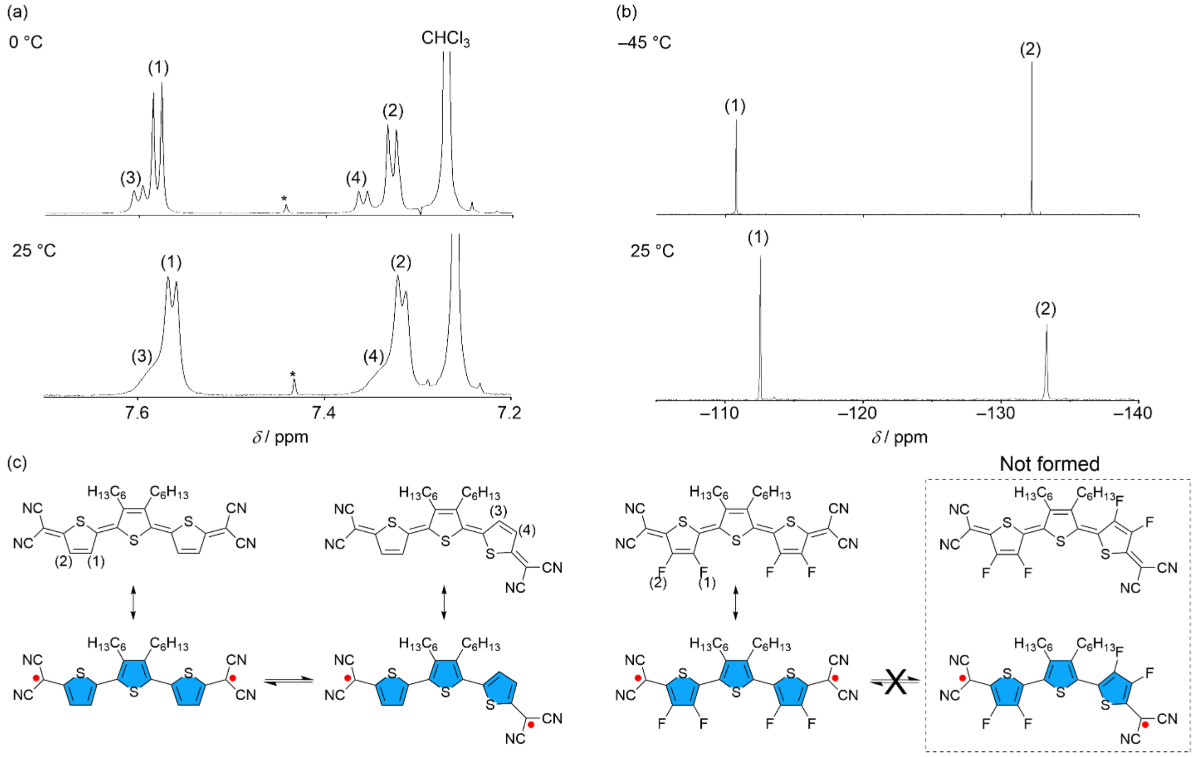

Figure 3.3. (a) ^{1}H NMR spectra of **TQ** and (b) ^{19}F NMR spectra of **FTQ** in the aromatic regions in $CDCl_3$. Signals marked by an asterisk are satellite peaks in $CHCl_3$. (c) Depiction of the conformational changes for **TQ** (left) and **FTQ** (right).

Single crystals of **FTQ** were obtained by the vapor diffusion from $CHCl_3$/hexane, and the structure was unambiguously determined by an X-ray crystallographic analysis. As shown in Figure 3.4(a), as expected, the molecular structure of **FTQ** adopts an *anti*-conformation and a planar geometry with dihedral angles of 4.7° and 2.8°. The distances between the sulfur atom of the central thiophene and the fluorine atoms of the adjacent thiophene units are 2.77 and 2.71 Å, which are shorter than the sum of the van der Walls radii of sulfur and fluorine atoms (3.27 Å). A similar intramolecular S–F contact is observed in the π-conjugated compounds containing thiophene rings and fluorine atoms.[4,5c] Based on the geometry of the single-crystal structure, the E_{CT} of **FTQ** using an NBO analysis was determined to be 1.66 and 2.00 kcal mol^{-1}, which are in good agreement with those estimated from the calculated optimized structure.

Concerning the packing diagram, the **FTQ** molecules are arranged in a slipped parallel arrangement with minimum intermolecular π–π distances of 3.41 Å (Figure 3.4(b)). It has been reported that the **TQ** framework with the butyl groups adopts different stacking structure with an anti-parallel arrangement in the packing layer. With the charge distribution in the ESP plots between **FTQ** and **TQ** in Figure 3.2(b), the observed slipped parallel structure in **FTQ** may originate from Coulombic attractive interactions between adjacent molecules. The transfer integrals between stacked structures were estimated using the ADF program at the PW91/TZP level (Figure 3.4(c)). The transfer integrals (*t*) of the LUMO are one order of magnitude higher than those of the HOMO, implying the availability of electron-transporting pathways along the stacking direction.

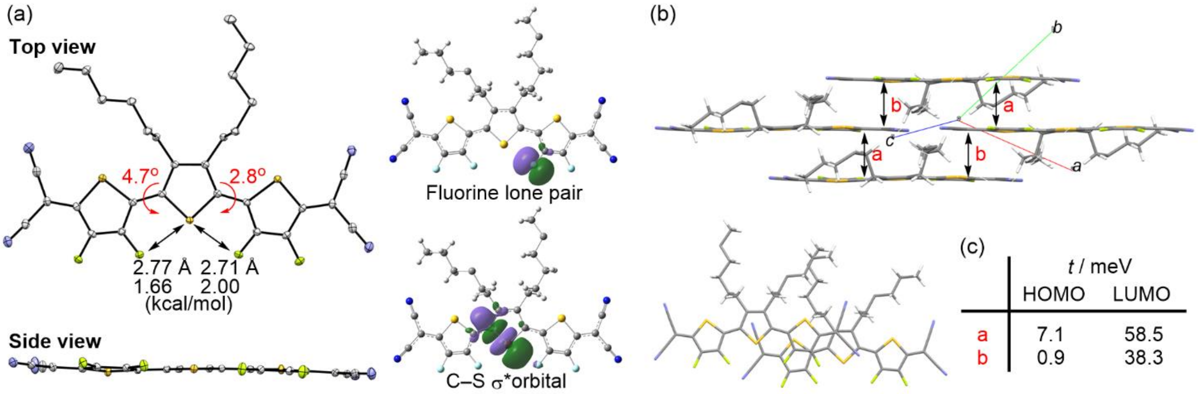

	t / meV	
	HOMO	LUMO
a	7.1	58.5
b	0.9	38.3

Figure 3.4. (a) ORTEP drawing of the molecular structure, (b) packing diagram from side view (top) and top view (bottom), and (c) estimated transfer integrals of HOMOs and LUMOs for **FTQ**.

3.4 Photophysical and Electrochemical Properties

UV-vis absorption spectra of the fluorinated quinoidal oligothiophenes (**FQT**, **FTQ**, and **FTQ-TT**) and the non-fluorinated quinoidal oligothiophenes (**QT**, **TQ**, and **TQ-TT**) in CH_2Cl_2 solutions and thin films are shown in Figure 3.5, and their photophysical data are summarized in Table 3.1. As shown in Figure 3.5, the absorption maxima (λ_{max}) of the fluorinated quinoidal oligothiophenes in solution are blue-shifted compared with those of non-fluorinated quinoidal oligothiophenes. These intense bands mainly represent HOMO–LUMO transition as confirmed by TD-DFT calculations at the B3LYP/6-31G (d,p) level of theory (see the experimental section). While the molar extinction coefficients (ε) of **FQT** and **FTQ** are higher than those of **QT** and **TQ**, **FTQ-TT** and **TQ-TT** showed almost identical ε values. This tendency was reproduced by the theoretically estimated oscillator strength (see the experimental section). As summarized in Table 3.1, the optical HOMO–LUMO energy gaps (ΔE_g^{opt}) of **FQT**, **FTQ**, and **FTQ-TT** estimated from the onsets in the solution spectra are close to those of **QT**, **TQ**, and **TQ-TT**. This trend is in good agreement with the theoretical results (Figure 3.2(a)). Compared to the solution spectra, broad absorption bands with red-shifted λ_{max} were observed for thin films of all of the compounds.

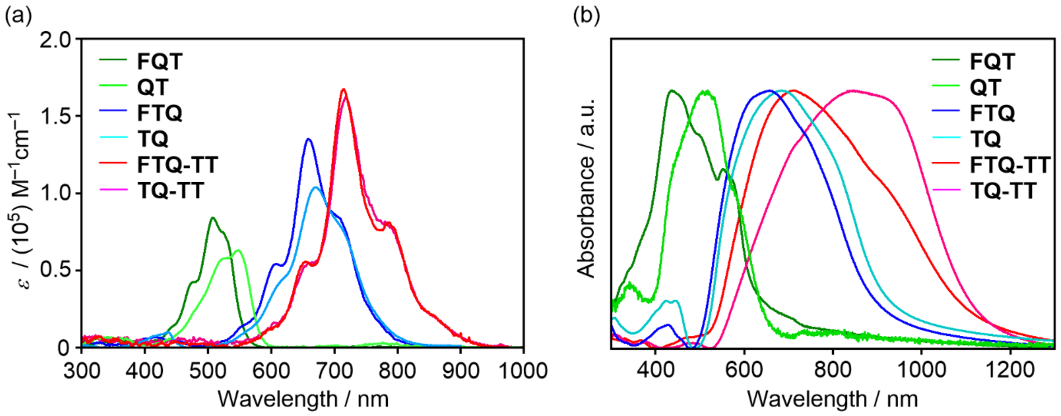

Figure 3.5. UV-vis-NIR absorption spectra of **FQT** (green), **QT** (light green), **FTQ** (blue), **TQ** (light blue), **FTQ-TT** (red), and **TQ-TT** (light red) (a) in CH_2Cl_2 and (b) in thin films.

The electrochemical properties of these compounds were investigated by cyclic voltammetry in CH_2Cl_2 containing 0.1 M $TBAPF_6$ as a supporting electrolyte. Ferrocene (Fc) was utilized as an external standard. The half-wave reduction potential ($E^{red}_{1/2}$) and oxidation potential ($E^{ox}_{1/2}$) and the estimated HOMO energy level (E_{HOMO}) and LUMO energy level (E_{LUMO}) are summarized in Table 3.1. We adopted the premise that the energy level of Fc/Fc^+ was −4.8 eV below the vacuum level. As shown in Figure 3.6, the CVs of both **FQT** and **QT** showed two one-electron reduction processes. On the other hand, **FTQ**, **FTQ-TT**, **TQ**, and **TQ-TT** showed first reduction waves with two-electron process, due to a decrease in on-site Coulomb repulsion in the dianion states for extended π-conjugated molecules.[10] Although **TQ** and **TQ-TT** did not show clear second reduction waves, **FTQ** and **FTQ-TT** showed a reversible second one-electron reduction process. The $E^{red}_{1/2}$ values of the fluorinated quinoidal molecules were positively shifted compared to those of **QT**, **TQ**, and **TQ-TT**. These results indicate that the formation of anionic species is both kinetically and thermodynamically stable due to the fluorine substitution. It should also be noted that the estimated E_{LUMO} of **FQT**, **FTQ**, and **FTQ-TT** were far below the criteria of −4.0 eV for air-stable n-type OFET materials.[1a,11]

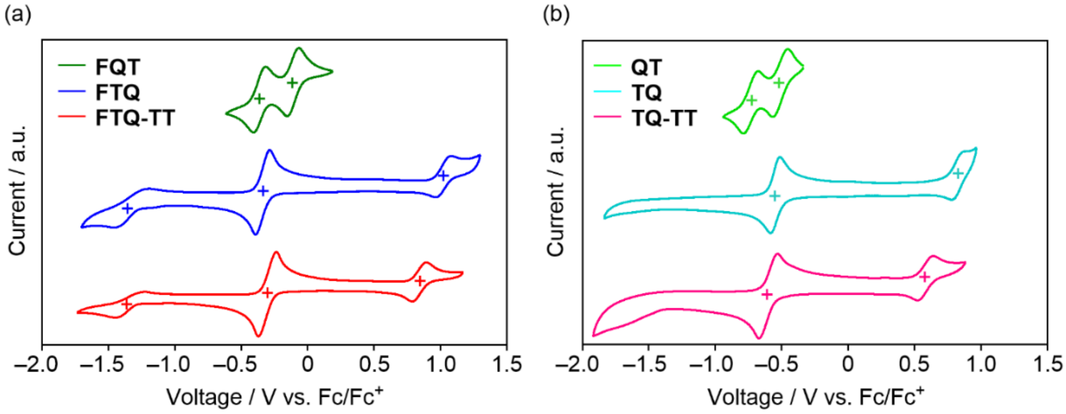

Figure 3.6. (a) CVs of **FQT** (green), **FTQ** (blue), and **FTQ-TT** (red) and (b) **QT** (light green), **TQ** (light blue), and **TQ-TT** (light red) in CH_2Cl_2 containing 0.1 M $TBAPF_6$.

Table 3.1. Photophysical and electrochemical properties.

Compounds	λ_{max} ($\varepsilon \times 10^5$) /nm (M^{-1} cm^{-1}) [a]	ΔE_g^{opt} /eV [b]	$E^{ox}_{1/2}$ /V [c]	$E^{red}_{1/2}$ /V [c]	E_{HOMO} /eV [d]	E_{LUMO} /eV [e]
FQT	507(0.8)	2.18	nd	–0.11, –0.36	nd	–4.69
FTQ	659 (1.4)	1.62	1.02	–0.34, –1.33	–5.82	–4.46
FTQ-TT	713 (1.6)	1.46	0.84	–0.30, –1.34	–5.64	–4.50
QT	548 (0.6)	2.13	nd	–0.51	nd	–4.29
TQ	670 (1.0)	1.60	0.81	–0.57	–5.61	–4.23
TQ-TT	717 (1.6)	1.46	0.56	–0.61	–5.36	–4.19

[a] In CH_2Cl_2. [b] Determined by the onset of the UV−vis spectra. [c] In CH_2Cl_2 containing $TBAPF_6$. [d] $E_{HOMO} = –E^{ox}_{1/2}–4.8$. [e] $E_{LUMO} = –E^{red}_{1/2}–4.8$.

3.5 Transistor Characteristics of Pristine Films

To investigate the crystallinity and morphologies of these compounds in the solid state, XRD and AFM measurements were performed on thin films. The thin films were fabricated onto HMDS-modified Si/SiO_2 substrates by spin-coating from $CHCl_3$ solutions. However, the low solubility of **FQT**, **QT**, and **TQ-TT** hampered the formation of uniform films. As shown in Figure 3.7 and Figure S3.5, AFM images revealed that thin films composed of **FTQ**, **FTQ-TT**, and **TQ** have relatively homogeneous microstructures with no observable grain boundaries. XRD peaks were not observed for the as spun **TQ** films (Figure S3.5), indicating amorphous behavior. However, a crystalline structure was formed after thermal annealing. In contrast, **FTQ** showed distinct diffraction peaks even before thermal annealing (Figure 3.7), indicating that the crystallinity was improved by the introduction of fluorine atoms in the case of **FTQ**. The intense XRD peak of **FTQ** at $2\theta = 4.0°$ corresponds to a *d*-spacing of 22.1 Å, which is almost equal to the length of the crystallographic *c*-axis (21.3 Å), indicating that the **FTQ** molecule adopts an edge-on orientation against the SiO_2 surface. The **FTQ-TT** thin films also showed crystalline behavior.

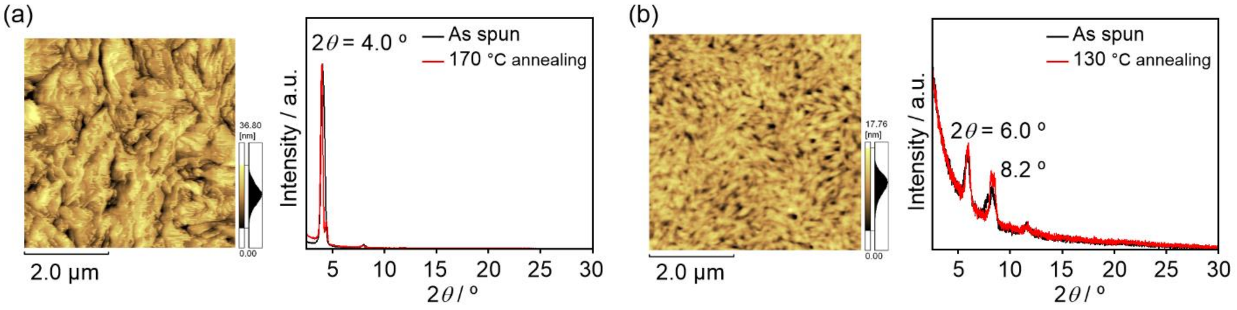

Figure 3.7. AFM height images and XRD data of (a) **FTQ** and (b) **FTQ-TT**.

To evaluate the carrier transport characteristics of **FTQ** and **FTQ-TT**, OFETs were fabricated with a bottom-gate/bottom-contact configuration. The thin films were prepared by spin-coating from 0.3 wt% $CHCl_3$ solutions onto HMDS-modified Si/SiO_2 substrates. The key transistor parameters obtained from the measurements are summarized in Table 3.2. As shown in Figure 3.8, **FTQ** and **FTQ-TT** showed typical n-type characteristics with electron mobilities (μ_e) in the range of 10^{-2}–10^{-3} cm^2 V^{-1} s^{-1} under vacuum conditions. Furthermore, the same order of μ_e was retained for **FTQ** and **FTQ-TT** after exposure to air for 24 h, and time-dependent electron-transport characteristics were summarized in Figure S3.6. The combination of the crystalline structure in the thin films with low-lying LUMO energy levels of less than −4.0 eV resulted in the development of kinetic stability against the intrusion of O_2 and/or H_2O and the thermodynamic stability of the anionic species.[12] The relatively low current on/off ratio (I_{on}/I_{off}) may be due to the existence of biradical character, resulting in the increase of carrier density even in the off state as mentioned in chapter 1.

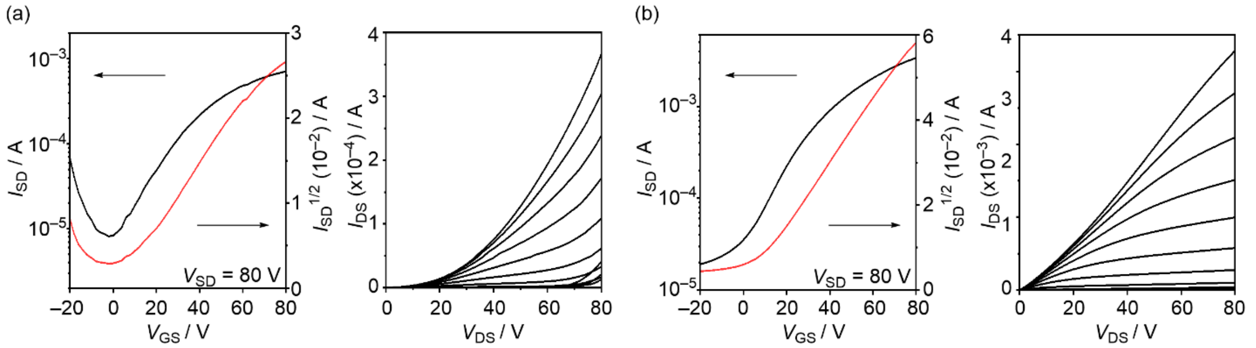

Figure 3.8. Transfer and output characteristics of OFETs using (a) **FTQ** and (b) **FTQ-TT**. V_{GS}, I_{SD}, and V_{DS} denotes gate voltage, source–drain current, and source–drain voltage, respectively.

3.6 Transistor Characteristics and Properties of Blend Films

Transistor characteristics based on blended films of p-type and n-type materials were evaluated,[6a, 13, 14] since it is still rare to obtain good ambipolar characteristics by utilizing OFETs based on small molecules.[15] In order to clarify the influence of fluorine substitution, we selected **FTQ** and **TQ** as n-type materials, because these compounds have a reliable solubility that is needed for the investigation. **TIPSP** was used as a soluble p-type material (structure shown in Figure 3.1). The active layers were prepared by spin-coating from 0.5/0.5 wt% $CHCl_3$ blend solutions of **FTQ**/**TIPSP** and **TQ**/**TIPSP** onto HMDS-modified Si/SiO_2 substrates without annealing. As shown in Figure 3.9, both blended films showed ambipolar behavior with well-balanced μ_e and hole mobility (μ_h) under vacuum conditions. However, the carrier mobilities of the **FTQ**/**TIPSP** blended films (μ_e: 4.6×10^{-4} cm^2 V^{-1} s^{-1}, μ_h: 8.5×10^{-4} cm^2 V^{-1} s^{-1}) had values that were two magnitudes higher than the corresponding values for those of the **TQ**/**TIPSP** blend films (μ_e: 2.3×10^{-6} cm^2 V^{-1} s^{-1}, μ_h: 4.3×10^{-6} cm^2 V^{-1} s^{-1}).

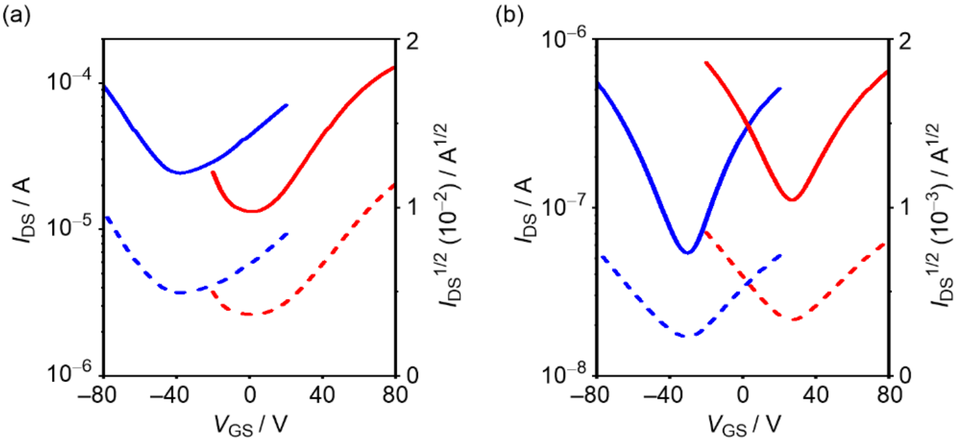

Figure 3.9. Transfer characteristics of OFET based on (a) **FTQ**/**TIPSP** and (b) **TQ**/**TIPSP** blended films (red and blue denote the n-channel and p-channel, respectively).

Table 3.2. Field-effect transistor characteristics under vacuum in air.

Compounds	Anneal temp. /°C	V_{th} /V	I_{on} / I_{off}	μ_e /cm^2 V^{-1} s^{-1} (μ_h /cm^2 V^{-1} s^{-1})
FTQ [a)]	170	3	10^2	4.1×10^{-3}
FTQ [b)]	170	–1	10^2	3.1×10^{-3}
FTQ-TT [a)]	130	–1	10^2	1.4×10^{-2}
FTQ-TT [b)]	130	–28	10^2	1.1×10^{-2}

[a)] Under vacuum. [b)] In air after 24h.

To understand the observed difference in carrier-transport characteristics, the properties of the blended films was investigated. UV-vis absorption spectra of the blended films and pristine films composed of **FTQ**, **TQ**, and **TIPSP** are shown in Figure S3.7. The blended film of **TQ** and **TIPSP** are regarded as a superimposition of pristine films. On the other hand, the **FTQ/TIPSP** film showed an apparent red-shift in the absorption with a λ_{max} of 800 nm, compared to those of pristine films. This result indicates the existence of electronic communication between **FTQ** and **TIPSP**. Similar behavior was observed for other fluorinated quinoidal oligothiophenes (Figure S3.8).

As shown in Figure S3.9(a), XRD measurements of the **FTQ/TIPSP** blended film exhibited clear diffraction peaks at $2\theta = 6.0°$ and 15.3°, which were different from the diffraction peaks of the pristine **FTQ** and **TIPSP** films. This result indicates that the co-crystals between **FTQ** and **TIPSP** are dominantly formed in the thin films. The XRD of the **TQ/TIPSP** blended film also showed a distinct peak at $2\theta = 6.0°$, which is different from the pristine films of **TQ** and **TIPSP** (Figure S3.9(b)). However, the peak strength was significantly lower than that of the XRD of the **FTQ/TIPSP** blended film.

The supramolecular organization in thin **TQ** and **FTQ** spin-coated films was investigated by grazing-incidence wide-angle X-ray scattering (GIWAXS). GIWAXS measurements provide valuable information about the film organization of the small molecules including their inter-stack distance and confirm results obtained by 1 dimensional XRD single crystal investigations. Samples were prepared by the same procedure as it was applied for OFET fabrication. The interlayer distance of 2.19 nm for both materials was determined from the main reflection (100 according to the Miller's index) observed at q_z = 0.286 Å^{-1} and q_{xy} = 0 Å^{-1} (Figure S3.10(a)). Higher order reflections (up to 3th) imply long-range organization of the molecules in the out-of-plane direction. This suggests that the long axis of the **TQ** and **FTQ** molecules are arranged perpendicular to the silicon dioxide surface. The main difference can be observed in the off-meridional plane where additional reflection for **FTQ** was observed (Figure S3.10(b)). This off-meridional reflection (at q_z= 0.346 Å^{-1} and q_{xy}= 0.115 Å^{-1}) confirmed the slipped parallel arrangement proposed by single crystal XRD investigation. Such reflections were not observed for the **TQ** molecule which suggests a typical inter-stack packing, previously observed with face-to-face slipped π-stacks proposed for molecule with **TQ** core and butyl substituent. For both materials, organization in the π-stacking direction cannot be confirmed by GIWAXS measurements due to too low intensity of the reflections in the wide angle range. The structures of **FTQ/TIPSP** and **TQ/TIPSP** blend films were also characterized by GIWAXS. As already mentioned, variation in molecular organization was observed between thin films of pristine **TQ** and

FTQ molecules. Interestingly, also mixtures of these quinoidal oligothiophene derivatives with **TIPSP** created different organization types (Figure 3.10(a)). **FTQ/TIPSP** gives a much better defined crystalline structure, evidenced by the high number of distinguished reflections. It should be noted that the position of the reflections in the pattern of **FTQ/TIPSP** blends does not correspond to the position of the reflections of pristine **FTQ** and **TIPSP** patterns (Figure 3.10(b)). The previously observed value of 2.19 nm for **FTQ** does not fit to the value of 1.5 nm observed at the meridional position in the **FTQ/TIPSP** film. To exclude the **TIPSP** organization motif, bare material has been additionally investigated by GIWAXS and the typical inter-stack distance of 1.69 nm was detected. Further variations of the reflections in the off-meridional plane were observed; the lack of peaks positioned at q_z= 0.346 Å^{-1} and q_{xy}= 0.115 Å^{-1} (described for **FTQ**) and appearance of reflections at q_z= 0.210 Å^{-1} and q_{xy}= 0.162 Å^{-1} suggests a completely new type of organization in the **FTQ/TIPSP** blend thin film. Additionally, new peaks located at the equatorial and off-equatorial plane appeared in the wide-angle region at q_z= 0.210 Å^{-1} and q_{xy}= 1.722 Å^{-1} as well as at q_z= 0.462 Å^{-1} and q_{xy}= 1.784 Å^{-1}, which can be assigned to π–π distances of 3.64 Å and 3.52 Å, respectively.

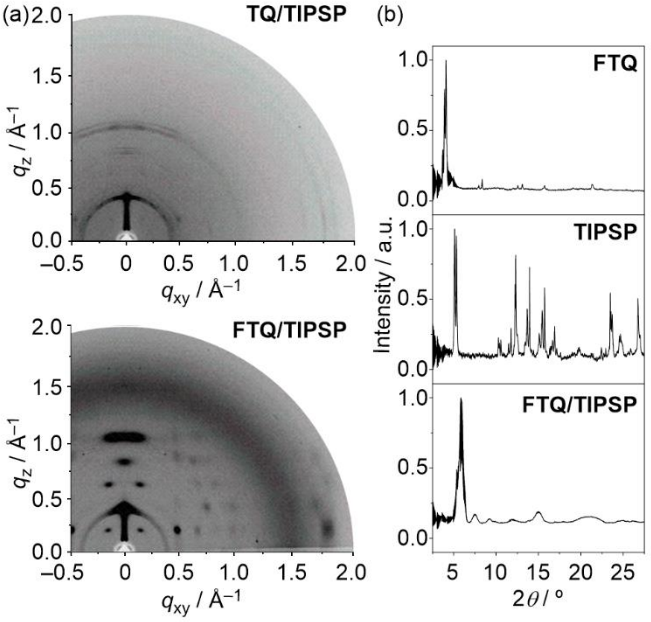

Figure 3.10. (a) GIWAXS patterns of **TQ/TIPSP** and **FTQ/TIPSP** spin-coated blends; (b) 2θ integration for **FTQ**, **TIPSP** and blend of **FTQ** and **TIPSP**.

To determine the molecular orientation of the molecules in the blend, single co-crystals of **FTQ** and **TIPSP** suitable for X-ray crystallographic analysis were successfully obtained by recrystallization using vapor diffusion from $CHCl_3$/hexane. As shown in Figure 3.11(a), **FTQ** and **TIPSP** are oriented in a face-to-face mixed-stack alignment with repeating structures of **FTQ–TIPSP–FTQ**. The observed intermolecular π–π distances between facial stacked structures were 3.45 and 3.32 Å (a and b in Figure 3.11(b), respectively). On the basis of the ADF calculations, this co-crystal possesses large *t* values for both hole-transport and electron-transport (Figure 3.11(b)). This estimation supports the appearance of balanced ambipolar characteristics for the **FTQ** and **TIPSP** blended films. These results demonstrate that the incorporation of fluorine atoms into n-type quinoidal oligothiophene frameworks promotes the formation of p-type/n-type dimer-type structures due to the complemental charge distribution symmetry against p-type molecules (Figure 3.11(c)).[16]

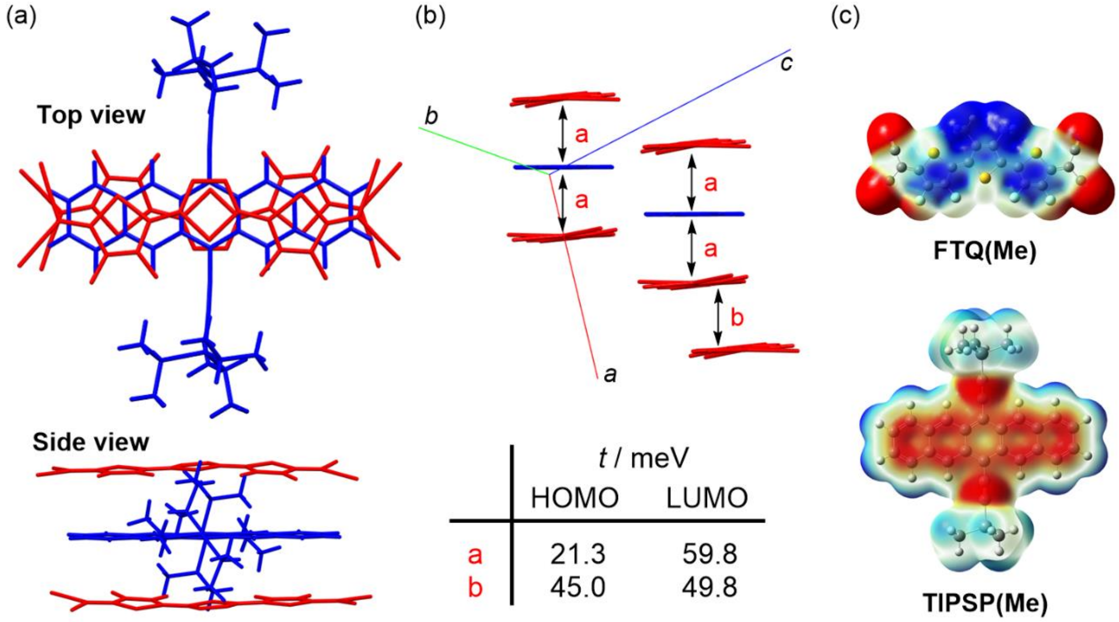

	t / meV	
	HOMO	LUMO
a	21.3	59.8
b	45.0	49.8

Figure 3.11. (a) Packing diagram from top view and side view, (b) estimated *t* values of HOMOs and LUMOs for the co-crystal of **FTQ** and **TIPSP**, and (c) ESP plots for **FTQ(Me)** and **TIPSP(Me)**.

3.7 Conclusion

In summary, a series of new bis(dicyanomethylene)-substituted quinoidal oligothiophenes with fluorine atoms at the β-positions in the thiophene rings was synthesized in order to investigate the influence of fluorine-substitution on their structures and properties. The results of theoretical calculations including NBO analyses as well as experimental results including NMR measurements and X-ray analyses indicated that these molecules have a fixed *anti*-conformation due to intramolecular S–F non-covalent interactions. Cyclic voltammetry measurements showed that the introduction of fluorine atoms contributed to increased electron-accepting characteristics and the formation of stable anionic species. OEFT devices based on these molecules exhibited air-stable n-type responses, which originate from their considerable low-lying LUMO energy levels and the well-aligned molecular structures in the thin films. Furthermore, a blended film of **FTQ** and **TIPSP** showed well-balanced ambipolar OFET characteristics. GIWAXS and X-ray analyses showed the formation of co-crystals of **FTQ** and **TIPSP**. These results demonstrate that the fluorine atoms in quinoidal oligothiophenes have advantages, not only for developing n-type semiconducting materials but also in constructing p-type/n-type complexes for applications in ambipolar devices.

3.8 Experimental Section

Supplementary Figures

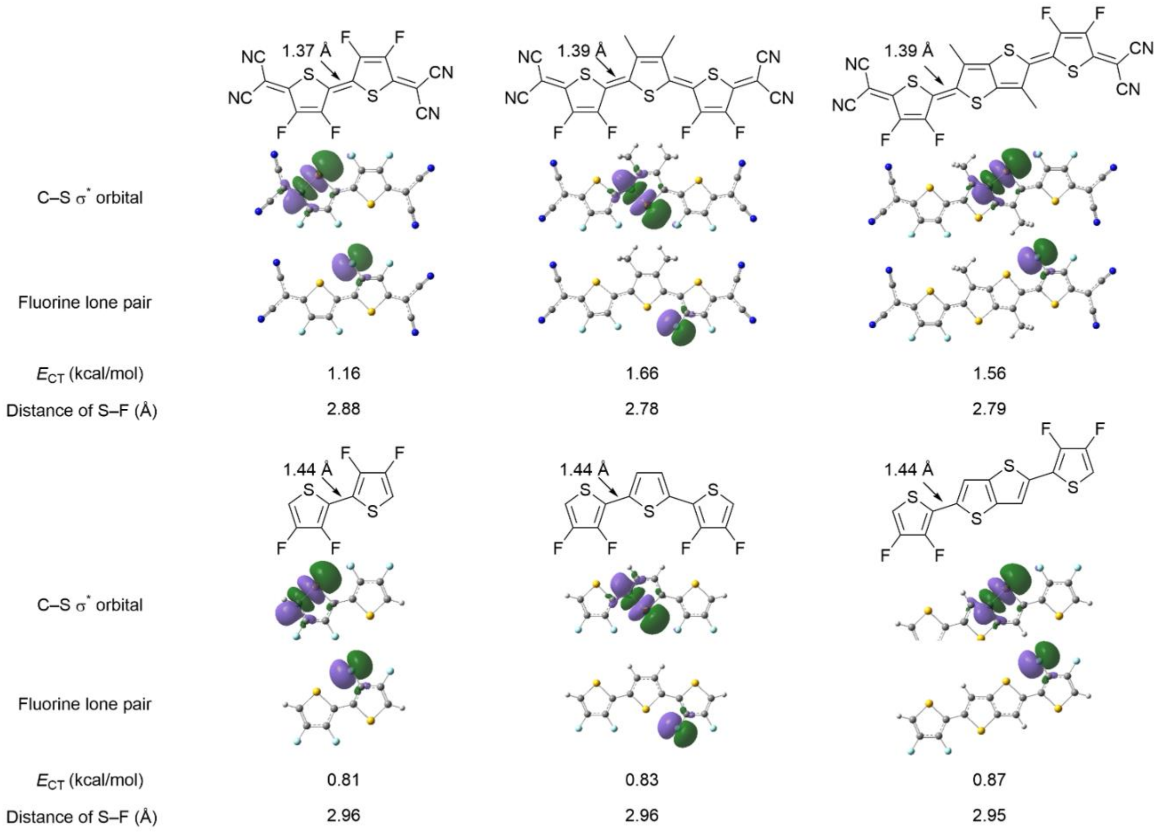

Figure S3.1. Depiction of the NBO orbitals for the optimized structures.

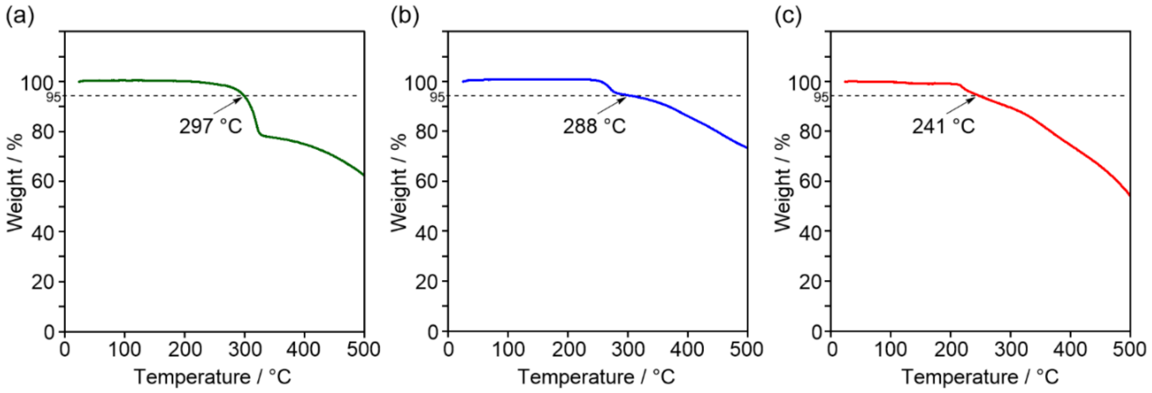

Figure S3.2. TGA curves for (a) **FQT**, (b) **FTQ**, and (c) **FTQ-TT** with a heating rate of 10 °C min^{-1} in a N_2 atmosphere.

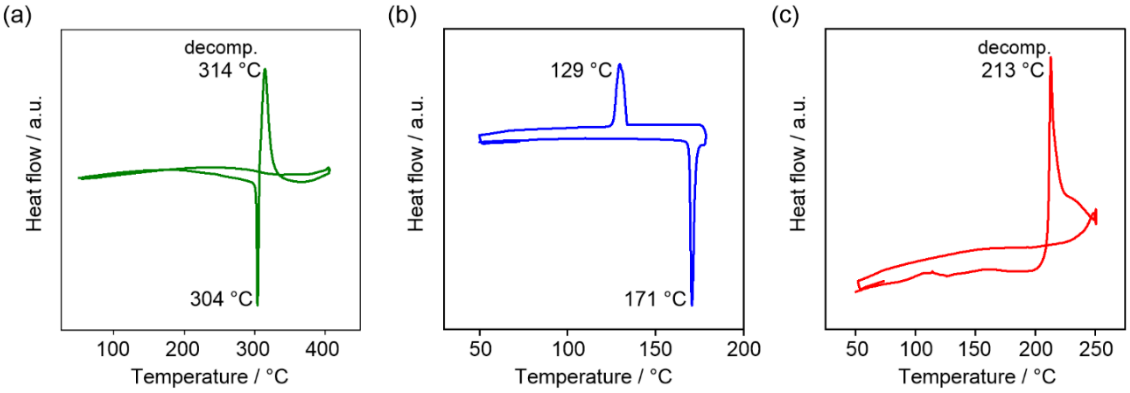

Figure S3.3. DSC curves of (a) **FQT**, (b) **FTQ**, and (c) **FTQ-TT** for a heating rate of 10 °C min^{-1} in a N_2 atmosphere.

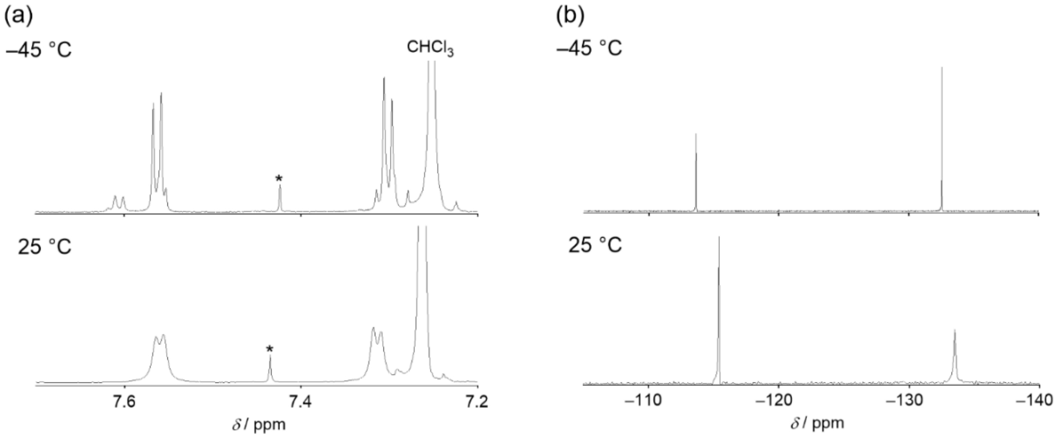

Figure S3.4. (a) ^{1}H NMR spectra of **TQ-TT** and (b) ^{19}F NMR spectra of **FTQ-TT** in the aromatic regions in $CDCl_3$. Signals marked by an asterisk are satellite peaks from $CHCl_3$.

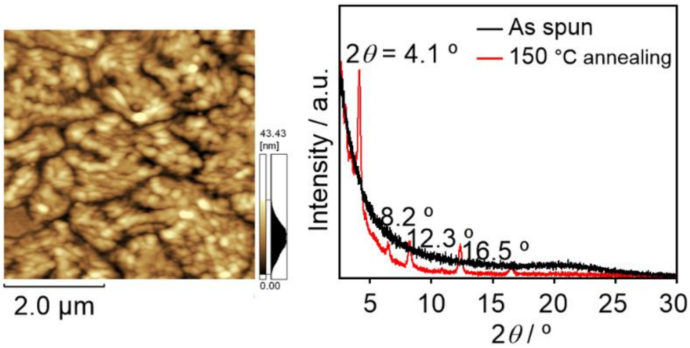

Figure S3.5. AFM height image and XRD data for **TQ**.

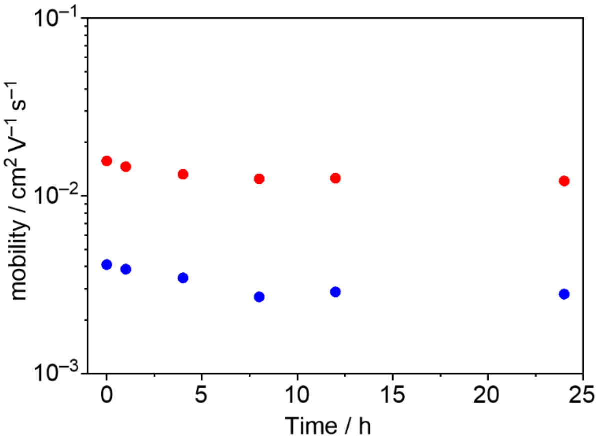

Figure S3.6. Time-dependent electron mobilities under air-exposed conditions for **FTQ** (blue) and **FTQ-TT** (red).

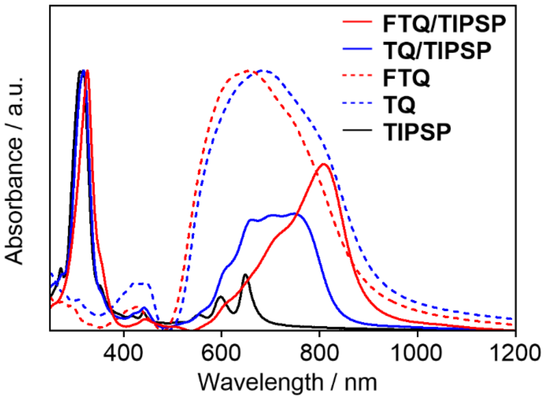

Figure S3.7. UV-vis-NIR absorption spectra of **FTQ/TIPSP** blend (red, solid line), **TQ/TIPSP** blend (blue, solid line), **FTQ** (red, dashed line), **TQ** (blue, dashed line), and **TIPSP** (black. Solid line) in thin films.

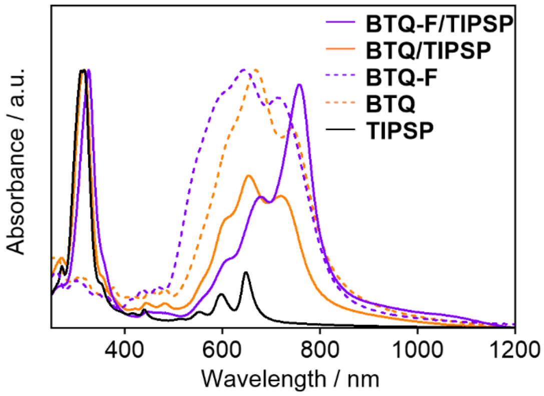

Figure S3.8. UV-vis-NIR absorption spectra of **BTQ-F/TIPSP** (purple, solid line), **BTQ/TIPSP** (orange, solid line), **BTQ-F** (purple, dashed line), **BTQ** (orange, dashed line), and **TIPSP** (black, solid line) in thin films.

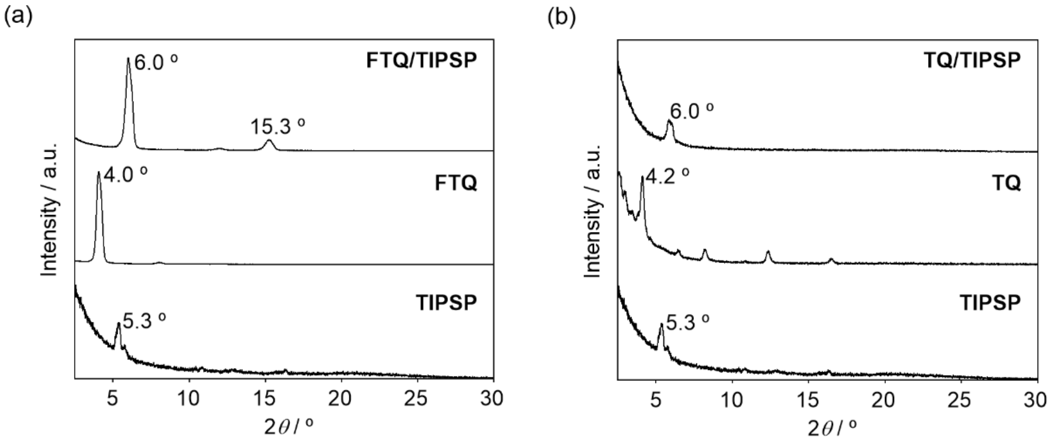

Figure S3.9. XRD data of (a) **FTQ/TIPSP** blend (Top), **FTQ** (middle), **TIPSP** (bottom), and (b) **TQ/TIPSP** blend (Top), **TQ** (middle), **TIPSP** (bottom).

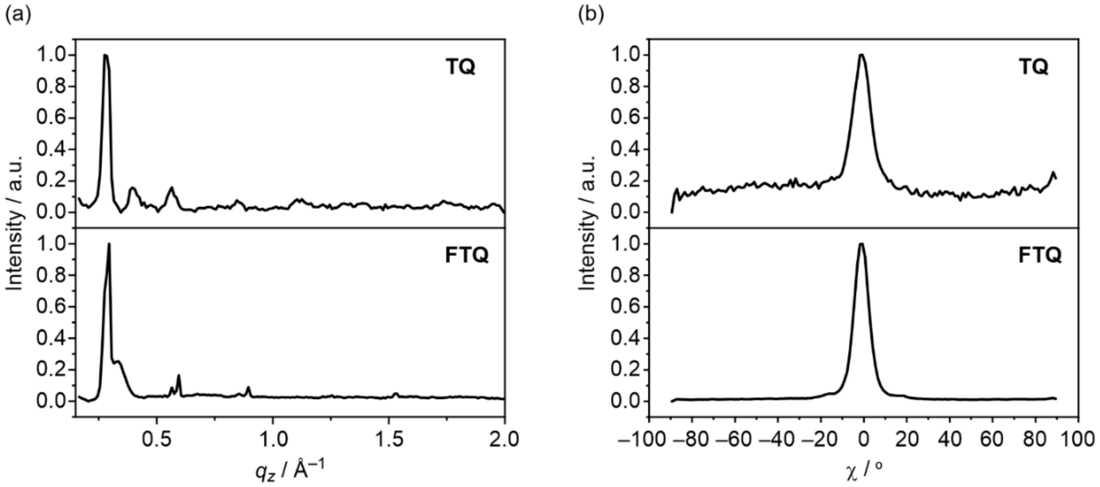

Figure S3.10. (a) Meridional integration for **TQ** and **FTQ** obtained from GIWAXS patterns of spin-coated thin films; (b) azimuthal integration intensity containing (100) reflection for **TQ** and **FTQ**.

General Information

Column chromatography was performed on silica gel. KANTO Chemical silica gel 60N (40–50 μm). Thin-layer Chromatography (TLC) plates were visualized with UV light. Preparative GPC was performed on a Japan Analytical LC-918 equipped with JAI-GEL 1H/2H. ^{1}H and ^{13}C NMR spectra were recorded on a JEOL JNM-ECS400 or JEOL JNM-ECA600 spectrometer in $CDCl_3$ with TMS as an internal standard. ^{19}F NMR spectra were recorded on a JEOL JNM-ECA600 spectrometer in CDCl3. Data are reported as follows: chemical shift in ppm (*δ*), multiplicity (s = singlet, d = doublet, t = triplet, m = multiplet, br = broad), coupling constant (Hz), and integration. Mass spectra were obtained on a Shimadzu AXIMA-TOF. UV-vis spectra were recorded on a Shimadzu UV-3600 spectrophotometer. All spectra were obtained in spectrograde solvents. Cyclic voltammetry was carried out on a BAS CV-620C voltammetric analyzer using a platinum disk as the working electrode, platinum wire as the counter electrode, and Ag/AgNO$_3$ as the reference electrode at a scan rate of 100 mV s^{-1}. High-resolution mass spectrum (HRMS) was obtained atmospheric pressure chemical ionization (APCI) or electrospray ionization (ESI) methods using a Thermo scientific LTQ Orbitrap XL.Elemental analyses were performed on PerkinElmer LS-50B by the elemental analysis section of the Comprehensive Analysis Center (CAC) of ISIR, Osaka University. The surface structures of the deposited organic films were observed by atomic force microscopy (Shimadzu, SPM9600), and the film crystallinity was evaluated by an X-ray diffractometer (Rigaku, SmartLab). X-ray diffraction patterns were obtained using Bragg-Brentano geometry with CuKα radiation as an X-ray source with an acceleration voltage of 45 kV and a beam current of 200 mA. The scanning mode was set to 2θ–θ scans between 2º–30º with scanning steps of 0.01º.

OFET Device Fabrication and Evaluation

The field-effect electron mobility was measured using bottom-gate bottom-contact OFET devices. The p-doped silicon substrate functions as the gate electrode. A thermally grown silicon oxide (SiO$_2$) dielectric layer on the gate substrate has 300 nm thick and a capacitance of 10.0 nF cm^{-2}. Interdigital source and drain electrodes were constructed with gold (30 nm) that were formed on the SiO$_2$ layer. The channel width (W) and channel length (L) are 38 mm and 5 μm, respectively. The silicon oxide surface was first washed with toluene, acetone, purified water and 2-propanol. It was then activated by ozone treatment and pretreated with HMDS. The semiconducting layer was fabricated by spin coating from 0.3 wt% chloroform solution at 1000 rpm for 1 min onto the substrate in air for **FTQ** and **FTQ-TT**, followed by annealing for 90 min at various temperatures under a vacuum condition (10^{-3}Pa). The characteristics of the OFETs were measured at room temperature under a pressure of 10^{-3} Pa by using a KEITHLEY 4200 semiconductor parameter analyzer. The μ_e was calculated in the saturated region by the following equation.

$$I_{DS} = \frac{W}{2L} C_i \mu (V_{GS} - V_{th})^2$$

Current on/off ratio was determined from the I_D sat V_{GS}= 0 V (I_{off}) and V_{GS}= 80 V (I_{on}).

GIWAXS Measurements

The films deposited by spin-coating were performed at the DELTA Synchrotron using beamline BL09 with a photon energy of 10 keV. The beam size was 1.0 mm × 0.2 mm (width x height), and samples were irradiated just below the critical angle for total reflection with respect to the incoming X-ray beam (~0.1°). The scattering intensity was detected on a 2-D image plate (MAR-345) with a pixel size of 150 μm (2300 × 2300 pixels), and the detector was placed 523 mm from the sample center. All X-ray scattering measurements were performed under vacuum (~1mbar) to reduce air scattering and beam damage to the sample. All 2DWAXS data processing and analysis was performed by using the software package Datasqueeze (http://www.datasqueezesoftware.com).

Computational Details

All calculations were conducted using Gaussian 09 program. The geometry was optimized with the restricted Becke Hybrid (B3LYP) at 6-31 G(d,p) level.

TD-DFT Calculation

FQT

Excited State 1: Singlet-A 2.61 eV 474 nm *f* = 1.58 <S**2>=0.000
HOMO > LUMO 0.70776
HOMO < LUMO 0.11597

FTQ(Me)

Excited State 1: Singlet-A 2.12 eV 586 nm *f* = 2.14 <S**2>=0.000
HOMO > LUMO 0.70816
HOMO < LUMO 0.12439

FTQ-TT(Me)

Excited State 1: Singlet-A 1.96 eV 632 nm *f* = 2.63 <S**2>=0.000
HOMO > LUMO 0.70965
HOMO < LUMO 0.13242

QT

Excited State 1: Singlet-A 2.57 eV 483 nm *f* = 1.37 <S**2>=0.000
HOMO > LUMO 0.70399
HOMO < LUMO 0.10769

TQ(Me)

Excited State 1: Singlet-A 2.11 eV 589 nm *f* = 1.98 <S**2>=0.000
HOMO > LUMO 0.70613
HOMO < LUMO 0.11819

TQ-TT(Me)

Excited State 1: Singlet-A 1.96 eV 634 nm *f* = 2.51 <S**2>=0.000
HOMO–1> LUMO+1 0.10533
HOMO > LUMO 0.70790
HOMO < LUMO 0.12771

Synthesis

Unless stated otherwise, all reagents were purchased from commercial sources and used without purification. Compounds **1**, **3**, 2,5-dibromo-3,4-dihexylthiophene and 2,5-dibromo-3,6-dihexylthieno[3,2-*b*]thiophene were prepared by the reference procedures.[17-20]

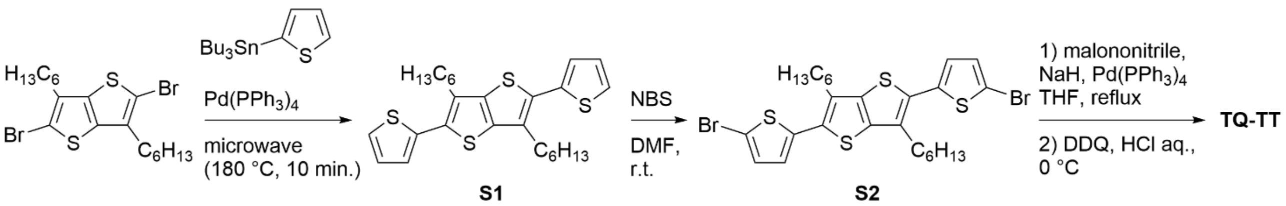

Scheme S3.1. Synthetic route for **TQ-TT**.

Synthesis of ***2***: NBS (226 mg, 1.27 mmol) was added to a solution of **1** (220 mg, 0.575 mmol) in AcOH (4.0 mL) at ambient temperature. The reaction was allowed to warm to 80 °C. After stirring for 4 h, the reaction mixture was poured into water. The resulting mixture was extracted with Et_2O. The organic layer was washed with 1 M aq. NaOH, water and dried over $MgSO_4$. The solvent was removed under reduced pressure, followed by purification with preparative GPC ($CHCl_3$) to give **2** (180 mg, 79%) as a white solid. ^{19}F NMR (565 MHz, $CDCl_3$): δ –133.3, –130.9; ^{13}C NMR (150 MHz, $CDCl_3$, TMS): δ 92.2-92.4 (m), 111.1-111.3 (m), 141.1 (dd, J = 270.2 and 20.2 Hz), 144.3 (dd, J = 263.0 and 20.2 Hz).

Synthesis of ***FQT***: Sodium hydride (60% in oil) (84 mg, 2.11 mmol) was added to a suspension of malononitrile (69 mg, 1.05 mmol) in anhydrous THF (12.5 mL) under nitrogen atmosphere and stirred for 10 min at room temperature. To this mixture was added compound **2** (174 mg, 0.439 mmol) and $Pd(PPh_3)_4$ (51 mg, 0.044 mmol), which was then heated to reflux. After 12 h, the reaction was cooled to 0 °C, and diluted hydrochloric acid (1M, 7.8 mL), $CHCl_3$ (7.8 mL), and DDQ (150 mg, 0.659 mmol) were added and stirred at 0 °C for 5 min. The resulting mixture was extracted with $CHCl_3$, washed with water, and dried over $MgSO_4$. The solvent was removed under reduced pressure and purified by column chromatography on silica gel ($CHCl_3$) to give **FQT** (89 mg, 56%) as a red solid. ^{19}F NMR (565 MHz, $CDCl_3$): δ –127.5, –118.7; HRMS (APCI) *m/z*: $[M]^-$ calcd. for $C_{14}F_4N_4S_2$, 363.9501; found, 363.9503.

Synthesis of ***4a***: 2,5-Dibromo-3,4-dihexylthiophene (119 mg, 0.290 mmol), **3** (307 mg, 0.638 mmol), $Pd(PPh_3)_4$ (34 mg, 0.029 mmol), and toluene (3.5 mL) were placed in a microwave proof walled glass vial equipped with a snap cap. The glass vial was purged nitrogen, securely sealed, and heated in a microwave reactor with keeping a temperature at 180 °C for 10 min. The reaction mixture was passed through pad of celite and the solvent was removed under reduced pressure, followed by purification with preparative GPC ($CHCl_3$) to give **4a** (138 mg, 75%) as a pale yellow solid. ^1H NMR (600 MHz, $CDCl_3$, TMS): δ 0.36 (s, 18H), 0.88 (t, J = 6.9 Hz, 6H), 1.25-1.38 (m, 12H), 1.47-1.52 (m, 4H), 2.62 (t, J = 8.3 Hz, 4H); ^{19}F NMR (565 MHz, $CDCl_3$): δ –134.1, –127.1; ^{13}C NMR (150 MHz, $CDCl_3$, TMS): δ –0.8, 14.1, 22.5, 28.1, 29.4, 30.4, 31.4, 114.6 (d, J = 24.6 Hz), 118.5 (d, J = 11.6 Hz), 126.6, 142.2, 142.4 (dd, J = 267.3 and 24.6 Hz), 149.6 (dd, J = 257.2 and 18.8 Hz); HRMS (APCI) *m/z*: $[M+H]^+$ calcd. for

$C_{30}H_{44}F_4S_3Si_2$, 633.2153; found, 633.2145.

Synthesis of ***5a***: NBS (85 mg, 0.475 mmol) was added to a solution of **4a** (137 mg, 0.216 mmol) in DMF (5.0 mL) at 0 °C. The reaction was allowed to warm to ambient temperature. After stirring for 4 h, the reaction mixture was poured into water. The resulting mixture was extracted with EtOAc. The organic layer was washed with water, brine and dried over $MgSO_4$. The solvent was removed under reduced pressure, followed by purification with preparative GPC ($CHCl_3$) to give **5a** (134 mg, 96%) as a pale yellow solid. ^1H NMR (600 MHz, $CDCl_3$, TMS): δ 0.89 (t, J = 6.2 Hz, 6H), 1.25-1.38 (m, 12H), 1.44-1.50 (m, 4H), 2.58 (t, J = 8.3 Hz, 4H); ^{19}F NMR (565 MHz, $CDCl_3$): δ –132.3, –130.9; ^{13}C NMR (150 MHz, $CDCl_3$, TMS): δ 14.0, 22.5, 28.1, 29.5, 30.4, 31.4, 91.3-91.5 (m), 113.7 (d, J = 11.6 Hz), 125.4, 141.1 (dd, J = 265.7 and 18.6 Hz), 143.3, 144.3 (dd, J = 262.8 and 20.1 Hz); HRMS (APCI) *m/z*: $[M]^+$ calcd. for $C_{24}H_{26}Br_2F_4S_3$, 645.9479; found, 645.9468.

Synthesis of ***FTQ***: Sodium hydride (60% in oil) (40 mg, 0.94 mmol) was added to a suspension of malononitrile (33 mg, 0.50 mmol) in anhydrous 1,4-dioxane (5.9 mL) under nitrogen atmosphere and stirred for 10 min at room temperature. To this mixture was added compound **5a** (134 mg, 0.207 mmol) and $Pd(PPh_3)_4$ (24 mg, 0.021 mmol), which was then heated to reflux. After 12 h, the reaction was cooled to 0 °C, and diluted hydrochloric acid (1M, 6.0 mL), $CHCl_3$ (6.0 mL) and DDQ (71 mg, 0.31 mmol) were added and stirred at 0 °C for 5 min. The resulting mixture was extracted with $CHCl_3$, washed with water, and dried over $MgSO_4$. The solvent was removed under reduced pressure and purified by column chromatography on silica gel (hexane/CH_2Cl_2, 1:2) to give **FTQ** (62 mg, 49%) as a blue solid. ^1H NMR (400 MHz, $CDCl_3$, TMS): δ 0.93 (t, J = 6.9 Hz, 6H), 1.30-1.42 (m, 8H), 1.48-1.62 (m, 8H), 2.78-2.84 (m, 4H); ^{19}F NMR (565 MHz, $CDCl_3$): δ –133.3, –112.6; HRMS (APCI) *m/z*: $[M]^-$ calcd. for $C_{30}H_{26}F_4N_4S_3$, 614.1256; found, 614.1224.

Synthesis of ***4b***: 2,5-Dibromo-3,6-dihexylthieno[3,2-*b*]thiophene (152 mg, 0.326 mmol), **3** (345 mg, 0.717 mmol), $Pd(PPh_3)_4$ (38 mg, 0.033 mmol), and toluene (5.0 mL) were placed in a microwave proof walled glass vial equipped with a snap cap. The glass vial was purged nitrogen, securely sealed, and heated in a microwave reactor with keeping a temperature at 180 °C for 10 min. The reaction mixture was passed through pad of celite and the solvent was removed under reduced pressure, followed by purification with preparative GPC ($CHCl_3$) to give **4b** (200 mg, 89%) as a yellow solid. ^1H NMR (600 MHz, $CDCl_3$, TMS): δ 0.37 (s, 18H), 0.87 (t, J = 6.2 Hz, 6H), 1.25-1.40 (m, 12H), 1.71-1.76 (m, 4H), 2.79 (t, J = 8.3 Hz, 4H); ^{19}F NMR (565 MHz, $CDCl_3$): δ –134.1, –126.8; ^{13}C NMR (150 MHz, $CDCl_3$, TMS): δ –0.7, 14.2, 22.7, 28.9, 29.0, 29.4, 31.6, 115.3 (d, J = 24.6 Hz), 119.1 (d, J = 11.6 Hz), 126.4, 134.5, 139.9, 142.6 (dd, J = 267.3 and 24.6 Hz), 149.8 (dd, J = 258.7 and 18.8 Hz); HRMS (APCI) *m/z*: $[M+H]^+$ calcd. for $C_{32}H_{44}F_4S_4Si_2$, 689.1874; found, 689.1864.

Synthesis of ***5b***: NBS (114 mg, 0.638 mmol) was added to a solution of **4b** (200 mg, 0.290 mmol) in DMF (13.6 mL) at 0 °C. The reaction was allowed to warm to ambient temperature. After stirring for 14 h, the reaction mixture was poured into water. The resulting mixture was extracted with EtOAc. The organic layer was washed with water, brine and dried over $MgSO_4$. The solvent was removed under reduced pressure, followed by purification with preparative GPC ($CHCl_3$) to give **5b** (165 mg, 81%) as a pale yellow solid. ^1H NMR (600 MHz, $CDCl_3$, TMS): δ 0.88 (t, J = 6.2 Hz, 6H), 1.25-1.40 (m, 12H), 1.68-1.73 (m, 4H), 2.75 (t, J = 8.3 Hz, 4H); ^{19}F NMR (565 MHz, $CDCl_3$): δ –132.1, –131.2; ^{13}C NMR (150 MHz, $CDCl_3$, TMS): δ 14.1, 22.6, 28.7, 28.8, 29.3, 31.5, 91.6-91.8 (m), 114.4 (d, J = 11.6 Hz), 124.8, 135.5, 139.9, 141.1 (dd, J = 265.8 and 20.1 Hz), 144.4 (dd, J = 261.5 and 20.3 Hz); HRMS (APCI) *m/z*: $[M]^+$ calcd. for $C_{26}H_{26}Br_2F_4S_4$, 701.9200; found, 701.9193.

Synthesis of ***FTQ-TT***: Sodium hydride (60% in oil) (23 mg, 0.57 mmol) was added to a suspension of malononitrile (19 mg, 0.28 mmol) in anhydrous 1,4-dioxane (3.5 mL) under nitrogen atmosphere and stirred for 10 min at room temperature. To this mixture was added compound **5b** (83 mg, 0.12 mmol) and $Pd(PPh_3)_4$ (14 mg, 0.012 mmol), which was then heated to reflux. After 18 h, the reaction was cooled to 0 °C, and diluted hydrochloric acid (1M, 3.6 mL), $CHCl_3$ (3.6 mL) and DDQ (40 mg, 0.18 mmol) were added and stirred at 0 °C for 10 min. The resulting mixture was extracted with $CHCl_3$, washed with water, and dried over $MgSO_4$. The solvent was removed under reduced pressure and purified by column chromatography on silica gel (hexane/CH_2Cl_2, 1:2) to give **FTQ-TT** (50 mg, 63%) as a blue solid. ^1H NMR (400 MHz, $CDCl_3$, TMS): δ 0.92 (t, J = 6.9 Hz, 6H), 1.32-1.52 (m, 12H), 1.70-1.78 (m, 4H), 2.89 (t, J = 7.8 Hz, 4H); ^{19}F NMR (565 MHz, $CDCl_3$): δ –127.5, –118.7; HRMS (APCI) *m/z*: $[M]^-$ calcd. for $C_{32}H_{26}F_4N_4S_4$, 670.0976; found, 670.0941.

Synthesis of ***S1***: 2-(Tributylstannyl)thiophene (230 mg, 0.616 mmol), 2,5-dibromo-3,6-dihexylthieno[3,2-*b*]thiophene (130 mg, 0.279 mmol), $Pd(PPh_3)_4$ (32 mg, 0.028 mmol), and toluene (4.3 mL) were placed in a microwave proof walled glass vial equipped with a snap cap. The glass vial was purged nitrogen, securely sealed, and heated in a microwave reactor with keeping a temperature at 180 °C for 10 min. The reaction mixture was passed through pad of celite and the solvent was removed under reduced pressure, followed by purification with preparative GPC ($CHCl_3$) to give **S1** (200 mg, 89%) as a brown solid. ^1H NMR (400 MHz, $CDCl_3$, TMS): δ 0.88 (t, J = 6.9 Hz, 6H), 1.25-1.45 (m, 12H), 1.71-1.80 (m, 4H), 2.87 (t, J = 8.2 Hz, 4H), 7.09 (dd, J = 5.0, and 3.7 Hz, 2H), 7.17 (dd, J = 3.7 and 0.9 Hz, 2H), 7.35 (dd, J = 5.0 and 0.9 Hz, 2H); ^{13}C NMR (100 MHz, $CDCl_3$, TMS): δ 14.1, 22.6, 28.8, 29.1, 29.4, 31.6, 125.7, 126.2, 127.5, 131.3, 132.0, 136.6, 138.5; HRMS (APCI) *m/z*: $[M+H]^+$ calcd. for $C_{26}H_{32}S_4$, 473.1460; found, 473.1446.

Synthesis of ***S2***: NBS (166 mg, 0.930 mmol) was added to a solution of **S1** (220 mg, 0.465 mmol) in DMF (24 mL) and THF (6 mL) at 0 °C. The reaction was allowed to warm to ambient temperature. After stirring for 10 h, the reaction mixture was poured into water. The resulting mixture was extracted with EtOAc. The organic layer was washed with water, brine and dried over $MgSO_4$. The solvent was removed under reduced pressure, followed by purification with preparative GPC ($CHCl_3$) to give **S2** (250 mg, 85%) as a pale yellow solid. ^1H NMR (400 MHz, $CDCl_3$, TMS): δ 0.88 (t, J = 6.9 Hz, 6H), 1.22-1.45 (m, 12H), 1.65-1.80 (m, 4H), 2.82 (t, J = 8.2 Hz, 4H), 6.90 (d, J = 3.7 Hz, 2H), 7.04 (d, J = 3.7 Hz, 2H); ^{13}C NMR (100 MHz, $CDCl_3$, TMS): δ 14.1, 22.6, 28.7, 29.1, 29.3, 31.6, 126.5, 130.3, 130.7, 132.5, 137.9, 138.6; HRMS (APCI) *m/z*: $[M+H]^+$ calcd. for $C_{26}H_{30}Br_2S_4$, 630.9650; found, 630.9644.

Synthesis of ***TQ-TT***: Sodium hydride (60% in oil) (43 mg, 1.07 mmol) was added to a suspension of malononitrile (35 mg, 0.53 mmol) in anhydrous THF (6.4 mL) under nitrogen atmosphere and stirred for 10 min at room temperature. To this mixture was added compound **S2** (140 mg, 0.222 mmol) and $Pd(PPh_3)_4$ (26 mg, 0.022 mmol), which was then heated to reflux. After 12 h, the reaction was cooled to 0 °C, and diluted hydrochloric acid (1M, 6.0 mL), $CHCl_3$ (6.0 mL) and DDQ (76 mg, 0.33 mmol) were added and stirred at 0 °C for 10 min. The resulting mixture was extracted with $CHCl_3$, washed with water, and dried over $MgSO_4$. The solvent was removed under reduced pressure and purified by column chromatography on silica gel (hexane/$CHCl_3$, 1:10) to give **TQ-TT** (50 mg, 38%) as a blue solid. ^{1}H NMR (600 MHz, $CDCl_3$, TMS): δ 0.92 (t, J = 7.3 Hz, 6H), 1.32-1.52 (m, 12H), 1.70-1.78 (m, 4H), 2.86 (t, J = 8.2 Hz, 4H), 7.31 (d, J = 5.5 Hz, 2H), 7.56 (d, J = 5.5 Hz, 2H); HRMS (APCI) *m/z*: $[M+H]^+$ calcd. for $C_{32}H_{30}N_4S_4$, 599.1426; found, 599.1422.

3.9 References

1 (a) Yui, K.; Aso, Y.; Otsubo, T.; Ogura, F. *Bull. Chem. Soc. Jpn*. **1989**, *62*, 1539. (b) Takimiya, K.; Aso, Y.; Otsubo, T.; Ogura, F. *Bull. Chem. Soc. Jpn*. **1991**, *64*, 2091. (c) Ogura, F.; Otsubo, T.; Aso, Y. *Pure Appl. Chem*. **1993**, *65*, 682.

2 Chonan, T.; Takahashi, K. *Bull. Chem. Soc. Jpn.*, 2004, **77**, 1487–1497.

3 (a) Berlin, A.; Grimoldi, S.; Zotti, G.; Osuna, R. M.; Delgado, M. C. R.; Ortiz, R. P.; Casado, J.; Hernández, V.; Navarrete, J. T. L. *J. Phys. Chem. B* **2005**, *109*, 22308. (b) Zotti, G.; Zecchin, S.; Vercelli, B.; Berlin, A.; Casado, J.; Hernández, V.; Ortiz, R. P.; Navarrete, J. T. L.; Ortí, E.; Viruela, P. M.; Milián, B. *Chem. Mater*. **2006**, *18*, 1539.

4 Yamamoto, K.; Ie, Y.; Nitani, M.; Tohnai, N.; Kakiuchi, F.; Zhang, K.; Pisula, W.; Asadi, K.; Blom, P. W. M.; Aso, Y. *J. Mater. Chem. C* **2018**, *6*, 7493.

5 (a) Jackson, N. E.; Savoie, B. M.; Kohlstedt, K. L.; de la Cruz, M. O.; Schatz, G. C.; Chen, L. X.; Ratner, M. A. *J. Am. Chem. Soc*. **2013**, *135*, 10475. (b) Raos, G.; Famulari, A.; Meille, S. V.; Gallazzi, M. C.; Allegra, G. *J. Phys. Chem. A* **2014**, *108*, 691. (c) Nielsen, C. B.; White, A. J. P.; McCulloch, I. *J. Org. Chem*. **2015**, *80*, 5045. (d) Gao, Y.; Deng, Y.; Tian, H.; Zhang, J.; Yan, D.; Geng, Y.; Wang, F. *Adv. Mater*. **2017**, *29*, 1606217. (e) Thorley, K. J.; McCulloch, I. *J. Mater. Chem. C* **2018**, *6*, 12413.

6 (a) Park, S. K.; Varghese, S.; Kim, J. H.; Yoon, S.-J.; Kwon, O. K.; An, B.-K.; Gierschner, J.; Park, S. J. *J. Am. Chem. Soc*. **2013**, *135*, 4757. (b) Dou, J.-H.; Yu, Z.-A.; Zhang, J.; Zheng, Y.-Q.; Yao, Z.-F.; Tu, Z.; Wang, X.; Huang, S.; Liu, C.; Sun, J.; Yi, Y.; Cao, X.; Gao, Y.; Wang, J.-Y.; Pei, J. *J. Am. Chem. Soc*. **2019**, *141*, 6561.

7 Kishi, R.; Ochi, S.; Izumi, S.; Makino, A.; Nagami, T.; Fujiyoshi, J.-y.; Matsushita, N.; Saito, M.; Nakano, M. *Chem. − Eur. J.* **2016**, *22*, 1493.

8 Wu, Q.; Ren, S.; Wang, M.; Qiao, X.; H, Li, X. Gao, X. Yang, D. Zhu, *Adv. Funct. Mater*., 2013, **23**, 2277–2284

9 Fuchibe, K.; Morikawa, T.; Shigeno, K.; Fujita, T.; Ichikawa, J. *Org. Lett*. **2015**, *17*, 1126.

10 Wang, X.-B. Woo, H-.K.; Huang, X.; Kappes, M. M.; Wang, L.-S. *Phys. Rev. Lett*. **2006**, *96*, 143002.

11 Anthopoulosa, T.D.; Anyfantis, G.C.; Papavassiliou, G. C.; de Leeuw, D. M. *Appl. Phys. Lett.* **2007**, *90*, 122105.

12 (a) de Leeuw, D. M.; Simenon, M. M. J.; Brown, A. R.; Einerhand, R. E. F. *Synth. Met.* **1997**, *87*, 53. (b) Anthopoulos, T. D.; Anyfantis, G. C.; Papavassiliou, G. C.; de Leeuw, D. M. *Appl. Phys. Lett.* **2007**, *90*, 122105-1-3. (c) Ie, Y.; Ueta, M.; Nitani, M.; Tohnai, N.; Miyata, M.; Tada, H.; Aso, Y. *Chem. Mater.* **2012**, *24*, 3285.

13 (a) Cheng, S.-S.; Huang, P.-Y.; Ramesh, M.; Chang, H.-C.; Chen, L.-M.; Yeh, C.-M.; Fung, C.-L.; Wu, M.-C.; Liu, C.-C.; Kim, C.; Lin, H.-C.; Chen, M.-C.; Chu, C.-W. *Adv. Funct. Mater*. **2014**, *24*, 2057. (b) Chen, X.; Zhang, G.; Luo, H.; Li, Y.; Liu, Z.; Zhang, D. *J. Mater. Chem. C* **2014**, *2*, 2869. (c) Xu, X.; Xiao, T.; Gu, X.; Yang, X.; Kershaw, S. V.; Zhao, N.; Xu, J.; Miao, Q. *Appl. Mater. Interfaces* **2015**, *7*, 28019. (d) Vegiraju, S.; Lin, C.-Y.; Priyanka, P.; Huang, D.-Y.; Luo, X.-L.; Tsai, H.-C.; Hong, S.-H.; Yeh, C.-J.; Lien, W.-C.; Wang, C.-L.; Tung, S.-H.; Liu, C.-L.; Chen, M.-C.; Facchetti, A. *Adv. Funct. Mater*. **2018**, *28*, 1801025.

14 Salzillo, T.; Camposa, A.; Mas-Torrent, M. *J. Mater. Chem. C* **2019**, *7*, 10257.

15 (a) Ribierre, J. C.; Fujihara, T.; Watanabe, S.; Matsumoto, M.; Muto, T.; Nakao, A.; Aoyama, T. *Adv. Mater*. **2010**, *22*, 1722. (b) Zhang, Y.; Kim, C.; Lin, J.; Nguyen, T.-Q. *Adv. Funct. Mater*. **2012**, *22*, 97. (c) Pfattner, R.; Pavlica, E.; Jaggi, M.; Liu, S.-X.; Decurtins, S.; Bratina, G.; Veciana, J.; Mas-Torrent, M.; Rovira, C. *J. Mater. Chem. C* ***2013***, 1, 3985. (d) Hwang, H.; Khim, D.; Yun, J.-M.; Jung, E.; Jang, S.-J.; Jang, Y. H.; Noh, Y.-Y.; Kim, D.-Y. *Adv. Funct. Mater*. **2015**, *25*, 1146. (e) Kang, M.; Hwang, H.; Park, W. T.; Khim, D.; Yeo, J. S.; Kim, Y.; Kim, Y. J.; Noh, Y. Y.; Kim, D. Y. *Appl. Mater. Interfaces* **2017**, ***9***, 2686.

16 Williams, J. H.; *Acc. Chem. Res*. **1993**, *26*, 593.

17 Gao, Y.; Deng, Y.; Tian, H.; Zhang, J.; Yan, D.; Geng, Y.; Wang, F. *Adv. Mater.* **2017**, *29*, 1606217.

18 Sakamoto, Y.; Komatsu, S.; Suzuki, T. *J. Am. Chem. Soc.* **2001**, *123*, 4643.

19 Li, Y.; Xue, L.; Li, H.; Li, Z.; Xu, B.; Wen, S.; Tian, W. *Macromolecules* **2009**, *42*, 4491.

20 He, Y.; Wu, W.; Zhao, G.; Liu, Y.; Li, Y. *Macromolecules* **2008**, *41*, 9760.

Chapter 4
Development of Anti-aromatic Framework Containing Heptafulvene Segment

4.1 Introduction

Increased interest has emerged in fully π-conjugated polycyclic hydrocarbons, which possess electronic properties desirable for potential applications as semiconducting materials in organic thin-film electronics.[1] While the majority of these systems are based on fused [4*n*+2] π-electron aromatic molecules such as pentacene, the utilization of a [4*n*] π-electron anti-aromatic system has emerged as a useful strategy to create new molecules with unusual electronic structures.[2] Since it is well known that the representative 8π- and 12π-electron frameworks pentalene and indacene (**ID**), respectively, are unstable due to the high anti-aromatic character, the incorporation of methylenecyclopentadiene (fulvene) segments into an acene system has become a rational molecular design to construct [4*n*] π molecules. Indeed, dibenzopentalene and indenofluorene (**IF**) derivatives have been intensively developed in recent years (Figure 4.1).[3] These fulvene units can accept an electron to form stable aromatic cyclopentadienide anions and, thus, polycyclic fully conjugated hydrocarbons containing five-membered rings have intrinsically electron-accepting characteristics.[4] An alternative approach to access anti-aromatic frameworks relies on the use of methylenecycloheptatriene (heptafulvene) segments to form tricyclic 16π-electron benzo[1,2:4,5]di[7]annulene (**BDA**), whereas pristine heptalene exhibits nonaromatic character due to its twisted non-planar geometry.[5] Although several polycyclic hydrocarbons containing a **BDA** framework have been synthesized,[6,7] the development of **BDA**-based anti-aromatic compounds is still limited due to the difficulty of (1) the molecular design to incorporate heptafulvene units into the π-conjugated systems and (2) the synthetic method for the construction of seven-membered rings. In contrast to the fulvene unit, the formation of cycloheptatrienyl cation by one-electron oxidation of heptafulvene leads to aromatic stabilization. Thus, the thin-film of **1** showed hole-transporting characteristics in OFET devices.[7,8] However, irrespective of these electronically complemental properties, fundamental studies to directly investigate the anti-aromatic character between the **ID** and **BDA** frameworks have not been carried out so far. Therefore, we sought to construct a novel π-conjugated polycyclic hydrocarbons by introducing multiple five-membered and seven-membered rings together in a conjugated molecule. Based on this strategy, we designed a new [4*n*] π system (**DIBDA)** containing both **ID** and **BDA** frameworks (Figure 4.1). The two outer benzene rings should induce an anti-aromatic character as the 16π-electron system based on **BDA** framework (**DIBDA-b**), however, 12π-electron system (**DIBDA-a**) exists in the resonance form. Recovery of benzenoid structure due to the pro-aromatic nature at the central benzene ring would lead to the appearance of open-shell electronic configuration (**DIBDA-c**). Furthermore, contribution of the polarized structure (**DIBDA-d**) seems to be existed, since **DIBDA** contains two azulene scaffolds. Herein, we describe the synthesis, structure, properties, and OFET characteristics of **DIBDA** to reveal the structure-property relationship of the novel [4*n*] π system.

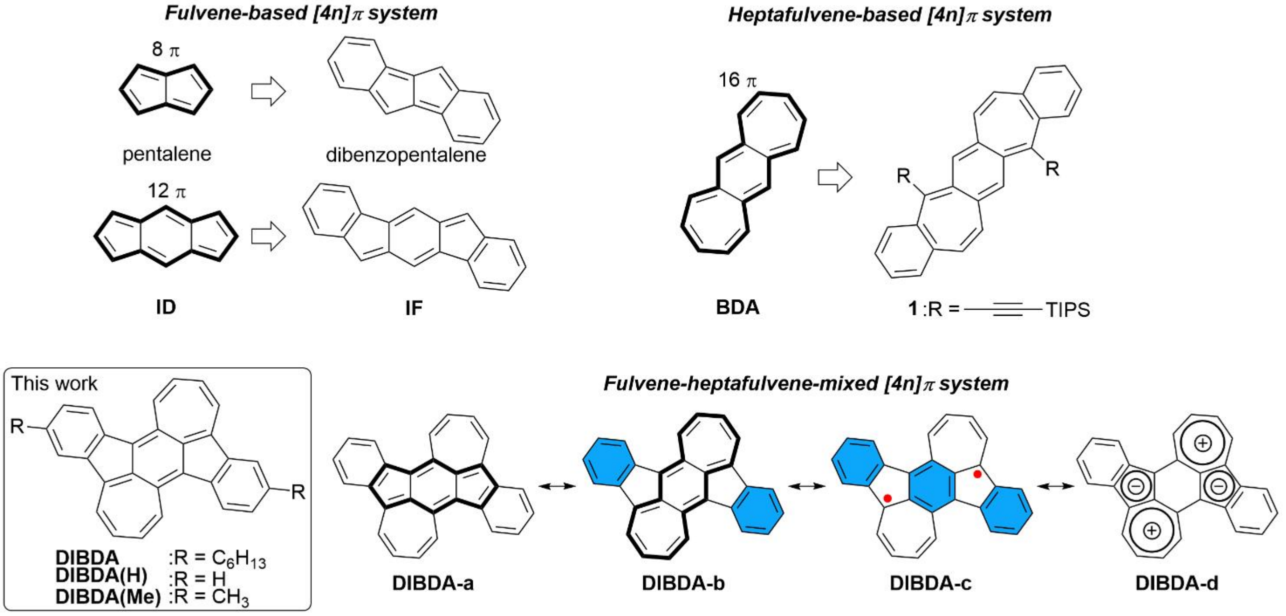

Figure 4.1. Chemical structures of representative anti-aromatic compounds and target compound **DIBDA**.

4.2 Synthesis and Characterization

We used an olefin metathesis reaction as a key step to construct the seven-membered ring framework. The synthetic route to **DIBDA** starting from compound **2** is shown in Scheme. 4.1. The Suzuki coupling reaction between **2** and allylboronic acid pinacol ester in the presence of [Pd(allyl)Cl]$_2$ afforded di-allylated compound **3**, which was reacted with allylmagnesium bromide to give the tetra-allylated compound **4**. The construction of seven-membered rings was achieved by olefin metathesis using the second generation Grubbs' catalyst to give key intermediate **5** in 95% yield.[9] We here report that compounds **4** and **5** were isolated as a mixture of diastereomers. Then, treatment of **5** with the Burgess reagent provided dehydrated compound **6**,[10] and subsequent oxidation with DDQ produced the target compound **DIBDA** in 50% yield. Note that the presence of the hexyl group is essential to impart enough solubility of **DIBDA** to enable characterization by NMR and other spectroscopic measurements. Detailed synthetic procedures and characterization data of the new compounds are summarized in the Experimental section. As shown in Figure S4.1, the ^{1}H NMR spectrum of **DIBDA** in CDCl$_3$ showed a downfield shift of the benzene protons by 0.41–0.62 ppm as compared to the indenofluorene derivative **IF(Me)-TA** (structure shown in Figure S4.1), indicating the increased contribution of aromatic character in the benzene ring for **DIBDA**. The proton signals in the seven-membered ring were observed in the upfield region between 5.95 and 7.29 ppm. Since the ^{1}H NMR signals for the seven-membered ring of the anti-aromatic **BDA** framework are reported to appear in a similar δ range of 4.88–6.30 ppm,[6] contribution of the anti-aromatic character in the seven-membered ring of **DIBDA** is expected.

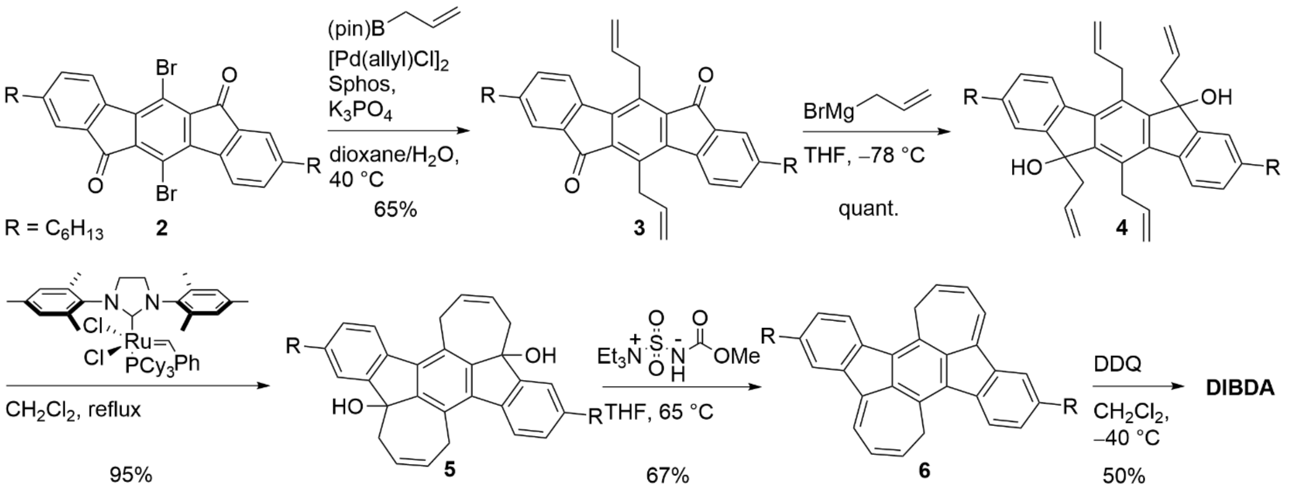

Scheme 4.1. Synthetic route of **DIBDA**.

TGA of **DIBDA** showed a 5% weight-loss temperature of 443 °C under a nitrogen atmosphere (Figure 4.2(a)). The DSC profile of **DIBDA** showed endothermic and exothermic peaks at 234 and 250 °C, respectively, during the first heating process (Figure 4.2(b)). On the other hand, no clear peaks were detected during the second heating process, and an insoluble black solid was observed after the DSC measurements. Given that only a slight weight loss was seen in TGA up to 443 °C, we considered that **DIBDA** melted at 234 °C, and intermolecular reactions occurred in the melting state to give unidentifiable insoluble products.

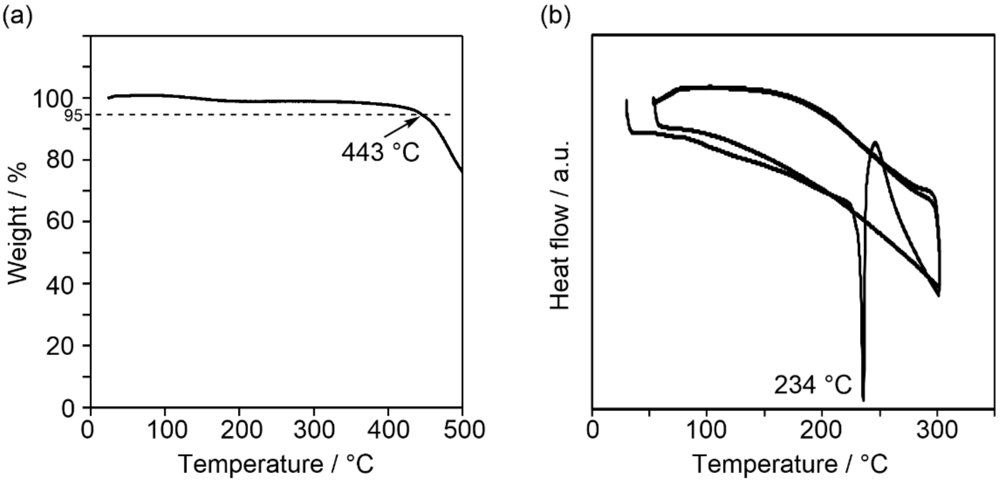

Figure 4.2. (a) TGA curves and (b) DSC curves of **DIBDA** at a heating rate of 10 °C min^{-1} in a N_2 atmosphere.

Since the indenofluorene derivatives include a *p*-quinodimethane core, it is known that these molecules show biradical character originating from the aromatization of the central benzene ring.[11] Thus, the singlet biradical characters (*y*) of **DIBDA(Me)** and **IF** were estimated using the occupation numbers of the spin-unrestricted Hartree–Fock natural orbitals. As a result, **DIBDA(Me)** displayed a moderate singlet biradical character ($y = 0.49$), which is larger than that of **IF** ($y = 0.30$). Since the calculated spin density for **DIBDA(Me)** shows the largest amplitude at the fused carbons between the five- and seven-membered rings and is distributed to the seven-membered ring

(Figure S4.2), the biradicaloid electronic structure is thought to be stabilized by the spin delocalization at the seven-membered rings.

4.3 Photophysical and Electrochemical Properties

The electrochemical behavior of **DIBDA** was investigated by CV and differential pulse voltammetry (DPV) measurements in CH_2Cl_2 containing 0.1 M $TBAPF_6$ as a supporting electrolyte. All potentials were calibrated against a ferrocene/ferrocenium (Fc/Fc^+) couple as the standard. As shown in Figure 4.3(a), the CV of **DIBDA** revealed three oxidation and two reduction processes, and the redox potentials were determined from DPV. From the first oxidation potential (E^{ox1}) and first reduction potential (E^{red1}) and the assumption that the energy level of Fc/Fc^+ is –4.8 eV below the vacuum level, the HOMO and LUMO energy levels (E_{HOMO} and E_{LUMO}) of **DIBDA** were estimated to be –4.69 and –3.46 eV, respectively. Based on these values, the HOMO-LUMO energy gap of **DIBDA** is calculated to be 1.23 eV. Interestingly, these E_{HOMO} and E_{LUMO} values are significantly different from those of **IF(Me)-TA** (E_{HOMO} = –5.84 eV and E_{LUMO} = –3.99 eV).[12] In order to understand the origin of this phenomenon, DFT calculations of **DIBDA(H)**, **IF**, and **BDA** at the B3LYP/6-311 +G(d,p) level were performed. As shown in Figure 4.4, the theoretically estimated E_{HOMO} and E_{LUMO} values of **DIBDA(H)** and **IF** qualitatively mimic the experimental values. Although the HOMO and LUMO orbitals of **DIBDA(H)** are delocalized over the π-conjugated backbones, both the E_{HOMO} and E_{LUMO} values of **DIBDA(H)** are between those of **BDA** and **IF** and closer to those of **BDA**. These results indicate that the electronic structure of the **DIBDA(H)** molecule is formed from a hybrid of those of **BDA** and **IF**, and that the contribution of the electronic character of **BDA** seems to be dominant.

To investigate the photophysical properties, a UV-vis-NIR absorption measurement of **DIBDA** in a CH_2Cl_2 solution was performed. As shown in Figure 4.3(b), the absorption spectrum of **DIBDA** includes three intense bands with absorption maxima (λ_{max}) at 279 (ε = 55000 M^{-1} cm^{-1}), 498 (36000 M^{-1} cm^{-1}), and 692 (26000 M^{-1} cm^{-1}) nm and weak bands at 866 and 997 nm. A TD-DFT calculation at the B3LYP/6-31G (d,p) level indicated that these intense bands were mainly assigned to HOMO–1 to LUMO+1, HOMO to LUMO+2, and HOMO to LUMO transitions, respectively (see the experimental section). The weak bands in the NIR region are assignable to the forbidden transition which is usually observed for anti-aromatic compounds.[13] Compared to the solution spectra, a new broad band was observed in the thin-films. This phenomenon is attributed to the intermolecular electronic interactions of π–π stacked backbones, which is favorable for carrier transport in thin-film devices (discussed later).

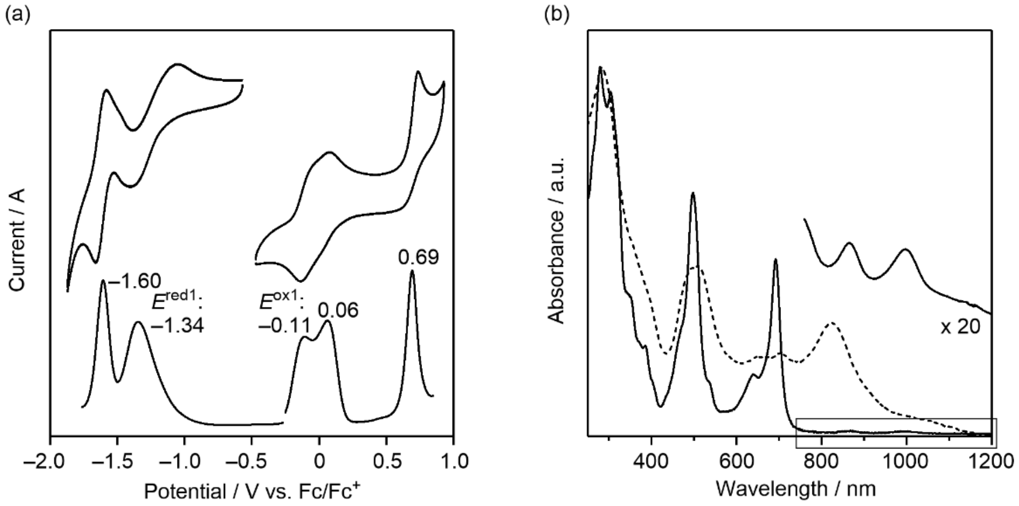

Figure 4.3. (a) CV (top) and DPV (bottom) of **DIBDA** in CH_2Cl_2 containing 0.1 M $TBAPF_6$. (b) UV-vis-NIR absorption spectra of DIBDA in CH_2Cl_2 (solid line) and thin-films (dashed line). The magnified spectrum in CH_2Cl_2 between 800 and 1200 nm is also shown.

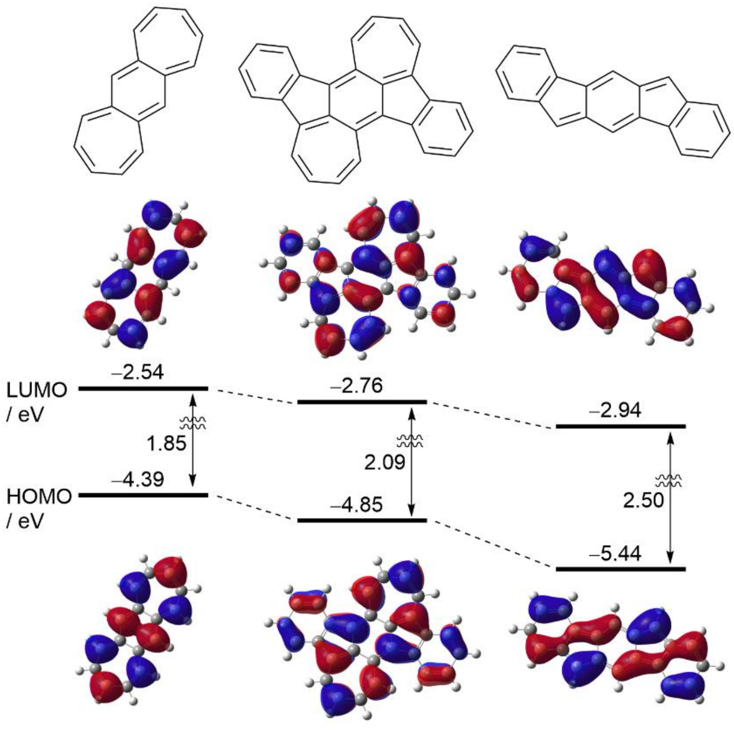

Figure 4.4. Energy levels and molecular orbitals of **BDA** (left), **DIBDA(H)** (center), and **IF** (right) calculated at B3LYP/6-311 + G(d,p) level.

The molecular structure of **DIBDA** was unambiguously determined using X-ray crystallographic analysis of crystals grown by the slow evaporation of hexane/$CHCl_3$ solutions. As shown in Figure 4.5(a), the π-conjugated framework of compound **DIBDA** holds a nearly planar structure: the deviations of carbon atoms constituting the **BDA** core from the mean plane of this core are less than 0.04 Å, and the dihedral angles between the mean planes of central **BDA** and the outer benzene rings are 4.9°, as shown in Figure 4.5(a). The structure of **1** was reported to show clear bond alternation in the *p*-quinodimethane core due to the increased contribution from resonance form **1a** (Figure S4.3), which in turn is attributed to the presence of the outer fused benzene rings.[7] On the other hand, the extent of the bond alternation for the **BDA** framework in **DIBDA** was rather small, with C–C bond lengths varying within the range of 1.37–1.44 Å (Figure 4.5(b)). To further assess the degree of bond alternation, we calculated the HOMA values based on the reported X-ray information. As shown in Figure S4.4, the HOMA value of the **BDA** framework in **1** was determined to be 0.31. In contrast, the HOMA value of the **BDA** framework in **DIBDA** was calculated to be as high as 0.81, supporting the small degree of bond alternation and resulting delocalized electronic structure. A similar trend was also observed for the anti-aromatic **ID** framework: the absence of fused benzene rings in compound **A** leads to an increase in the HOMA value (Figure S4.4). These results indicate that pristine anti-aromatic frameworks show large HOMA values; thus, the **BDA** framework in **2** is expected to show anti-aromatic character. Interestingly, this HOMA value is larger than that of the indenofluorene framework in **DIBDA** (0.56), indicating that the contribution of 16π (**BDA**) and $6\pi \times 2$ (two outer benzene rings) is larger than that of 20π (indenofluorene) in the electronic structure of **DIBDA**. To investigate the electronic contribution of the π electrons in **DIBDA**, we performed an electron localization function (ELF) estimation.[14] The ELF isosurface plot (Figure S4.5) showed that the π electron pairs are uniformly distributed over the entire molecule. This result clearly indicates that the π-conjugation is delocalized over the entire π conjugated framework in **DIBDA**, despite the different HOMA values of **BDA** and **IF** frameworks.

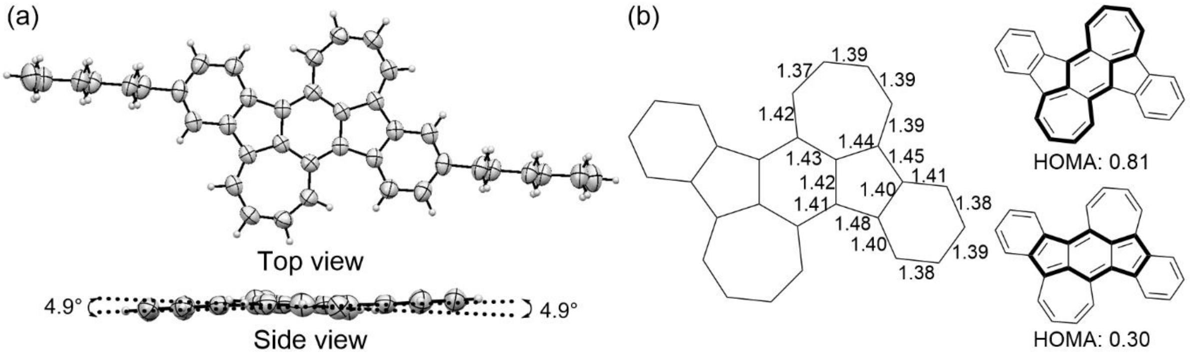

Figure 4.5. (a) ORTEP drawing of **DIBDA** for top view and side view. (b) bond lengths for the crystal structure (left) and HOMA values for **BDA** and **IF** frameworks.

Based on this molecular structure, we estimated the aromaticity of the π-conjugated framework of **DIBDA(H)** by the nucleus independent chemical shift (NICS). The results of the NICS(1.7)$_{\pi zz}$-*XY*-scans[15] are summarized in Figure 4.6. The NICS(1.7)$_{\pi zz}$ values of **DIBDA(H)**, calculated at the GIAO-B3LYP/6-311+G(d) level, are δ = +12.40, +6.19, –9.48, and –18.90 ppm for the rings A, B, C, and D, respectively. The positive values of rings A and B indicate that the **BDA** framework has an anti-aromatic character. On the other hand, the indenofluorene core composed of rings C and D in **DIBDA(H)** exhibits an aromatic character, which is in contrast with the result of pristine indenofluorene **IF**, in which the five-membered ring shows an anti-aromatic character.[16] Since framework **DIBDA(H)** contains both five- and seven-membered rings, this calculated aromatic character of the C ring is considered to result from increased electron density owing to electrical polarized structure (**DIBDA-d**) (Figure 4.1). This was confirmed by the calculation of the electrostatic potential of **DIBDA(H)**, which was similar to that calculated for benz[*a*]azulene, as shown in Supplementary Figure S4.6. These results are in agreement with the aforementioned findings based on the HOMA values, indicating the large electronic contribution of the **BDA** framework. To further support the anti-aromaticity of the **BDA** framework in **DIBDA**, we conducted anisotropy of the current-induced density (ACID) analysis.[17] Compound **DIBDA** showed continuous paratropic ring currents in the **BDA** framework (Figure 4.7). On the other hand, diatropic ring currents were seen in the C_5-C_6 frameworks. This result clearly indicates that **DIBDA** has local anti-aromaticity in the **BDA** framework and local aromaticity in the C_5-C_6 frameworks, consistent with the results of NICS calculation.

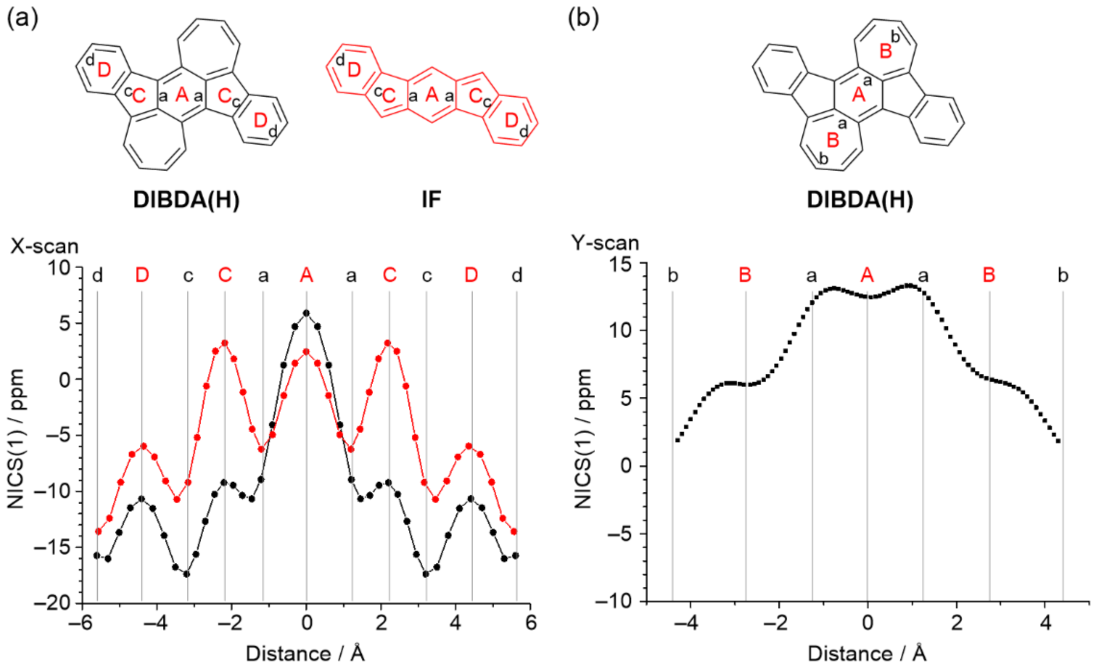

Figure 4.6. (a) NICS(1.7)πzz-X-scans for **DIBDA(H)** (black) and **IF** (red) and (b) NICS(1.7)πzz-Y-scans for **DIBDA(H)**.

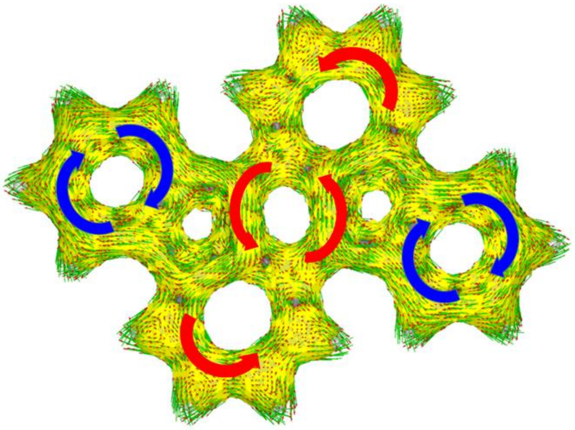

Figure 4.7. ACID-derived induced ring current map for **DIBDA**.

In the molecular packing diagram, **DIBDA** takes a herringbone π-stacked motif with minimum intermolecular π–π distances of 3.42 Å (Figure 4.8). On the basis of the calculation by the ADF program at the PW91/TZP level, the transfer integrals for hole transport (t_{HOMO}) and electron transport (t_{LUMO}) between adjoining molecules were estimated. **DIBDA** showed large t_{HOMO} and t_{LUMO} of 91.4 and 111.6 meV, respectively, between facial-stacked molecules, and, thus, the construction of charge-carrier transporting pathways is expected along the stacking direction.

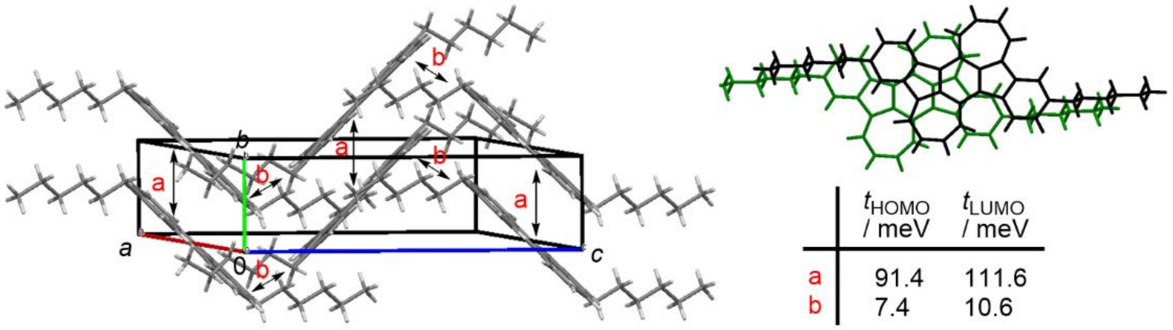

	t_{HOMO} / meV	t_{LUMO} / meV
a	91.4	111.6
b	7.4	10.6

Figure 4.8. Packing diagram and estimated transfer integrals of HOMOs and LUMOs for **DIBDA**.

4.4 Transistor Characteristics

Reflecting the high thermal stability of **DIBDA**, the thin-films for OFET measurements could be prepared by vacuum deposition onto HMDS-modified Si/SiO$_2$ substrates. The AFM image of this film exhibited interconnected micrometer-sized grains (Figure 4.9(a)). XRD of the thin-film showed clear diffractions, indicating the formation of crystalline structures in thin-films. According to the X-ray crystal structure (Figure 4.8), the peak at $2\theta = 5.2°$ can be indexed as a (001) diffraction peak with a *d* spacing of 17.0 Å, implying that the molecules are aligned with the crystal *c*-axis perpendicular to the SiO$_2$ surface. To evaluate the charge-transport characteristics of the thin-films, OFET devices with bottom-gate bottom-contact configuration were fabricated. As shown in Figure 4.9(c), this device showed hole-transporting characteristics with a field-effect hole mobility of 3.0×10^{-5} cm^2 V^{-1} s^{-1} with a current on/off ratio of 10^5. On the other hand, electron-transporting behavior was not observed for **DIBDA**. This p-type response is explained by the high-lying HOMO energy level of **DIBDA**. Importantly, taking the intrinsic electron-transporting behavior of the indenofluorene chromophore into consideration, embedding the **BDA** framework significantly influences the type of charge carriers. This trend is in good agreement with the estimated anti-aromaticity of the **BDA** framework.

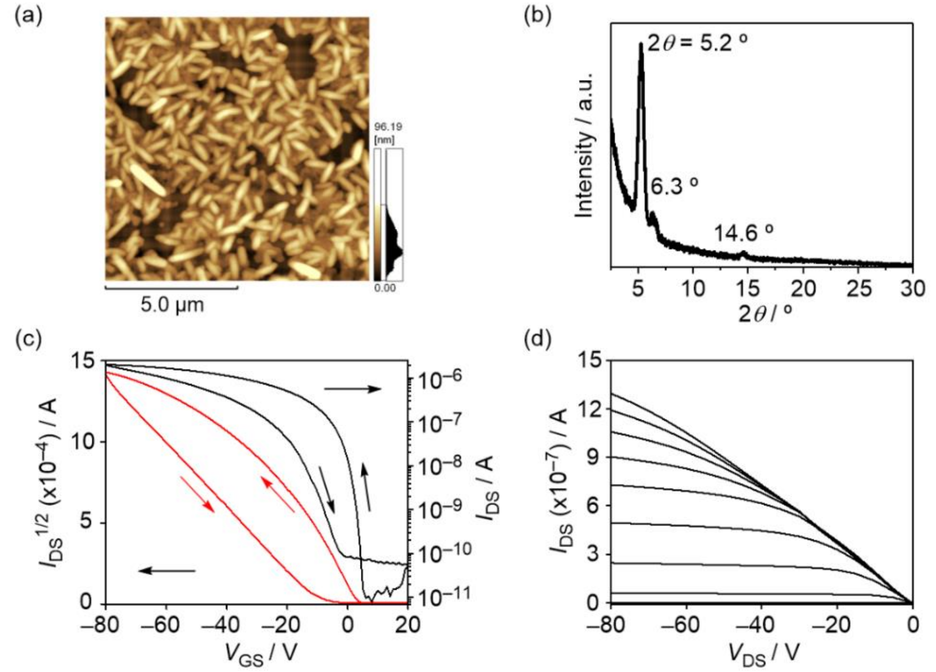

Figure 4.9. (a) AFM height image, (b) XRD data, OFET (c) transfer and (d) output characteristics of thin-film based on **DIBDA**. I_{DS} and V_{GS} denote source-drain current and gate voltage, respectively.

4.5 Conclusion

In conclusion, in order to directly investigate the anti-aromatic character between the **ID** and **BDA** frameworks, we successfully synthesized new polycyclic hydrocarbon **DIBDA**, which contains a fused dicyclohepta[*cd*,*ij*]-*s*-indacene framework in the molecule. Electrochemical and photophysical measurements revealed that **DIBDA** has a relatively high HOMO energy level and a narrow HOMO-LUMO energy gap, and these properties mainly come from the **BDA** framework. Investigation of the X-ray crystal structure and theoretical calculation indicates that the contribution of anti-aromatic character for the **BDA** framework is dominant in the molecule. These results clearly demonstrate that the unique character of **DIBDA** originated from the heptafulvene-based **BDA** framework, and we can conclude that the development of new anti-aromatic compounds possessing the **DCHI** or **BDA** frameworks will pave the way to the fundamental understanding of anti-aromaticity. Considering that **DIBDA** shows hole-transporting characteristics, fine-tuning of molecular design would aid the development of high-performance electronic materials. Further investigation on the development of such compounds to reveal the structure-property-semiconducting performance relationship is currently underway in our group.

4.6 Experimental Section

Supplementary Figures

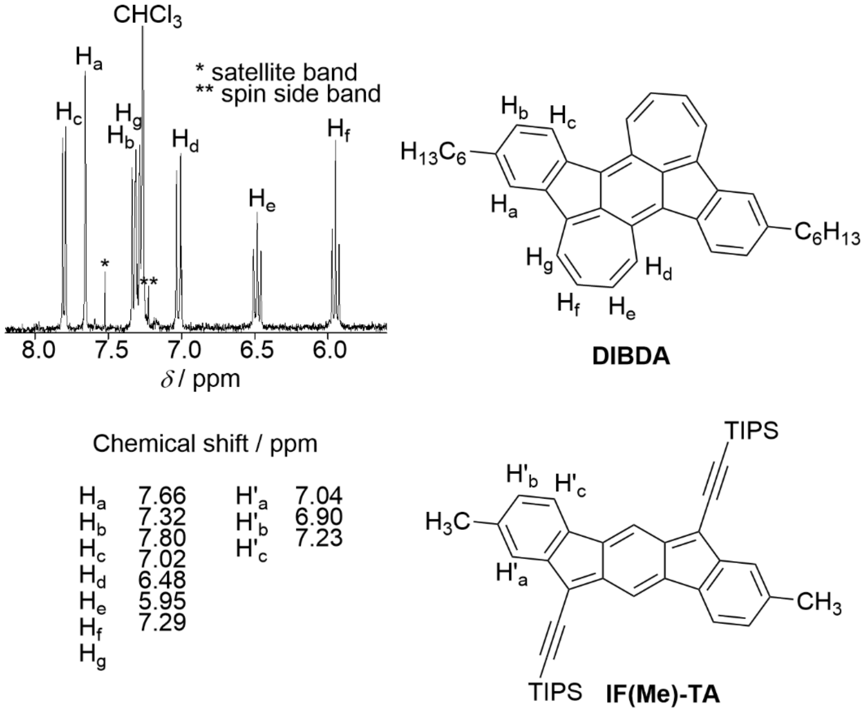

Chemical shift / ppm

H$_a$	7.66	H'$_a$	7.04
H$_b$	7.32	H'$_b$	6.90
H$_c$	7.80	H'$_c$	7.23
H$_d$	7.02		
H$_e$	6.48		
H$_f$	5.95		
H$_g$	7.29		

Figure S4.1. ^{1}H NMR spectrum of **DIBDA** in aromatic regions in CDCl$_3$. Chemical shifts of **IF(Me)-TA** were extracted from reference 12.

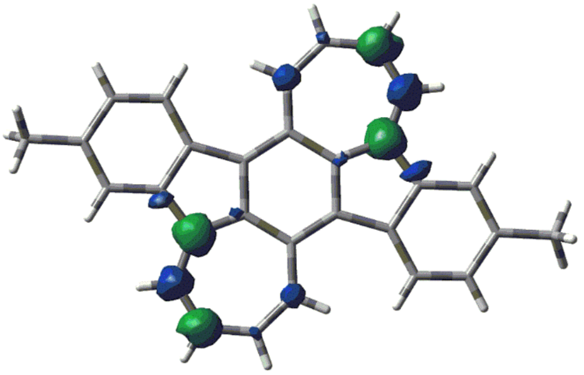

Figure S4.2. Spin density distribution of **DIBDA(Me)** calculated at the UB3LYP/6-31 G(d) level.

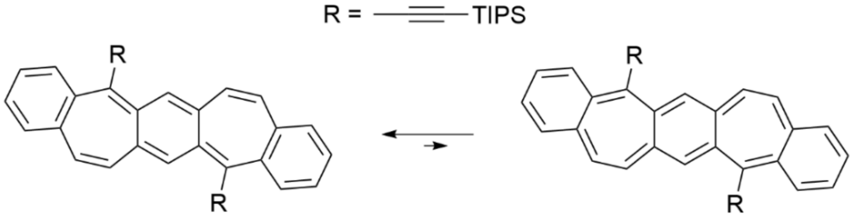

1a

1b

Figure S4.3. Resonance chemical structures of **1**.

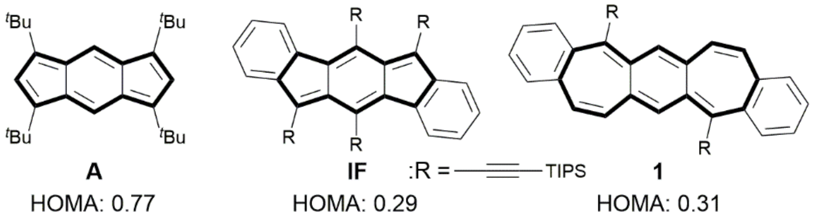

Figure S4.4. HOMA values for **A**, **IF**, and **1**. X-ray crystallographic data for **A**, **IF**, and **1** are obtained from references 18, 19, and 7, respectively**.**

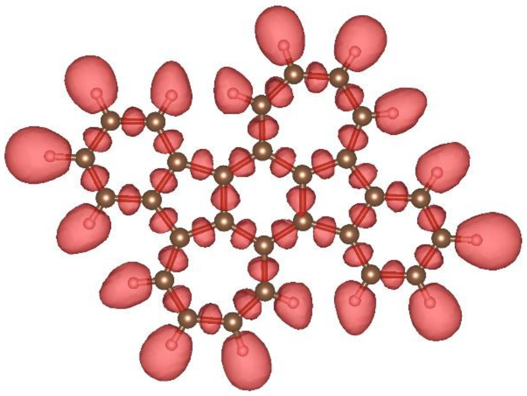

Figure S4.5. Isosurface plot of **DIBDA** at an isosurface level of 0.73.

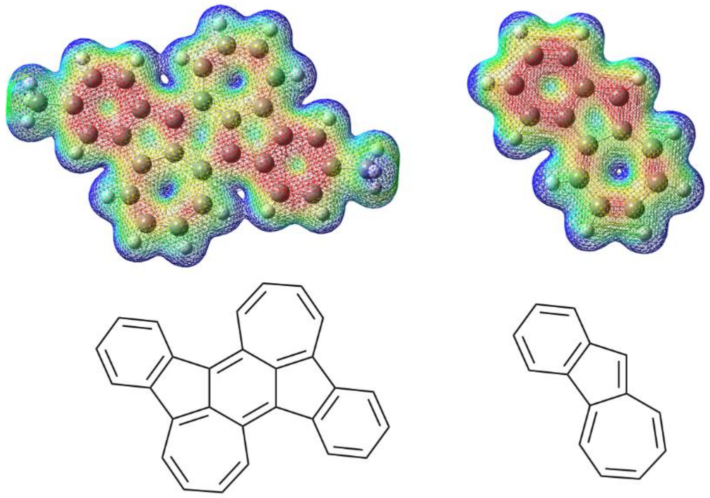

Figure S4.6. Electrostatic potentials of **DIBDA(H)** (left) and benz[*a*]azulene (right).

General Information

Column chromatography was performed on silica gel. KANTO Chemical silica gel 60N (40–50 μm). Thin-layer Chromatography (TLC) plates were visualized with UV light. Preparative GPC was performed on a Japan Analytical LC-918 equipped with JAI-GEL 1H/2H. ^{1}H and ^{13}C NMR spectra were recorded on a JEOL JNM-ECS400 or JEOL JNM-ECA600 spectrometer in $CDCl_3$ with TMS as an internal standard. Data are reported as follows: chemical shift in ppm (δ), multiplicity (s = singlet, d = doublet, t = triple, m = multiplet, br = broad), coupling constant (Hz), and integration. UV-vis-NIR spectra were recorded on a Shimadzu UV-3600 spectrophotometer. All spectra were obtained in spectrograde solvents. TGA and DSC were performed under nitrogen at a heating rate of 10 °C min^{-1} with a Shimadzu TGA-50 and a Shimadzu DSC-60, respectively. Cyclic voltammetry was carried out on a BAS CV-620C voltammetric analyzer using a platinum disk as the working electrode, platinum wire as the counter electrode, and Ag/AgNO$_3$ as the reference electrode at a scan rate of 100 mV s^{-1}. High-resolution mass spectrum (HRMS) was obtained atmospheric pressure chemical ionization (APCI) or electrospray ionization (ESI) methods using a Thermo scientific LTQ Orbitrap XL. Elemental analyses were performed on PerkinElmer LS-50B by the elemental analysis section of the Comprehensive Analysis Center (CAC) of ISIR, Osaka University. The surface structures of the deposited organic film were observed by atomic force microscopy (Shimadzu, SPM9600), and the film crystallinity was evaluated by an X-ray diffractometer (Rigaku, SmartLab). X-ray diffraction patterns were obtained using Bragg-Brentano geometry with CuKα radiation as an X-ray source with an acceleration voltage of 45 kV and a beam current of 200 mA. The scanning mode was set to 2θ–θ scans between 2º–30º with scanning steps of 0.01º.

X-Ray Information

The diffraction data were collected on a Rigaku XtaLAB P200 diffractometer with monochromated CuKα (λ = 1.54187 Å) radiation. The structures were determined by a direct method (SHELXT Version). The non-hydrogen atoms were anisotropically refined. CCDC-1816207 contains the supplementary crystallographic data for **DIBDA**. These data can be obtained free of charge from The Cambridge Crystallographic Data Centre via www.ccdc.cam.ac.uk/data_request/cif/.

Crystal Data for **DIBDA**: $C_{40}H_{40}$, M = 520.76, monoclinic, space group $P2_1/c$ (#14), a = 18.0409(11), b = 4.7749(3), c = 17.2744(10) Å, β = 104.994(6)°, V = 1437.41(16) Å^{-3}, D_{calc} = 1.203 g cm^{-3}, $F_{(000)}$ = 560.00, μ = 5.042 cm^{-1} (CuKα), Z = 2, R = 0.063, R_w = 0.1903 for all data.

OFET Device Fabrication and Evaluation

The field-effect electron mobility was measured using bottom-gate bottom-contact OFET devices. The p-doped silicon substrate functions as the gate electrode. A thermally grown silicon oxide (SiO_2) dielectric layer on the gate substrate has 300 nm thick and a capacitance (C_{i}) of 10.0 nF cm^{-2}. Interdigital source and drain electrodes were constructed with gold (30 nm) that were formed on the SiO2 layer. The channel width (W) and channel length (L) are 38 mm and 5 μm, respectively. The silicon oxide surface was first washed with toluene, acetone, purified water and 2-propanol. It was then activated by ozone treatment and pretreated with HMDS. The semiconductor layer was vacuum-deposited on the HMDS-modified Si/SiO_2 substrate at a rate of 0.1 Å s^{-1} under a pressure of 10^{-6} Pa to a thickness of 25 nm determined by a quartz crystal monitor. The characteristics of the OFETs were measured at room temperature under a pressure of 10^{-3} Pa by using a KEITHLEY 4200 semiconductor parameter analyzer. The hole mobility (μ_{h}) was calculated in the saturated region at the V_{DS} of –80 V by the following equation.

$$I_{\mathrm{DS}} = \frac{W}{2L} C_i \mu (V_{GS} - V_{th})^2$$

Current on/off ratio was determined from the I_{DS} at V_{GS}= 0 V (I_{off}) and V_{GS}= –80 V (I_{on})

Computational Details

All calculations were conducted using Gaussian 09 program. The geometry was optimized with the restricted Becke Hybrid (B3LYP) at 6-311+G(d,p) level. The time-dependent density functional theory (TD-DFT) calculations were conducted at the CAM-B3LYP/6-31G(d,p) level of theory. As shown below, optimized structure of **DIBDA** reproduces X-ray crystal structure. However, to directly correlate with HOMA values, nucleus-independent chemical shift (NICS) calculations and biradical character calculations were conducted by the geometry obtained by X-ray crystal structure analysis.

Side views of **DIBDA** for optimized chemical structure at B3LYP 6-311+G(d,p) level (left) and X-ray structure (right). For X-ray structure, alkyl groups were omitted for clarity.

The ELF was calculated with the DGrid 5.0 program,[20] and the isosurface was visualized using the VESTA program.

TD-DFT calculation

DIBDA(Me)

```
Excited State    1:         Singlet-A        2.03 eV    612 nm    f = 0.29    <S**2>=0.000
          HOMO–1 > LUMO+1                        0.23678
          HOMO > LUMO                            0.65657
Excited State    2:         Singlet-A        2.98 eV    416 nm    f = 0.14    <S**2>=0.000
          HOMO–3 > LUMO+1                        0.10330
          HOMO –2> LUMO                          0.27783
          HOMO–1> LUMO+1                         0.38943
          HOMO > LUMO                            0.19034
          HOMO > LUMO+2                          0.45979
Excited State    3:         Singlet-A        3.26 eV    381 nm    f = 0.34    <S**2>=0.000
          HOMO–1 > LUMO+1                        0.51868
          HOMO > LUMO                            0.14208
          HOMO> LUMO+2                           0.43182
```

Synthesis

Unless stated otherwise, all reagents were purchased from commercial sources and used without purification. Compound **s-1** was prepared by the reported procedure.[21]

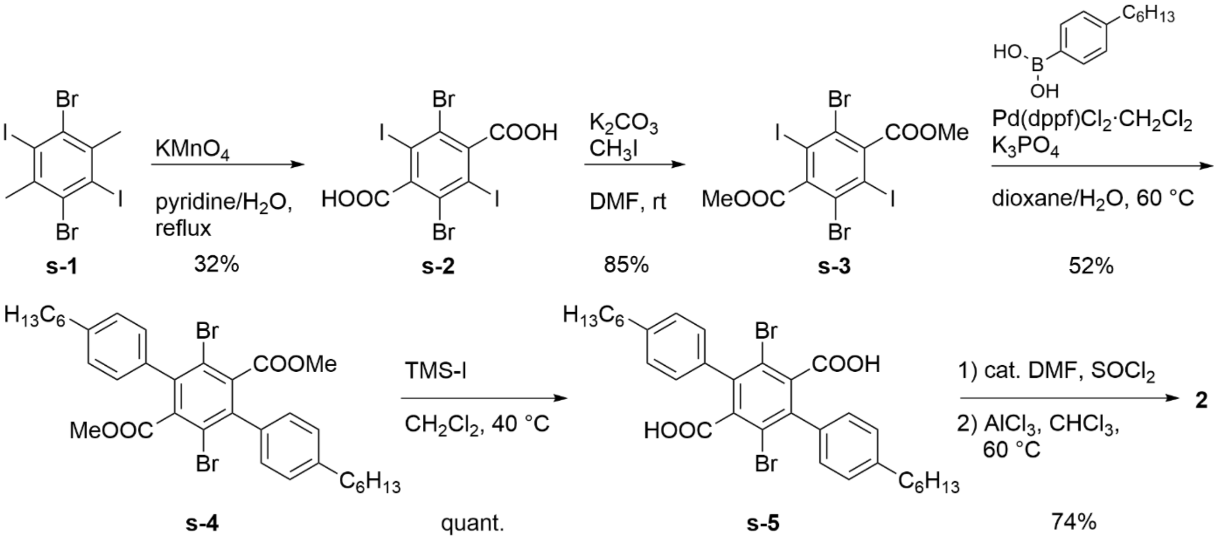

Scheme S4.1. Synthetic route of **2**.

Synthesis of 3: Compound **2** (200 mg, 0.329 mmol), allylboronic acid pinacol ester (0.240 mL, 1.32 mmol), allylpalladium(II) chloride dimer (24.0 mg, 0.0658 mmol), SPhos (108 mg, 0.263 mmol), and K_3PO_4 (350 mg, 1.65 mmol), 1,4-dioxance (7.0 mL) and water (1.9 mL) were added to a reaction vial. The vial was purged with N_2. After stirring for 4 h at 40 °C, water was poured into the reaction mixture. The resultant mixture was extracted with EtOAc and the combined organic layer was washed with brine. After drying with $MgSO_4$, the solvent was removed under reduced pressure and the residue was purified by column chromatography on silica gel (hexane : $CHCl_3$ = 2 : 1) to give **3** (113 mg, 65%) as a magenta solid. ^{1}H NMR (400 MHz, $CDCl_3$, TMS): δ 0.89 (t, J = 6.9 Hz, 6H), 1.27-1.38 (m, 12H), 1.56-1.65 (m, 4H), 2.66 (t, J = 7.6 Hz, 4H), 4.24 (d, J = 5.0 Hz, 4H), 5.08-5.13 (m, 4H), 6.05-6.16 (m, 2H), 7.30 (dd, J = 7.8, 1.8 Hz, 2H), 7.47 (d, J = 1.8 Hz, 2H), 7.57 (d, J = 7.8 Hz, 2H); ^{13}C NMR (150 MHz, $CDCl_3$): δ 14.1, 22.6, 28.9, 30.3, 31.1, 31.7, 35.6, 116.4, 123.6, 124.0, 133.9, 134.3, 134.9, 134.9, 136.1, 140.2, 144.1, 145.5; HRMS (*m*/*z*): $[M+H]^+$ calcd. for $C_{38}H_{43}O_2$, 531.3258; found, 531.3248.

Synthesis of 4: To a solution of **3** (190 mg, 0.358 mmol) in THF (23 mL), 1.0 M allylmagnesium bromide solution in Et_2O (0.788 mL, 0.788 mmol) was added at –78 °C. After stirring for 1 h at –78 °C, the reaction was quenched by pouring saturated NH_4Cl aqueous solution. The combined organic was extracted with EtOAc and washed with water. After drying over with $MgSO_4$, the solvent was removed under reduced pressure to give **4** (220 mg, quant.) as an orange solid. ^{1}H NMR (600 MHz, $CDCl_3$, TMS): δ 0.89 (t, J = 6.9 Hz, 6H), 1.27-1.38 (m, 12H), 1.59-1.68 (m, 4H), 2.19-2.23 (m, 2H), 2.61-2.69 (m, 4H), 2.92-3.07 (m, 4H), 3.95-4.01 (m, 1H), 4.08-4.14 (m, 1H), 4.30-4.36 (m, 1H), 4.42-4.47 (m, 1H), 4.65-4.77 (m, 4H), 4.86-4.96 (m, 2H), 5.06-5.16 (m, 4H), 6.14-6.23 (m, 2H), 7.11-7.15 (m, 2H), 7.32 (s, 2H), 7.54-7.60 (m, 2H); ^{13}C NMR (150 MHz, $CDCl_3$): δ 14.1, 22.6, 28.9, 29.0, 31.5, 31.8, 31.9, 35.9, 36.0, 43.7, 43.8, 82.7, 116.1, 116.2, 117.9, 118.0, 122.8, 123.0, 123.4, 123.5, 128.8, 128.9, 129.5, 129.9, 132.5, 132.6, 136.0, 136.2, 136.4, 138.7, 138.8, 142.1, 147.3, 147.5, 149.8; HRMS (*m/z*): $[M+Na]^+$ calcd. for $C_{44}H_{54}O_2Na$, 637.4016; found, 637.4014.

Synthesis of ***5***: Grubbs catalyst (22.4 mg, 0.0264 mmol) was added to a solution of **4** (203 mg, 0.330 mmol) in CH_2Cl_2 (8.0 mL), and the reaction was refluxed. After stirring for 2 h, the reaction mixture was filtrated through pad of celite. The solvent was removed under reduced pressure, and the residue was purified by column chromatography on silica gel ($CHCl_3$) to give **5** (175 mg, 95%) as a brown solid. ^1H NMR (600 MHz, $CDCl_3$, TMS): δ 0.89 (t, J = 6.5 Hz, 6H), 1.28-1.40 (m, 12H), 1.62-1.69 (m, 4H), 2.30-2.40 (m, 4H), 2.66 (t, J = 7.6 Hz, 4H), 2.98-3.04 (m, 2H), 4.09-4.21 (m, 4H), 5.68-5.74 (m, 2H), 5.89-6.00 (m, 2H), 7.16-7.19 (m, 2H), 7.34-7.37 (m, 2H), 7.73-7.81 (m, 2H); ^{13}C NMR (150 MHz, $CDCl_3$): δ 14.1, 22.6, 28.4, 28.9, 29.1, 31.5, 31.7, 35.9, 38.8, 38.9, 80.9, 81.0, 123.0, 123.1, 123.2, 125.5, 125.9, 126.1, 126.4, 129.1, 131.1, 131.4, 135.0, 135.1, 136.7, 136.8, 142.4, 142.5, 148.5, 148.9, 150.8, 150.9; HRMS (*m/z*): $[M+Na]^+$ calcd. for $C_{40}H_{46}O_2Na$, 581.3390; found, 581.3392.

Synthesis of ***6***: Burgess reagent (180 mg, 0.754 mmol) was added to a solution of **5** (175 mg, 0.314 mmol) in THF (7.0 mL). After stirring for 1 h at 65 °C, the reaction was quenched by pouring water. The combined organic was extracted with EtOAc and washed with water. After drying over with $MgSO_4$, the solvent was removed under reduced pressure and the residue was purified by column chromatography on silica gel (hexane : $CHCl_3$ = 1 : 1) to give **6** (110 mg, 67%) as a brown solid. ^1H NMR (400 MHz, $CDCl_3$, TMS): δ 0.90 (t, J = 6.9 Hz, 6H), 1.28-1.42 (m, 12H), 1.64-1.74 (m, 4H), 2.70 (t, J = 7.3 Hz, 4H), 3.76 (d, J = 7.3 Hz, 4H), 5.95-6.04 (m, 2H), 6.46-6.53 (m, 2H), 7.14-7.19 (m, 4H), 7.59 (d, J = 1.4 Hz, 2H), 7.98 (d, J = 7.8 Hz, 2H); ^{13}C NMR (150 MHz, $CDCl_3$): δ 14.1, 22.7, 29.0, 29.4, 31.6, 31.8, 36.1, 120.1, 122.3, 122.8, 122.9, 123.8, 127.4, 127.9, 133.3, 137.3, 140.9, 141.2, 141.3, 141.9; HRMS (*m/z*): $[M+H]^+$ calcd. for $C_{40}H_{43}$, 523.3359; found, 523.3353.

Synthesis of ***DIBDA****:* To a solution of **6** (22 mg, 0.042 mmol) in CH_2Cl_2 (3.2 mL), a solution of DDQ (9.6 mg, 0.042 mmol) in CH_2Cl_2 (1.0 mL) was added slowly at –40 °C. After stirring for 20 min, the reaction was allowed to warm to ambient temperature. The solvent was removed under reduced pressure and the residue was washed with acetone to give **DIBDA** (11 mg, 50%) as a dark green solid. Recrystallization from hexane/$CHCl_3$ gave a pure compound. mp: 233-235 °C; ^1H NMR (400 MHz, $CDCl_3$, TMS): δ 0.89 (t, J = 6.9 Hz, 6H), 1.27-1.38 (m, 12H), 1.64-1.72 (m, 4H), 2.75 (t, J = 7.6 Hz, 4H), 5.92-5.97 (m, 2H), 6.46-6.51 (m, 2H), 7.02 (d, J = 11.5 Hz, 2H), 7.28-7.34 (m, 4H), 7.66 (s, 2H), 7.80 (d, J = 8.7 Hz, 2H); ^{13}C NMR (175 MHz, $CDCl_3$): δ 14.2, 22.6, 29.1, 31.8, 31.9, 36.2, 119.5, 120.7, 123.6, 126.0, 128.8, 129.0, 133.0, 134.4, 134.6, 136.5, 138.0, 140.4, 149.1, 150.6; UV/vis (CH_2Cl_2): λ_{max} (ε [$M^{-1}cm^{-1}$]) = 279 (55000), 304 (51000), 498 (36000), 692 (26000); HRMS (*m/z*): $[M+H]^+$ calcd. for $C_{40}H_{41}$, 521.3203; found, 521.3196.

Synthesis of ***s-2***: Potassium permanganate (42.6 g, 270 mmol) was added in six portions to a solution of compound **s-1** (6.96 g, 13.5 mmol) in pyridine (242 mL) and water (71 mL), and the mixture was stirred for overnight at reflux condition. The reaction mixture was passed through pad of celite under hot condition to remove residue of potassium permanganate. The filtrate was washed with EtOAc for two times, and the aqueous layer was acidified by 10%

hydrochloric acid. The precipitate in the aqueous layer was extracted with EtOAc. After drying with $MgSO_4$, the solvent was removed under reduced pressure. Then potassium hydroxide (4.04 g, 72.0 mmol) was added to the suspension of obtained solid in water (216 mL), and the mixture was allowed to warm to 90 °C. To this solution, potassium permanganate (13.0 g, 82.3 mmol) was added, and this reaction mixture was stirred for 6 h. After completion of the reaction, methanol was added to the reaction mixture at room temperature in order to quench the unreacted potassium permanganate. Then, this mixture was passed through pad of celite under hot condition. The filtrate was acidified by 2N hydrochloric acid, and the precipitate was extracted with EtOAc. After drying with $MgSO_4$, the solvent was removed under reduced pressure to give **s-2** (2.51 g, 32%) as a white solid. ^1H NMR (400 MHz, DMSO-d_6): δ 14.30 (br, 2H); ^{13}C NMR (100 MHz, DMSO-d_6): δ 103.5, 126.2, 146.5, 168.6. This compound was used for next step without further purification.

*Synthesis of **s-3***: Compound **s-2** (2.49 g, 4.33 mmol), potassium carbonate (2.39 g, 17.3 mmol) in DMF (10.4 mL) was stirred for 10 min at room temperature. Then, iodomethane (1.08 mL, 17.3 mmol) was added to this mixture. After stirring for 1 h at 35 °C, water was poured into the reaction mixture. The resulting mixture was extracted with EtOAc. The organic layer was washed with water and dried over $MgSO_4$. The solvent was removed under vacuum condition to give **s-3** (2.21 g, 85%) as a white solid. ^1H NMR (400 MHz, $CDCl_3$, TMS): δ 3.99 (s, 6H); ^{13}C NMR (150 MHz, $CDCl_3$): δ 54.0, 101.4, 126.7, 145.1, 166.9; HRMS (m/z): $[M+H]^+$ calcd. for $C_{10}H_7Br_2I_2O_4$, 604.6775; found, 604.6760.

*Synthesis of **s-4***: Compound **s-3** (2.21 g, 3.66 mmol), 4-hexylphenylboronic acid (2.26 g, 11.0 mmol), $Pd(dppf)Cl_2{\cdot}CH_2Cl_2$ (59.8 mg, 0.0732 mmol), and K_3PO_4 (3.11 g, 14.6 mmol), 1,4-dioxance (51 mL), and water (14 mL) were added to a round-bottom flask. This flask was purged with N_2. After stirring for 16 h at 60 °C, the mixture was extracted with EtOAc, and the organic layer was washed with water. After drying with $MgSO_4$, the solvent was removed under reduced pressure. The residue was purified by column chromatography on silica gel ($CHCl_3$), followed by purification with preparative GPC ($CHCl_3$) to give **s-4** (1.28 g, 52%) as a white solid. ^1H NMR (400 MHz, $CDCl_3$, TMS): δ 0.89 (t, J = 7.0 Hz, 6H), 1.27-1.38 (m, 12H), 1.60-1.70 (m, 4H), 2.65 (t, J = 7.8 Hz, 4H), 3.53 (s, 6H), 7.17-7.25 (m, 8H); ^{13}C NMR (150 MHz, $CDCl_3$): δ 14.4, 23.0, 29.3, 31.5, 32.0, 36.1, 52.8, 120.2, 128.5, 129.5, 135.0, 139.2, 141.5, 143.8, 167.0; HRMS (m/z): $[M+Na]^+$ calcd. for $C_{34}H_{40}Br_2O_4Na$, 695.1165; found, 695.1168.

*Synthesis of **s-5***: To a solution of **s-4** (1.28 g, 1.90 mmol) in CH_2Cl_2 (14.4 mL), trimethylsilyl iodide (1.55 mL, 11.4 mmol) was added. After stirring for overnight at 40 °C, water was poured into the mixture at room temperature. The resultant mixture was extracted with EtOAc, and the organic layer was washed with water. After drying with $MgSO_4$, the solvent was removed under reduced pressure to give **s-5** (1.22 g, quant.) as a white solid. ^1H NMR (400 MHz, DMSO-d_6, TMS): δ 0.89 (t, J = 6.8 Hz, 6H), 1.26-1.38 (m, 12H), 1.56-1.66 (m, 4H), 2.62 (t, J = 7.6 Hz, 4H), 7.19 (d, J = 8.4 Hz, 4H), 7.29 (d, J = 8.4 Hz, 4H), 13.49 (br, 2H). This compound was used for next step without further purification.

*Synthesis of **2***: Compound **s-5** (1.22 g, 1.89 mmol) was placed in a round-bottom flask. Thionyl chloride (23 mL) and DMF as a catalyst was added to the flask, and the reaction mixture was refluxed for 2 h. Then, thionyl chloride and DMF were removed under reduced pressure. The residue was resolved in $CHCl_3$ (68 mL), and aluminum chloride (2.52 g, 18.9 mmol) was added to the solution. After stirring for 5 h at 60 °C, 10% hydrochloric acid was slowly poured into the reaction mixture at 0 °C. The resultant mixture was extracted with $CHCl_3$, and the organic layer was washed with water and $NaHCO_3$. After drying with $MgSO_4$, the solvent was removed under reduced pressure, and the residue was washed with acetone to give **2** (850 mg, 74%) as a magenta solid; ^{1}H NMR (600 MHz, $CDCl_3$, TMS): δ 0.89 (t, J = 6.3 Hz, 6H), 1.27-1.38 (m, 12H), 1.60-1.67 (m, 4H), 2.66 (t, J = 8.1 Hz, 4H), 7.38 (d, J = 7.2 Hz, 2H), 7.54 (s, 2H), 8.49 (d, J = 7.2 Hz, 2H); ^{13}C NMR (150 MHz, $CDCl_3$): δ 14.1, 22.6, 28.8, 31.0, 31.6, 35.7, 114.4, 124.3, 124.7, 134.3, 135.1, 137.1, 138.8, 145.8, 146.7, 190.0; HRMS (m/z): $[M+H]^+$ calcd. for $C_{32}H_{33}Br_2O_2$, 609.0822; found, 609.0818; analysis (calcd., found for $C_{32}H_{32}Br_2O_2$): C (63.17, 63.06), H (5.30, 5.43).

4.6 References

1 (a) Bendikov, M.; Wudl, F.; Perepichka, D. F. *Chem. Rev.* **2004**, *104*, 4891. (b) Anthony, J. E. *Angew., Chem. Int. Ed.* **2008**, *47*, 452. (c) Li, J.; Zhang, Q. *Synlett.* **2013**, *24*, 686. (d) Ye, Q.; Chi, C. *Chem. Mater.* **2014**, *26*, 4046.

2 (a) Randić, M. *Chem. Rev.* **2003**, *103*, 3449. (b) Kertesz, M.; Choi, C. H.; Yang, S. *Chem. Rev.* **2005**, **105**, 3448. (c) Hopf, H. *Angew., Chem. Int. Ed.* **2013**, *52*, 12224. (d) Breslow, R. *Chem. Rec.* **2014**, *14*, 1174.

3 (a) Tobe, Y. Chem. Rec. **2015**, *15*, 86. (b) Frederickson, C. K.; Rose, B. D.; Haley, M. M. *Acc. Chem. Res.* **2017**, *50*, 977.

4 Chase, D. T.; Fix, A. G.; Kang, S. J.; Rose, B. D.; Weber, C. D.; Zhong, Y.; Zakharov, L. N.; Lonergan, M. C.; Nuckolls, C.; Haley, M. M. *J. Am. Chem. Soc.* **2012**, *134*, 10349.

5 (a) Oth, J. F. M.; Müllen, K.; Königshofen, H.; Wassen, J.; Vogel, E. *Helv. Chim. Acta.* **1974**, *57*, 2387. (b) Konishi, A.; Horii, K.; Shiomi, D.; Sato, K.; Takui, T.; Yasuda, M. *J. Am. Chem. Soc.* **2017**, *141*, 10165.

6 Sugihara, Y.; Saito, J.; Murata, I. *Angew., Chem. Int. Ed.* **1991**, *30*, 1174.

7 Yang, X.; Liu, D.; Miao, Q. *Angew., Chem. Int. Ed.* **2014**, *53*, 6786.

8 (a) Xu, X.; Xiao, T.; Gu, X.; Yang, X.; Kershaw, S. V.; Zhao, N.; Xu, J.; Miao, Q. *ACS Appl. Mater. Interfaces* **2015**, *7*, 28019. (b) Yang, X.; Shi, X.; Aratani, N.; Goncalves, T. P.; Huang, K.-W.; Yamada, H.; Chi, C.; Miao, Q. *Chem. Sci.* **2016**, *7*, 6176.

9 Scholl, M.; Ding, S.; Lee, C. W.; Grubbs, R. H. *Org. Lett.* **1999**, *1*, 953.

10 Burgess, E.; Penton, H. R. Jr.; Taylor, E. A. *J. Org. Chem.* **1973**, *38*, 26.

11 Ito, S.; Minami, T.; Nakano, M. *J. Phys. Chem. C* **2012**, *116*, 19729.

12 Chase, D. T.; Fix, A. G.; Rose, B. D.; Weber, C. D.; Nobusue, S.; Stockwell, C. E.; Zakharov, L. N.; Lonergan, M. C.; Haley, M. M. *Angew. Chem., Int. Ed.* **2011**, *50*, 11103.

13 Ito, T.; Hayashi, Y.; Shimizu, S.; Shin, J.-Y.; Kobayashi, N.; Shinokubo, H. *Angew. Chem., Int. Ed.* **2012**, *51*, 8542.

14 Poater, J.; Duran, M.; Solà, M.; Bernard Silvi, B. *Chem. Rev.* **2014**, *105*, 3911.

15 Gershoni-Poranne, R.; Stanger, A. *Chem. − Eur. J.* **2014**, *20*, 5673.

16 Frederickson, C. K.; Zakharov, L. N.; Haley, M. M. *J. Am. Chem. Soc.* **2016**, *138*, 16827.

17 Herges, R.; Geuenich, D. *J. Phys. Chem. A* **2001**, *105*, 3214.

18 Dunitz, J. D.; Krüger, C.; Irngartinger, H.; Maverick, E. F.; Wang, Y.; Nixdorf, M. *Angew. Chem., Int. Ed.* **1988**, *27*, 387.

19 Chase, D. T.; Rose, B. D.; McClintock, S. P.; Zakharov, L. N.; Haley, M. M. *Angew., Chem. Int. Ed.* **2011**, *50*, 1127.

20 Kohout, M. DGrid, version 5.0; Max Planck Institute for Chemical Physics of Solids: Dresden, Germany, 2017.

21 Rose, B. D.; Santa Maria, P. J.; Fix, A. G.; Vonnegut, C. L.; Zakharov, L. N.; Parkin, S. R.; Haley, M. M. *Beilstein J. Org. Chem*. **2014**, *10*, 2122.

Conclusion

In this thesis, the design, synthesis, properties, and semiconducting characteristics of novel quinoidal and anti-aromatic compounds were investigated for elucidation of the structure−property relationships in order to allow these compounds to become candidates for advanced materials in organic electronics. The major conclusions in each chapter of this thesis are summarized as follows.

In chapter 1, the synthesis of benzo-annulated quinoidal oligothiophenes was achieved. The presence of benzo-annulation increased the molecular stability, leading to the isolation of quinoidal oligothiophene 6-mer (**BTQ-6**) as an ambipolar semiconducting material applicable for OFET device. Theoretical and experimental investigation indicated that benzo-annulated quinoidal terthiophenes have large contribution of closed-shell electronic structure. As a result, the conformation of these molecules was stabilized in the solution. The VT-FET measurements suggested that the decreased contribution of biradical character suppressed hole injection at $V_{GS} = 0$, leading to high on/off current ratio in OFET devices.

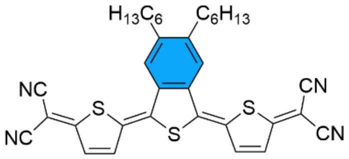

BTQ

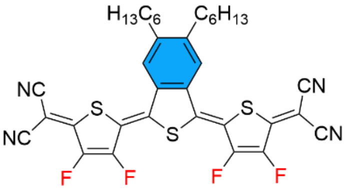

BTQ-F

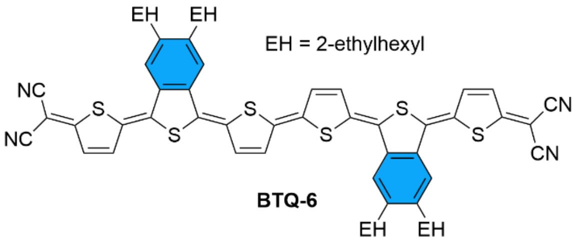

BTQ-6

In chapter 2, the synthesis of fully benzo-annulated quinoidal terthiophene derivatives (**B3TQ-Bu** and **B3TQ-EH**) was accomplished using retro Diels-Alder reaction. Thermal analyses indicated that the introduction of benzo-annulation led to high thermal stability. Theoretical calculation indicated that **B3TQ** core has no open-shell electronic configuration, and experimental measurements showed large band gap of the molecules. OPV device based on a donor polymer and **B3TQ-EH** as an acceptor showed PCE of 1.39%.

B3TQ-Bu (R = C_4H_9)
B3TQ-EH (R = 2-ethylhexyl)

In chapter 3, the synthesis of new quinoidal oligothiophenes having fluorine atoms (**FQT**, **FTQ**, **FTQ-TT**) was achieved. VT-NMR measurements and NBO analyses demonstrated that fluorine substitution to quinoidal oligothiophenes fixed *trans*-conformation due to the noncovalent intramolecular S-F interaction, leading to the high crystallinity of these materials in the solid states. From electrochemical measurements, it was confirmed that fluorine substitution increased electron-accepting characteristics. Owing to the enhanced stability of reduced species of these molecules, **FTQ** and **FTQ-TT** showed excellent stability against air as n-type semiconductors in OFET devices. Also, the blend films of **FTQ** and TIPS-pentacene showed ambipolar characteristics due to the formation of the co-crystal. This result is rationalized by the change of the charge distribution symmetry on the oligothiophene core based on the fluorine substitution.

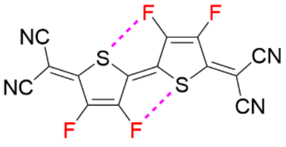

FQT

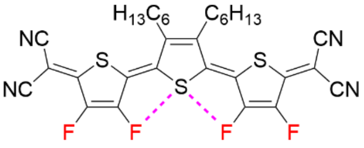

FTQ

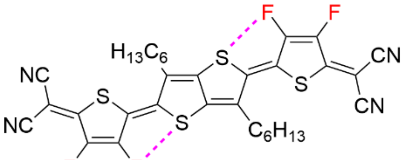

FTQ-TT

In chapter 4, the synthesis of **DIBDA** containing **DBA** scaffold was achieved by using olefin metathesis as a key reaction. From the bond length obtained by single-crystal X-ray analysis, large contribution of **DIBDA-b** conjugated system is suggested. Theoretical studies indicated that **DIBDA** has paratropic ring current on the **BDA** framework. The high thermal stability of **DIBDA** allow device fabrication by vacuum deposition, and the OFET device showed hole transporting characteristic due to the high HOMO energy level of the molecule. This result demonstrated that local antiaromaticity on **BDA** framework has large effect on the semiconducting characteristics.

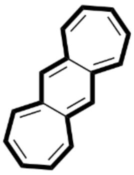

BDA

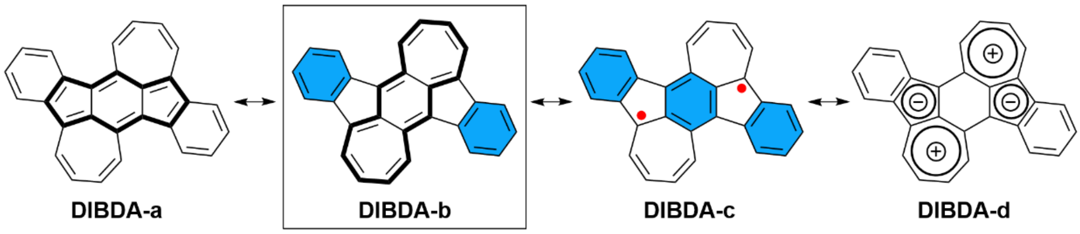

DIBDA-a **DIBDA-b** **DIBDA-c** **DIBDA-d**

In this work, I developed quinoidal and anti-aromatic compounds where the electronic structures were modified for application to organic electronics. First of all, the synthetic route of these compounds bearing benzo-annulation structures for controlling the biradical character (*y*) were established. Then, the relationships of structure, properties, and semiconducting characteristics were investigated by using several experimental measurements and theoretical calculations. The systematic studies of quinoidal oligothiophenes having benzo-annulation structures showed that subtle difference of the values of biradical character has large effects on the electronic properties of the materials in the solid states. Measurements of semiconducting characteristics based on the thin films of the materials implied that the biradical character of quinoidal molecules has an influence on the carrier generation process. On the other hand, I achieved the synthesis of a new anti-aromatic [4n] π scaffold containing seven-membered rings and revealed the potential application to p-type materials in organic electronics, owing to the considerably enhanced HOMO energy level. This thesis provides important information for development of novel π-conjugated compounds as organic electronic materials.

List of Publications

(1) Oligothiophene quinoids containing a benzo[*c*]thiophene unit for the stabilization of the quinoidal electronic structure
K. Yamamoto, Y. Ie, M. Nitani, N. Tohnai, F. Kakiuchi, K. Zhang, W. Pisula, K. Asadi, P. W. M. Blom, Y. Aso
Journal of Materials Chemistry C, Vol. 6, 7493–7500 (2018).

(2) Antiaromatic character of cycloheptatriene-bis-annelated indenofluorene framework mainly originated from heptafulvene segment
K. Yamamoto, Y. Ie, N. Tohnai, F. Kakiuchi, Y. Aso
Scientific Reports, Vol. 8, 17663 (2018).

(3) Electron-accepting π-Conjugated Systems Based on Cyclic Imide and Cyano-substituted Benzothiadiazole for Non-fullerene Organic Photovoltaics
K. Yamamoto, S. Kato, H. Zajaczkowska, T. Marszalek, P. W. M. Blom, Y. Ie
Journal of Materials Chemistry C, in press.

(4) Quinoidal Oligothiophenes Having Full Benzene Annelation: Synthesis, Properties, Structures, and Acceptor Application in Organic Photovoltaics
K. Yamamoto, S. Jinnai, T. Takehara, T. Suzuki, Y. Ie
Organic Letters, Vol. 22, 547–551 (2020).

List of Supplementary Publications

(1) Regioselective Nucleophilic Functionalization of Antiaromatic Nickel(II) Norcorroles
R. Nozawa, K. Yamamoto, J.-Y. Shin, S. Hiroto, H. Shinokubo
Angewandte Chemie International Edition, Vol. 54, 8454–8457 (2015).

(2) Ni^{II} tetrahydronorcorroles: antiaromatic porphyrinoids with saturated pyrrole units
R. Nozawa, K. Yamamoto, I. Hisaki, J.-Y. Shin, H. Shinokubo
Chemical Communications, Vol. 52, 7106–7109 (2016).

(3) A Thiazole-fused Antiaromatic Compound Containing an *s*-Indacene Chromophore with a High Electron Affinity
Y. Ie, C, Sato, K. Yamamoto, M, Nitani, Y. Aso
Chemistry Letters, Vol. 47, 1534–1537 (2019).

Acknowledgements

Foremost, I am deeply grateful to Professor Yutaka Ie for the invaluable discussions, continuous guidance, suggestion, and encouragement of my Ph.D study and research.

I would like to offer my special thanks to Professor Yoshio Aso for the invaluable discussions, guidance, and suggestion of my Ph.D study and research.

I would like to express my gratitude to Professor Hiroshi Shinokubo for the constructive comments and warm encouragement.

I have greatly benefited from Professor Yoshito Tobe for the invaluable discussions and suggestions.

I would like to express my appreciation to Assistant Professors Makoto Karakawa, Masashi Nitani, and Seihou Jinnai for the technical assistance, and helpful suggestions.

I appreciate the insightful feedback offered by Specially Appointed Professor Toshihiro Onishi.

I am indebted to Dr. Dayang Zhou for technical supports and helpful suggestions.

I would like to thank Dr. Tatsuhiko Ohto and Ms. Yuka Okumura for technical support for calculation.

I wish to thank Dr. Hiroyasu Sato for the single-crystal X-ray diffraction analysis.

I thank all labmates and colleagues: Dr. Hajime Nitta, Dr. Taichi Moriyama, Mr. Takuji Seo, Ms. Yumi Hirose, Ms. Yoshimi Fujiki, Ms. Keiko Yamazaki, Dr. Chatterjee Shreyam, Dr. Shunsuke Tamba, Ms. Ayana Uchida, Mr. Yuji Okamoto, Ms. Nana Kawaguchi, Mr. Koki Morikawa, Mr. Takuya Inoue, Mr. Kakeru Izuno, Mr, Yota Kishimoto, Mr. Taishi Sakai, Mr. Tomoya Hamada, Mr. Keisuke Nagai, Mr. Ryota Doi, Mr. Tomoya Nishino, Mr. Ryo Adachi, Mr. Yuki Hirai, and Ms. Wansu Wang for the supports, advices, and discussions.

I would like to acknowledge the Research Fellowship for Young Scientists from the Japan Society for the Promotion of Science.

Finally, I express thanks to my family: Yasuo Yamamoto, Mamiko Yamamoto, and Ayaka Yamamoto for the continuous supports during my graduate study.

Keitaro Yamamoto

Ibaraki, Osaka
January 2020